UNIVERSIDAD POLITÉCNICA DE MADRID
Escuela Técnica Superior de Ingenieros Navales

Numerical and Experimental Study of Mooring Systems with Clump Weights for Floating Wind Turbines

DOCTORAL THESIS

Submitted for the degree of Doctor by:

Tomás Lopez Olocco
Mechanical Engineer

Madrid, 2024

UNIVERSIDAD POLITÉCNICA DE MADRID
Escuela Técnica Superior de Ingenieros Navales

Doctoral Degree in Naval Architecture, Marine and Ocean Engineering

Numerical and Experimental Study of Mooring Systems with Clump Weights for Floating Wind Turbines

DOCTORAL THESIS

Submitted for the degree of Doctor by:

Tomás Lopez Olocco
Mechanical Engineer

Under the supervision of:
Dr. Leo M. González Gutiérrez
Dr. Javier Calderón Sánchez

Madrid, 2024

Title: Numerical and Experimental Study of Mooring Systems with Clump Weights for Floating Wind Turbines

Author: Tomás Lopez Olocco

Doctoral Programme: Naval Architecture, Marine and Ocean Engineering

Thesis Supervision:

Dr. Leo M. González Gutiérrez, Full Professor (Universidad Politécnica de Madrid)(Supervisor)

Dr. Javier Calderón Sánchez, Assistant Professor (Universidad Politécnica de Madrid)(Supervisor)

External Reviewers:

Thesis Defense Committee:

Thesis Defense Date:

This thesis has been partially supported by the Ministry of Science, Innovation, and Universities of Spain through projects FOWT-DAMP and FOWT-DAMP2 (References: RTI2018-096791-B-C21, RTI2018-096791-B-C22, PID2021-123437OB-C21, and PID2021-123437OB-C22).

To my parents and my brother

Acknowledgement

During these four years, I have worked hard and put in many hours to ensure that this thesis turns out well, a thesis that I can be proud of, but the part I always looked forward to the most was writing this acknowledgment page. Therefore, as the sentimental person that I am, I am going to enjoy these few lines. This page is not enough to express how grateful I am to each and every person who has been there to make this thesis possible. However, I will do my best.

First and foremost, I must thank my family. Thanks to my parents, Cecilia and Juan, for everything they have done for me; my achievements are the result of all their effort and sacrifice over the years. Thanks to my brother Agustín for always being by my side and giving me that different perspective on things that I so often need. Thanks to my grandparents, Nena, Armando, Natalio and Antonia for being always there for me.

To my advisor Leo, my scientific father, for trusting me from the beginning and throughout the doctorate, for your patience, and for teaching me everything in this world of research that helped shape me into the researcher I am today. Without a doubt, I was very lucky the day of your appointment. To my advisor Javier, for sharing your knowledge with me and introducing me to the complicated world of OpenFOAM, but above all for accompanying me and often providing the support I needed over these years.

To Krish for welcoming me so warmly in Amherst, those were wonderful months, a great experience and opportunity where I learned a lot, thanks for all your teachings. To all the wonderful people of CEHINAV who directly or indirectly helped me during my doctorate, Juan, Daniel, Fali, David, Alberto, Adrián, Ricardo, Julio, and Luis; specially to the Director of the group Antonio for all the shared knowledge in hydrodynamics. A complete paragraph could be dedicated to my office colleague, Patricia. Thank you for being such a great companion these years and for your wise words when I needed them the most. I thank the team at the CEHIPAR ocean basin, Adolfo, Ana, Leandro, Daniel, Amalia, and Julio, for their patience at work. I remember those model tests fondly.

To my best friends in Argentina, Valentina and Franco, thank you for being my daily support from abroad, for motivating me to overcome imposter syndrome, and for continuing fighting for my dreams. To Rocio, Chuco and Pablo, whom I met on my first day in Madrid and have not been apart since then, thank you for making my transition to another country and culture so pleasant. To my friends from the tank, Javier, Andrés, and Antonio, for the great work environment we created, all the laughs, discussions, code exchanges, gym days, and a thousand other things, thank you. Special thanks to you, Antonio, for all that you have taught me about the world of naval architecture, which was unknown to me at the beginning.

Finally, I want to highlight all the financial support I have received for tuition, international stays, paper publications, conference travels, etc. Thanks to the Ministerio de Ciencia, Innovación y Universidades, the Universidad Politécnica de Madrid, and the CEHINAV.

Thank you all. The end.

Agradecimientos

Durante estos cuatro años me he esforzado y trabajado duro muchas horas para que esta tesis salga bien y pueda sentirme orgulloso de ello, pero lo que más ilusión siempre me hizo fue escribir esta página de agradecimientos. Por eso, como buen sentimental que soy, voy a disfrutarlo. Esta página no alcanza para expresar lo agradecido que estoy con todas y cada una de las personas que han estado ahí para que esta etapa de mi vida sea posible. Sin embargo, voy a hacer mi mayor esfuerzo.

En primer lugar, tengo que agradecer a mi familia. Gracias a mis padres, Cecilia, y Juan por todo lo que han hecho por mí; mis logros son fruto de todo su esfuerzo y sacrificio a lo largo de los años. Gracias a mi hermano Agustín por estar siempre a mi lado y por darme siempre esa mirada distinta de las cosas que tanto necesito. Gracias a mis abuelos, Nena, Armando, Natalio y Antonia por haber estado presente siempre.

A mi director Leo, mi padre científico, por confiar en mi desde el principio y durante todo el doctorado, tu paciencia, y por enseñarme todo en este mundo de la investigación que ayudó a convertirme en el investigador que soy hoy. Sin dudas tuve mucha suerte el día de la designación. A mi director Javier, por transmitirme tus conocimientos e iniciarme en el complicado mundo del OpenFOAM, pero sobretodo por acompañarme, y muchas veces dar el apoyo que necesitaba, durante estos años.

A Krish por recibirme tan bien en Amherst, fueron unos meses maravillosos, una gran experiencia y oportunidad en dónde aprendí mucho, gracias por todas tus enseñanzas. A todo el grupo de maravillosas personas del CEHINAV que me han ayudado durante mi doctorado, Juan, Daniel, Fali, Alberto, David, Adrián, Ricardo, Julio y Luis, pero especialmente a su director Antonio, por todas tus enseñanzas de hidrodinámica. Un párrafo aparte podría dedicárselo a mi compañera de despacho Patricia. Gracias por acompañarme tan bien estos años y por tus sabias palabras en aquellos momentos donde más lo necesitaba. Al equipo del canal de olas del CEHIPAR, Adolfo, Ana, Leandro, Daniel, Amalia y Julio, por su paciencia a la hora de trabajar conmigo. Recuerdo esos ensayos de canal con mucho cariño.

A mis mejores amigos de Argentina, Valentina y Franco, gracias por ser mi sostén diario a la distancia y por motivarme a vencer el síndrome del impostor y seguir peleando por mis sueños. A Rocio, Chuco y Pablo, que nos conocimos mi primer día en Madrid y que no nos separamos más, gracias por hacer tan amena mi transición a otro país y otra cultura. A mis amigos que me quedan del canal, Javier, Andrés y Antonio, por el bonito ambiente de trabajo que formamos, todas las risas, discusiones, intercambios de código de programación, las escapadas al gimnasio, y mil cosas más. Gracias especialmente a vos, Antonio, por todo lo que me has enseñado del mundo naval, ajeno a mí en un comienzo.

Por último, quiero destacar todo el apoyo económico que he recibido para matrículas, la estancia, publicar papers, viajes a congreso, etc. Gracias al Ministerio de Ciencia, Innovación y Universidades, a la Universidad Politécnica de Madrid, y al CEHINAV.

Muchas gracias a todos. Fin.

Abstract

The transition towards a low-carbon economy is emerging as one of the most pressing challenges of our era. Among the various sustainable technologies, offshore wind energy stands out because of its potential to significantly contribute to this transition. The international framework is increasingly supportive of offshore wind as a key technology for achieving decarbonization goals, as evidenced by the widespread support it receives in many countries around the globe.

However, the expansion of offshore wind technology faces notable technical and economic challenges, particularly with the trend towards installing turbines in deeper waters. This trend is driven by the fact that most of the US coastlines, almost all of Japan's coastlines, and several locations in Europe, including the coasts of Norway, the Mediterranean, and the Atlantic (Spain and Portugal), require the use of floating wind turbines due to their deep-water conditions. This requires longer mooring lines, which significantly increases their weight, and therefore cost.

This Ph.D. thesis aims to address one of the new critical station-keeping challenges that arise: the demand for innovative and cost-effective mooring solutions for floating wind turbines. The integration of inertial elements, such as clump weights, into mooring lines is explored to improve the response of floating platforms while reducing costs. Clump weights can significantly enhance the performance of mooring systems if properly designed. In this Ph.D. thesis, different possibilities of clump weight inclusion in single and shared mooring systems of floating wind farms are explored; benefits and counterparts are demonstrated.

The methodology adopted along with this thesis is a mixed-method approach that combines numerical simulations with a strong level of experimental validation. First, the hydrodynamics of an isolated clump weight is studied with computational fluid dynamics simulations and experiments. The results are then used to implement these devices in a dynamic mooring line code. In this part of the research it is found that clump weights primarily affect the weight and added mass rather than viscous drag loads in the mooring line. After this, the clump weight is added to the lines of a catenary mooring system of a floating wind turbine and evaluated with numerical simulations in OpenFAST and experiments. The first-order motions remain relatively unchanged, but second-order motions vary due to system stiffness changes, allowing for different offsets. Finally, the contribution of the clump weight in a shared mooring system is explored, in which a reduction of maximum displacements in the horizontal plane and mooring line loads is achieved. In addition, slack/snap conditions are drastically reduced or nearly eliminated.

This Ph.D. thesis provides a comprehensive analysis of the influence of clump weights in the mooring systems for floating wind turbines and floating wind farms. Incorporating clump weights in mooring systems can offer a practical solution to improve the economic and technical viability of offshore wind farms. The findings suggest that clump weights can reduce the overall cost of mooring systems by enhancing performance and reducing material requirements.

Resumen

La transición hacia una economía neutra en emisiones carbono es uno de los desafíos más apremiantes de nuestra era. Entre las diversas tecnologías de energía renovable, la energía eólica marina destaca por su potencial para contribuir significativamente a esta transición. El marco internacional apoya cada vez más a la energía eólica marina como una tecnología clave para lograr los objetivos de descarbonización, como lo demuestra el amplio respaldo que recibe en distintos países alrededor del mundo.

Sin embargo, la expansión de la tecnología eólica marina se enfrenta a desafíos técnicos y económicos notables, especialmente por su tendencia actual de instalar turbinas en aguas cada vez más profundas. Esta tendencia está impulsada por el hecho de que más de la mitad de las costas de Estados Unidos, casi todas las costas de Japón y varios lugares en Europa, incluyendo las costas de Noruega, el Mediterráneo y el Atlántico (España y Portugal), requieren el uso de turbinas eólicas flotantes debido a la profundidad de sus aguas. Esto requiere líneas de fondeo más largas, lo que aumenta significativamente su peso y, por lo tanto, su coste.

Esta tesis doctoral tiene como objetivo abordar uno de los nuevos desafíos críticos en el posicionamiento dinámico de plataformas: la demanda de soluciones de fondeo innovadoras y rentables para turbinas eólicas flotantes. En esta línea, se explora la posibilidad de añadir elementos inerciales, como los *clump weights*, en las líneas de fondeo para mejorar la respuesta de las plataformas flotantes y así reducir los costes.

Los *clump weights* pueden mejorar significativamente el rendimiento de los sistemas de fondeo si se diseñan adecuadamente. En esta tesis doctoral se exploran diferentes posibilidades de inclusión de *clump weights* tanto en sistemas de fondeo individuales como compartidos de parques eólicos flotantes; demostrando así sus fortalezas y debilidades.

La metodología adoptada a lo largo de esta tesis es un enfoque de método mixto que combina simulaciones numéricas con experimentos a escala. En primer lugar, se estudia la hidrodinámica de un *clump weight* aislado mediante simulaciones de dinámica de fluidos computacional y experimentos. Los resultados se utilizan luego para la implementación de estos dispositivos en un código de elementos finitos que incluye los efectos dinámicos de la línea de fondeo. En esta parte de la investigación se encuentra que los *clump weights* afectan principalmente el peso y la masa añadida en lugar de las cargas de arrastre viscoso en la línea de fondeo. Después de esto, se añade el *clump weight* a las líneas de un sistema de fondeo en catenaria de una turbina eólica flotante, y se evalúa mediante simulaciones numéricas en OpenFAST comparados luego con ensayos experimentales realizados también en el marco de esta tesis. Los movimientos de primer orden permanecen relativamente sin cambios, pero los movimientos de baja frecuencia varían debido a los cambios en la rigidez del sistema, permitiendo diferentes desplazamientos. Finalmente, se explora la contribución del *clump weight* en un sistema de fondeo compartido, en el cual se logra una reducción de los desplazamientos máximos en el plano horizontal y de las cargas en las líneas de fondeo. Además, las condiciones de *slack/snap* se reducen drásticamente hasta casi eliminarse.

Esta tesis doctoral proporciona un análisis exhaustivo de la influencia de los *clump weights* en los sistemas de fondeo para turbinas eólicas y parques eólicos flotantes. Las complejas simulaciones numéricas junto con el alto grado de validación experimental que poseen son un punto a destacar de esta tesis doctoral. La incorporación de *clump weights* en los sistemas de fondeo puede ofrecer una solución práctica para mejorar la viabilidad económica y técnica de los parques eólicos marinos. Los hallazgos sugieren que los *clump weights* pueden reducir el costo total de los sistemas de fondeo al mejorar el rendimiento y reducir los requisitos del material.

Publications during the PhD

Journal papers

Lopez-Olocco, T., Calderon-Sanchez, J., González-Gutiérrez, L. M. (2024) Experimental validation of the simulations of the flow around an impulsively started scaled clump weight using an overset dynamic mesh with OpenFOAM. (Under revision, Ocean Engineering). **(Q1)**.

Liang, G., **Lopez-Olocco, T**., Medina-Manuel, A., Ynocente, L. S., Jiang, Z., and Souto-Iglesias, A. (2024). Experimental investigation of two shared mooring configurations for a dual-spar floating offshore wind farm in irregular waves. *Marine Structures*. **(Q1)**.

Lopez-Olocco, T., Liang, G., Medina-Manuel, A., Ynocente, L. S., Jiang, Z., and Souto-Iglesias, A. (2023). Experimental comparison of a dual-spar floating wind farm with shared mooring against a single floating wind turbine under wave conditions. *Engineering Structures*, 292, 116475. **(Q1)**.

Lopez-Olocco, T., González-Gutiérrez, L. M., Calderon-Sanchez, J., Marón Loureiro, A., Saavedra Ynocente, L., Bezunartea Barrio, A. and Vivar Valdés, N. (2022). Experimental and Numerical Study of the Influence of Clumped Weights on a Scaled Mooring Line. *Journal of Marine Science and Engineering*, 10 (5), 676. **(Q1)**.

Saettone, S., **Lopez-Olocco, T.**, Medina-Manuel, A., Taskar, B., Steen, S. and Andersen, P. (2022). Experimental measurements of propulsive factors in regular deep-water following waves for a fishing trawler. *Ocean Engineering*, 263, 112167. **(Q1)**.

Conference papers

Lopez-Olocco, T., González Gutiérrez, Leo M., Thiagarajan, Krish Sharman (2024) Validation of a Mooring System with Clump Weights for a Spar Floating Wind Turbine Model using Openfast. In *43th International Conference on Ocean, Offshore & Arctic Engineering*, Singapore EXPO, Singapore.

Saleh, S., Akers, R., Koo, B., Yau, H., **Lopez-Olocco, T.** and Thiagarajan, K. (2023). Comparison of Fatigue Characteristics of Polyester and Nylon Mooring Lines for Shallow Water Floating Offshore Wind Turbines. In *5th International Offshore Wind Technical Conference*, Exeter, England.

Jiang, Z., Liang, G., **Lopez-Olocco, T.**, Medina-Manuel, A., Saavedra-Ynocente, L.A. and Souto-Iglesias, A. (2023) Model test of a dual-spar floating wind farm in regular waves. In *9th International Conference on Marine Structures*, Gothenburg, Sweden.

Contents

Acknowledgement . . . iii
Agradecimientos . . . iv
Abstract . . . v
Resumen . . . vi
Publications during the PhD . . . viii
List of Figures . . . xiii
List of Tables . . . xviii
Abbreviations . . . xxi

1 Introduction **1**
1.1 The offshore wind industry . . . 1
1.2 Floating Offshore Wind Energy . . . 3
1.2.1 Types of floating platforms . . . 4
1.2.2 Types of mooring systems . . . 6
1.2.2.1 Hybrid mooring systems . . . 7
1.2.2.1.1 Multi-component lines . . . 7
1.2.2.1.2 Additional devices: Buoys and clump weights . . . 7
1.2.2.1.3 Additional devices: shock loads absorbers . . . 7
1.2.2.2 Shared mooring systems . . . 9
1.2.3 Previous and current projects . . . 10
1.2.4 Cost and challenges . . . 11
1.3 Background and Motivation . . . 12
1.4 Objectives . . . 12
1.5 Structure of the Thesis . . . 14

2 State of the art **15**
2.1 Clump weight hydrodynamics . . . 15
2.2 Isolated mooring lines: Fairlead prescribed motions in forced oscillations . . . 17
2.3 Mooring systems of FWTs . . . 20
2.4 Shared mooring systems of FWFs . . . 22

3 Hydrodynamics of impulsively started clump weights **25**
3.1 Abstract . . . 25
3.2 Experiment descriptions . . . 25
3.2.1 Experimental set-up . . . 25

3.2.2 Dimensional analysis . . . 27
3.3 Numerical model . . . 30
3.3.1 Governing equations . . . 30
3.3.2 Turbulence modeling . . . 30
3.3.3 Overset technique . . . 31
3.3.4 Numerical schemes and solver parameters . . . 31
3.3.4.1 Numerical discretization schemes: fvSchemes . . . 31
3.3.4.2 Linear equations solvers: fvSolution . . . 32
3.4 Test cases description and set-up . . . 32
3.4.1 Numerical model verification: impulsively started circular cylinder . . . 32
3.4.2 Numerical model validation: experimental case . . . 35
3.5 Results . . . 37
3.5.1 Unsteady flow past a impulsively started circular cylinder . . . 38
3.5.1.1 Re = 3000 . . . 39
3.5.1.2 Re = 9500 . . . 39
3.5.2 Numerical validation with experiments . . . 44
3.5.2.1 Hydrodynamic force . . . 44
3.5.2.2 Flow description and features . . . 47
3.6 Computational resources . . . 49
3.7 Concluding remarks . . . 51

4 Inclusion of clump weights on isolated catenary mooring lines 53
4.1 Abstract . . . 53
4.2 Experiments description . . . 54
4.2.1 Test matrix . . . 60
4.3 Numerical implementation: Theoretical background . . . 62
4.3.1 Quasi-static approach . . . 62
4.3.2 Dynamic approach . . . 63
4.3.2.1 Basic dynamic equations . . . 63
4.3.2.2 Clump Weight implementation . . . 65
4.3.2.3 Computational parameters used in the simulations . . . 66
4.3.2.3.1 OPASS numerical tool . . . 66
4.3.2.3.2 MoorDyn numerical tool . . . 67
4.4 Experimental results and numerical validation . . . 68
4.4.1 Static cases . . . 68
4.4.2 Dynamic cases . . . 69
4.4.2.1 Tensions response . . . 69
4.4.2.1.1 Dissipated energy . . . 74
4.4.2.1.2 Numerical validation . . . 76
4.4.2.2 Motions response . . . 81
4.4.2.2.1 Numerical validation . . . 83
4.5 Concluding remarks . . . 85

5 Inclusion of clump weights along catenary mooring lines of FWTs 87
5.1 Abstract . . . 87

5.2 Case of study . . . 87
5.2.1 Description of the FWT . . . 87
5.2.2 Environmental conditions . . . 88
5.2.3 Mooring system design . . . 89
5.3 Experimental tests . . . 90
5.3.1 Experimental set-up . . . 91
5.3.2 Test matrix . . . 94
5.3.3 Instrumentation . . . 95
5.3.4 Methodology . . . 96
5.3.4.1 Decay tests . . . 96
5.3.4.2 Wave tests . . . 99
5.3.4.2.1 Wave calibration . . . 99
5.3.4.2.2 Response amplitude operators (RAOs) . . . 100
5.4 Numerical model calibration . . . 101
5.5 Results . . . 103
5.5.1 Natural frequencies and damping estimation . . . 103
5.5.2 First-order RAOs from the regular wave and white noise cases . . . 104
5.5.3 Response analysis for the irregular wave cases . . . 105
5.5.3.1 Motion responses . . . 106
5.5.3.1.1 Spectral analysis . . . 106
5.5.3.1.2 Statistics . . . 107
5.5.3.2 Tension responses . . . 108
5.5.3.2.1 Spectral analysis . . . 110
5.5.3.2.2 Statistics . . . 111
5.6 Concluding remarks . . . 113

6 Inclusion of clump weights along shared lines of FWFs 115
6.1 Abstract . . . 115
6.2 Description of the FWF . . . 115
6.2.1 Mooring system design . . . 116
6.3 Experimental tests . . . 118
6.3.1 Experimental set-up . . . 118
6.3.2 Test matrix . . . 120
6.3.3 Instrumentation . . . 120
6.3.4 Methodology . . . 121
6.3.4.1 Decay tests . . . 121
6.3.4.2 Wave tests . . . 121
6.4 Results . . . 122
6.4.1 Natural frequencies and damping estimation . . . 122
6.4.2 First-order RAOs from the regular wave and white noise tests . . . 123
6.4.3 Response analysis for the irregular wave tests . . . 124
6.4.3.1 Motion responses . . . 125
6.4.3.1.1 Spectral analysis . . . 125
6.4.3.1.2 Statistics . . . 127
6.4.3.2 Tension responses of the anchor lines . . . 129

6.4.3.2.1 Spectral analysis . . . 129
6.4.3.2.2 Statistics . . . 129
6.4.3.3 Tension responses of the shared line . . . 131
6.4.3.3.1 Spectral analysis . . . 132
6.4.3.3.2 Slack and Snap events analysis . . . 133
6.4.3.3.3 Statistics . . . 133
6.4.3.3.4 Analysis of Extreme Mooring Tension . . . 135
6.5 Concluding remarks . . . 138

7 Conclusions and future work **141**
7.1 Conclusions . . . 141
7.2 Future research lines . . . 144

List of Figures

1.1 Global offshore wind capacity in operation [137]. . . . 3
1.2 Different platform concepts for FWT: (a) Semi-submersible, (b) Spar and (c) TLP. . . . 5
1.3 Mooring configurations of FWTs. . . . 6
1.4 Catenary line diagram of a mooring line with a clump weight and a buoy. . . . 8
1.5 Sample of polymer springs attached to the line [97]. . . . 8
1.6 Shared mooring line between FWT. . . . 9
1.7 Timeline of floating offshore wind turbine deployments, including prototypes, demonstrators, and farms (Edwards et al. [37]). . . . 11
1.8 Scope of the thesis and the different "zoom levels". . . . 13

3.1 Experimental set-up. . . . 26
3.2 External forces acting on the scaled clump weight. . . . 27
3.3 Designed and manufactured scaled clump weight. . . . 29
3.4 Motion law applied to the Arduino controller. . . . 29
3.5 Computational domain with labels corresponding to the boundaries. . . . 33
3.6 Overset boundary assignment . . . 34
3.7 Background and overset mesh around the circular cylinder. . . . 34
3.8 Computational domain for the validation case. . . . 36
3.9 zoneID and cellTypes assigned for the overset dynamic mesh. . . . 37
3.10 Detailed view of the different refinement areas. . . . 38
3.11 Result of the moving average mean postprocessing applied for de overset results (C_D comparison). . . . 39
3.12 C_D comparison for different dynamic meshes and turbulence model of an impulsively started circular cylinder at Re = 3000. . . . 40
3.13 (a) Instantaneous streamlines from present work, (b) Experiments from Bouard and Coutanceau [8], and (c) Instantaneous streamlines from [77], of an impulsively started circular cylinder for Re = 9500 at $T = 2.0$. . . . 41
3.14 Vorticity field of an impulsively started circular cylinder at adimensionalized time $T = 1$, $T = 3$, and $T = 6$ (Re = 9500). . . . 42
3.15 C_D comparison for different turbulence modeling. . . . 43
3.16 Mesh convergence for the verification case (Re = 9500) for different turbulence modeling. . . . 44

3.17 Numerical comparison of the CFD results and the quasi-static empirical model approximation. . . . 45
3.18 Post-processed instantaneous position x of the clump weight (top), the derived velocity v (middle), and acceleration a (bottom). . . . 46
3.19 Experimental force (EFD) and numerical force (CFD) comparison. . . . 46
3.20 Pressure field of the flow around the impulsively started clump weight at times $t = 1.0s$, $t = 2.0s$, $t = 3.0s$, $t = 4.0s$, $t = 5.0s$, and $t = 6.0s$. The motion is in the upward direction. . . . 48
3.21 Q-criterion isosurfaces. $Q = 1$ at $t = 2.0s$. . . . 49
3.22 Pressure field of the flow around the impulsively started clump weight at times $t = 6.5s$, $t = 7.0s$, $t = 7.5s$, $t = 8.0s$, $t = 8.5s$, and $t = 8.75s$. The motion is in the upward direction. . . . 50

4.1 (**Left**) OC4-DeepCWind FOWT design. (**Right**) Top view of the mooring system of the OC4-DeepCWind FWT [121]. . . . 54
4.2 CEHIPAR facilities. (**a**) CEHIPAR towing tank. (**b**) CEHIPAR towing tank carriage. . . . 55
4.3 Main dimensions of the selected chain. . . . 57
4.4 Schematic layout of the top and side views of the experimental setup. . . . 57
4.5 Typical clump weight used in the offshore industry. . . . 58
4.6 Designed and manufactured scaled clump weight (**left**) and snapshot of the clump weight installed in the mooring line obtained with the submerged camera (**right**). . . . 59
4.7 The load cell and dynamometer connection to the aluminum beam attached to the linear guide. . . . 59
4.8 Catenary shape of all the tested configurations. . . . 62
4.9 Free body diagram of a mooring line with a clump weight positioned at point P. 64
4.10 External forces acting on an element of line. . . . 66
4.11 Horizontal stiffness of the line in all tested configurations. . . . 69
4.12 Pretension of the tested configurations - vector representation. . . . 69
4.13 Fairlead tension during the fairlead displacement with and without clump weight for three different fairlead amplitude values for Configuration 1. . . . 71
4.14 Fairlead tension during the fairlead displacement with and without clump weight for three different fairlead amplitude values for Configuration 2. . . . 72
4.15 Fairlead tension during the fairlead displacement with and without clump weight for three different fairlead amplitude values for Configuration 1 (with the same pretension). . . . 73
4.16 Experimental comparison fairlead tension time series for $A = 0.225\ m$ and $T = 2.8\ s$. . . . 74
4.17 Dissipated energy for all the test matrix in the non-dimensional form. . . . 75
4.18 Dissipated energy under the imposed top-end motions for the mooring line without clump weight. . . . 76
4.19 Dimensionless increase of dissipated energy due to the clump weights. . . . 77

4.20 Comparison between the computed fairlead tension values and the experimental measurements of the isolated mooring line for three different oscillation amplitudes $A = 0.125,\ 0.175,\ 0.225\ [m]$ and three different periods $T = 2.8,\ 3.5,\ 5.5\ [s]$ for the isolated mooring line. 78
4.21 Comparison between the computed fairlead tension values and the experimental measurements of the isolated mooring line with the clump weight in Config. 1 for three different oscillation amplitudes $A = 0.125,\ 0.175,\ 0.225\ [m]$ and three different periods $T = 2.8,\ 3.5,\ 5.5\ [s]$ for the isolated mooring line. 79
4.22 Comparison between the computed fairlead tension values and the experimental measurements of the isolated mooring line with the clump weight in Config. 2 for three different oscillation amplitudes $A = 0.125,\ 0.175,\ 0.225\ [m]$ and three different periods $T = 2.8,\ 3.5,\ 5.5\ [s]$ for the isolated mooring line. 80
4.23 Trajectories of the tracked points of the mooring line for a top-end motion of an Amplitude of 0.175 m and periods 3.5 s. Markers 2 to 10 are indicated in the figure. 81
4.24 Tracked motions of three points of the mooring line, for a top-end motion of an Amplitude of 0.125 m and periods $2.8, 3.5, 5.5$ s. 82
4.25 Comparison between computed trajectories of catenary nodes and experimental tracked points for different oscillation periods $T = 2.8,\ 3.5,\ 5.5$ s and amplitude $A = 0.125$ m for the isolated mooring line without clump weight. 83
4.26 Comparison between computed trajectories of catenary nodes and experimental tracked points for different oscillation periods $T = 2.8,\ 3.5,\ 5.5$ s and amplitude $A = 0.125$ m for the isolated mooring line with clump weight (Configuration 1). 84

5.1 Top and side view of the mooring system configuration (dashed line: wire; solid line: chain). The symbols $f1$, $f2$, $f3$, $f4$ denote the fairlead connections. . . 88
5.2 Side view of the designed mooring system configurations with clump weights (dashed line: wire; solid line: chain; red colored dot: clump weight Config. 1; blue colored dot: clump weight Config. 2). 90
5.3 Top view of the model with the aluminum structure, including the instrumentation cables. 92
5.4 Mooring line connections. 93
5.5 Experimental layout of the spar FWT. Dimensions at model scale $[m]$ 94
5.6 The spar model in testing position with the instrumentation circled in red. . 96
5.7 Detailed view of the instruments used for motion measurement during the tests. 96
5.8 Detailed view of the load used during the tests and the line arrangement. . . 97
5.9 Detailed view of the ultrasonic wave probe. 97
5.10 Exemplied analysis of a decay time series. 98
5.11 Illustration of the model FWT during seakeeping tests. 99
5.12 Calibration of the wave power spectra. 100
5.13 Numerical convergence analysis with MoorDyn of equilibrium fairlead pretensions. 102
5.14 Surge platform motions in the experimental and numerical decay tests for the Baseline configuration. 104
5.15 Numerical-experimental RAOs magnitudes comparison for the baseline configuration. 105

5.16 Numerical comparison of the magnitude of the surge, heave and pitch RAOs for all the mooring configurations. 106
5.17 Numerical-experimental comparison of surge motion for the Baseline mooring configuration in the extreme wave condition, wave seed IRR02B. 107
5.18 Numerical and experimental PSDs of surge motion for all the tested configurations. 108
5.19 Numerical and experimental PSDs of heave motion for all the tested configurations. 108
5.20 Numerical and experimental PSDs of pitch motion for all the tested configurations. 109
5.21 Numerical-experimental comparison of the fairlead tension T_{f3} for the Baseline mooring configuration in the extreme wave condition, wave seed IRR02B. . . 110
5.22 Numerical and experimental PSDs of T_{f1} fairlead tension for all the tested configurations. 111
5.23 Numerical and experimental PSDs of T_{f3} fairlead tension for all the tested configurations. 111

6.1 Side view of the Dual-spar FWF with different mooring systems (dashed line: steel wire; solid line: chain). 116
6.2 Top view of the Dual-spar FWF with different mooring systems (dashed line: wire; solid line: chain). The symbols $f1$, $f2$, $f3$, $f4$ denote the fairlead connections that are measured in the experiments. 117
6.3 Experimental layout of the dual-spar FOWF with shared mooring configurations (dimensions in $[m]$) 119
6.4 Illustration of the experimental layout of the baseline configuration 120
6.5 Image of the FWT models instrumented in the testing position. 121
6.6 Illustration of the Dual-spar FWF during seakeeping tests. 122
6.7 Comparison of response amplitude operators for surge, heave and pitch motions, single- and dual-spar configurations. 124
6.8 Comparison of response amplitude operators for anchor lines (T_{f1}) and shared line (T_{f3}); single- and dual-spar configurations. 125
6.9 Averaged surge spectra for the IRR02 wave case. $H_s = 12.7\ m$ and $T_p = 15.45\ s$ 125
6.10 Comparison of averaged heave and pitch spectra for the IRR02 wave case. $H_s = 12.7\ m$ and $T_p = 15.45\ s$ 126
6.11 POE of surge and pitch for the IRR02 wave case. $H_s = 12.7\ m$ and $T_p = 15.45\ s$. 127
6.12 Comparison of surge and pitch motion statistics for the IRR02 wave case. $H_s = 12.7\ m$ and $T_p = 15.45\ s$. The statistical values are averaged across three realizations except "Max abs" and "Min abs". "Max abs": total maximum among three realizations; "Min abs": total minimum among three realizations; "Max": maximum; "Min": minimum; 'RMS": root mean square; "95%": 95% quantile; "5%": 5% quantile. 128
6.13 Comparison of the anchor line tension PSDs for the IRR02 wave case. $H_s = 12.7\ m$ and $T_p = 15.45\ s$. 129
6.14 Comparison of the anchor line tension POEs for the IRR02 wave case. $H_s = 12.7\ m$ and $T_p = 15.45\ s$. 130
6.15 Anchor lines tension statistics (normalized with the pretension) for the IRR02 wave case. $H_s = 12.7\ m$ and $T_p = 15.45\ s$. 131

6.16 Comparison of the anchor line tension $[N]$ in all configurations for extreme case IRR02B. 131
6.17 Comparison of the shared line tension $[N]$ in all configurations for extreme case IRR02B. 132
6.18 Shared line fairlead tension T_{f3} PSD for the extreme IRR02 wave case. $H_s = 12.7\ m$ and $T_p = 15.45\ s$. 132
6.19 Identified snap load events in the time series of mooring tension T_{f4}, case IRR02A. 134
6.20 POE of the time history of the shared line fairlead tensions Tf_3 for the extreme IRR02 wave case. $H_s = 12.7\ m$ and $T_p = 15.45\ s$. 135
6.21 POE of the peaks of the time history of the shared line fairlead tensions Tf_3 for the extreme IRR02 wave case. $H_s = 12.7\ m$ and $T_p = 15.45\ s$. 135
6.22 POE of the peaks of the time history of the shared line fairlead tensions Tf_4 for the extreme IRR02 wave case. $H_s = 12.7\ m$ and $T_p = 15.45\ s$. 136
6.23 shared line fairlead tension statistics (normalized with the pretension) for the extreme sea state. IRR02 wave case. $H_s = 12.7\ m$ and $T_p = 15.45\ s$ 136
6.24 Quantile-Quantile (Q-Q) plots for the 3-P Weibull fitted distribution in mooring tension T_{f4}, extreme condition, IRR02A wave case. $H_s = 12.7\ m$ and $T_p = 15.45\ s$. 137
6.25 Comparison of estimated MPME of mooring tension in the two mooring configurations, extreme condition, IRR02A wave case. $H_s = 12.7\ m$ and $T_p = 15.45\ s$. 138

List of Tables

2.1 Comparison table of the existing research literature of mooring lines forced oscillations. . . . 19

3.1 Scaled clump weight properties . . . 29
3.2 Boundary conditions used in the verification case. . . . 34
3.3 Numerical schemes used in the verification case. . . . 35
3.4 Boundary conditions used in the validation case. . . . 36
3.5 Numerical schemes used in the validation case. . . . 37
3.6 pimpleDyMFoam solver CPU time costs and parameters for the simulated cases. The diameter D is taken as the characteristic length for all the cases. 51

4.1 OC4-DeepCWind mooring system properties [121]. . . . 56
4.2 Involved variables in the design of the scaled clump weight. . . . 58
4.3 Position of the red marks used for capturing the line movements. . . . 60
4.4 Amplitudes of the fairlead motions for $\lambda = 1/30$. . . . 61
4.5 Fairlead motions periods in seconds for $\lambda = 1/30$. . . . 61
4.6 Parameters of the computational model. . . . 67
4.7 Experimental-numerical comparison of pretension of each configuration. . . . 68

5.1 Environmental parameters for mooring system design. . . . 88
5.2 Design variables and design space of the anchor lines . . . 89
5.3 Properties of the mooring lines adopted in the design. . . . 89
5.4 Froude scaling of variables . . . 91
5.5 Target and measured mass properties at model scale. . . . 92
5.6 Physical properties of the scaled mooring lines . . . 94
5.7 Target and measured pretensions for both configurations. . . . 95
5.8 Summary of test cases with irregular and regular waves. . . . 95
5.9 Experimental-numerical comparison of pretension, after line length tuning. . . . 102
5.10 Estimation of the critical damping ratio ξ (Eq. 5.10) for the experiments and the numerics [%]. . . . 103
5.11 Natural period estimation for the experiments and the numerics [s]. . . . 104
5.12 Motion statistics . . . 109
5.13 Fairlead tensions statistics. . . . 112

6.1 Mooring properties of the two shared mooring configurations (full scale, refer to Fig. 6.1) . . . 117
6.2 Target and measured mass properties of the FOWT models (model scale) . . 118
6.3 Mooring properties of the mooring lines used in the tests (model-scale) . . . 119
6.4 Target and measured pretension for the two shared mooring configurations (model-scale) . . . 120
6.5 Natural period estimation for the tested configurations [s]. . . . 123
6.6 Estimation of the damping ratio ξ for the tested configurations [%]. . . . 123
6.7 T_{MPME} for the two shared mooring configurations (averaged over three cases). 138

Abbreviations

CAPEX Capital expenditures

CEHINAV Canal de Ensayos Hidrodinámicos de la ETSI Navales

CEHIPAR Canal de Ensayos Hidrodinámicos de El Pardo

CFD Computational Fluid Dynamics

COG Center of Gravity

DLC Design Load Case

DNS Direct Numerical Simulation

DOF Degree of Freedom

EFD Experimental Fluid Dynamics

FWT Floating Wind Turbine

FWF Floating Wind Farm

FVM Finite Volume Method

IEC International Electrotechnical Commission

ITTC International Towing Tank Conference

JONSWAP Joint North Sea Wave Project

KHL Kelvin Hydrodynamics Laboratory

LCOE Levelized Cost of Energy

LED Light Emitting Diode

MARIN Maritime Research Institute Netherlands.

MARINTEK Norwegian Marine Technology Research Institute (now SINTEF)

NMRI National Maritime Research Institute

NREL National Renewable Energy Laboratory

OPEX Operating expenses

O&G Oil and Gas

PET Polyester ("Polyethylene terephthalate")

PSD Power Spectral Density

RANS Reynolds Average Navier Stokes

RAO Respose Amplitude Operator

SPH Smoothed Particle Method

UK United Kingdom

ULS Ultimate Limit State

US United States of America

Chapter 1

Introduction

1.1 The offshore wind industry

The exploitation of wind energy has been used since ancient times, more than 3,000 years ago for irrigation or milling; but it was not until the late 19th century that it was used to produce electrical power. Danish scientist Poul La Cour was influential in shaping modern technology with his windmills, producing 20 to 35 kW. This led to the development of turbines in the range of 30 to 60 kW, and just after World War II, Johhanes Juul developed the 200 kW Gedser turbine. By 1980, Denmark had established itself as a key player in wind energy along with the US, having developed high-power turbines and improved technology over the years [96].

Concepts like disaster or change began to emerge in people's general thinking in the 1970s, due to the environmental consequences of industrial development. This was compounded by public awareness of the potential harms of nuclear energy, which led to an environmental consciousness movement to seek alternative energy sources. However, the wind energy race began with the severe oil crisis in the mid-1970s, when governments began to explore new energy sources and channel efforts towards this. This combination of events was the key element that triggered the gradual increase in turbine power and improved technology, making wind energy a reliable and economically viable alternative energy source. In 2022, almost 7% of the electrical energy produced came from wind energy [57].

The lack of land to install wind turbines, along with the impact of visual contamination and noise on people, motivated the idea of taking wind turbines offshore. The first futuristic concepts of offshore wind turbines were developed by Hermann Honnef and other concepts were proposed in the United States in the 1970s, but they were never implemented. The first wind turbine installed at sea dates back to 1991 in Sweden and the first large farm was installed in 1992 in Vindeby, Denmark. Since then, growth has been exponential, marked by the following milestones:

- Vindeby, Denmark, 1991: First offshore wind farm with a capacity of 4.5 MW.
- Horns Rev 1 (Denmark 2002): First wind farm that marked the transition from pilot

test or demonstration to large scale. First wind farm to use steel monopiles and to have its own designated offshore substation. Capacity of 160 MW.

- Beatrice (Great Britain 2007): 2 prototypes of 5 MW turbines installed at a depth of 45 m, the deepest at the time.
- Hywind (Norway 2009): First floating spar-type wind turbine installed. Pilot test of 2.3 MW at 220 meters depth.
- WindFloat 1 (Portugal 2011): First semi-submersible floating wind turbine installed. Pilot test of 2 MW.
- Hywind Scotland (Great Britain 2017): First floating wind farm. Installed capacity of 30 MW.
- Germany 2017: First offshore wind energy contract with zero subsidy from a government.
- Hywind Tampen (Norway 2022): First renewable energy source for the offshore oil industry. Floating concrete spar-type wind turbines with shared anchors. Installed capacity of 88 MW.

Considering that around 80% of the world's population is located no more than 100 km from coastal lines, it makes sense to seize this great opportunity to exploit the vast potential of offshore wind power. Offshore wind power has several advantages that we can mention, such as:

- The wind resource is more abundant and stable offshore, with higher wind speeds and more consistent directions. Therefore, the power output can be greater than that of an onshore wind farm.
- The impact of noise pollution from rotor rotation is less, allowing for bigger machines with larger rotor diameters to be employed offshore, i.e., greater power output.
- The visual impact on the landscape is considerably reduced, as they are located far from populated areas.
- Larger farms than those on the continent can be installed, since offshore there is an abundance of physical space to place wind turbines.

While among the principal disadvantages, we can mention the following:

- Like those installed on the continent, the installation of wind farms implies an environmental impact on the site. As it is a relatively new technology, research continues on the negative effects on biological life and how to fully understand all of them.
- Although project costs are reduced year by year, the investment (CAPEX) in these mega-engineering projects is still very high, so large consortia of companies and governments are usually necessary.
- The necessary infrastructure is more complex, the supply chain is challenging and the offshore operation and maintenance are more complicated; therefore, the costs (OPEX) of these projects are much higher than their onshore counterparts nowadays.

The international framework is clearly favorable for offshore wind as a key technology in meeting decarbonization goals, as evidenced by the support received in many European countries, which have been betting on this form of energy for years, in line with the EU's strategic goal of consolidating itself as a global leader in this technology [23]. The global offshore market grew on average by 21% each year in the past decade, bringing the total installed capacity in operation to 67 GW (see Figure 1.1). From this capacity, almost 50% is installed in China [137].

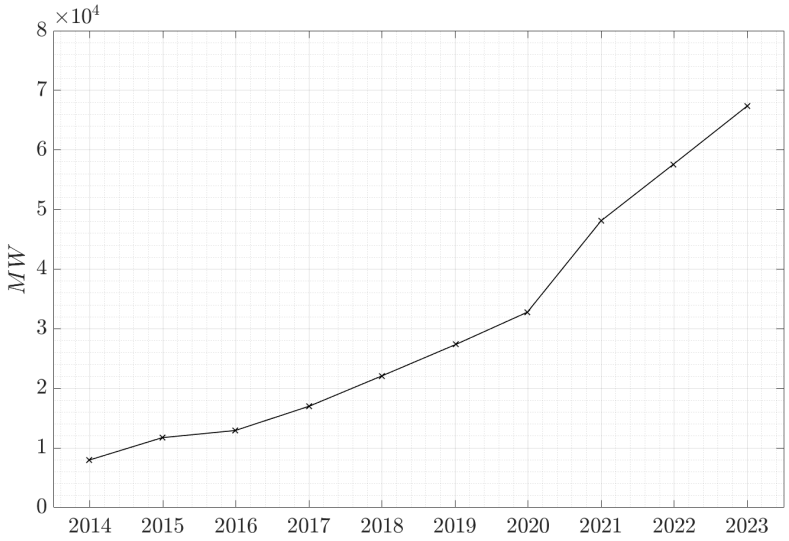

Figure 1.1: Global offshore wind capacity in operation [137].

The exploitation of offshore wind energy is very promising economically but has also become a great technical challenge due to the growing trend of placing increasingly larger power (and therefore diameter, weight, height) wind turbines in ever deeper waters, which for techno-economic reasons require exploitation through floating wind turbines due to their deep waters. This trend occurs because 61% of the US coasts, almost all the coasts of Japan, and several European locations, such as the coasts of Norway, the Mediterranean, and the Atlantic (Spain and Portugal) have deep water a short distance from shore. In addition, in deep-water regions, better atmospheric conditions are found.

1.2 Floating Offshore Wind Energy

Beyond a certain depth, fixed offshore wind turbines are not an option because they are no longer techno-economically viable, demanding the deployment of floating wind turbines to enable the exploitation of wind resources in deeper sea locations [119]. Therefore, FWTs stand out as a key technology in unlocking the vast potential of offshore wind energy.

The various concepts for floating wind turbine platforms, along with their associated mooring and anchor technologies, are based on the legacy of deep-water floating platforms from the oil

and gas offshore industry, although with some differences for different needs. For example, the size difference between platforms for oil and gas extraction and those for floating wind turbines is substantial; the floating wind sector requires the installation of a large number of smaller structures. This directly impacts the design, manufacturing, installation, and operation of these structures, highlighting the urgent need for the industrialization of these units.

1.2.1 Types of floating platforms

There are numerous concepts of floating platforms to support wind turbines offshore. These can be classified into three main groups based on how the system achieves its static stability. These three main categories are illustrated in Figure 1.2.

- **Tension Leg Platform (TLP)**: This type of platform has positive buoyancy and achieves stability through the tension of its mooring system. Among its advantages, we can highlight:
  - Very reduced linear and rotational movements (excellent stability).
  - Due to its low draft, it has a flexible range of installation depths.
  - Low structural mass.
  - Can be assembled in port and towed to its final production destination.

  Conversely, among its disadvantages, we can highlight:
  - High loads on the mooring and anchors (significant seabed preparation required).
  - Complex and very costly mooring installation.
  - The tendons adjust to tidal variations.
  - Specialized vessels required for installation.
  - They are not self-stable before installation nor during towing operations.
- **Semi-submersible**: This type of platform achieves stability by distributing its buoyancy and using the advantage of high inertia from the flotation area to achieve a restoring moment. Among its advantages, we can highlight:
  - Relatively low movements, few downtime instances.
  - Due to its low draft, it has a flexible range of installation depths.
  - Easy to bring to port for major repairs.
  - Does not require specialized vessels, only towing ships.
  - Can be assembled in port and towed to its final production destination, simpler installation.

  Conversely, among its disadvantages, we can highlight:

  - Can have resonant horizontal movements due to second-order or drift forces.
  - Waves can induce significant loads, especially vertical ones.
  - Complex steel structures with many welded joints.
  - Large dimensions (high structural mass) to provide sufficient buoyancy and stability.

- **Spar**: This platform type achieves stability by having its center of gravity below the center of buoyancy, which produces a stabilizing moment and great inertial resistance in roll and pitch. Among its advantages, we can highlight the following.
  - Simple design and feasible for series production.
  - Improved linear displacement performance due to deep draft and small flotation area.
  - Excellent stability.
  - Reduced wave-induced forces (smaller area of impact).

  In contrast, among its disadvantages, we can highlight the following.
  - Considerable rotational movements due to the low stability of the waterline area.
  - Due to its draft, its use is restricted to areas of great depth.
  - Assembly usually must be performed at sea, requiring special ships and cranes.
  - Its great draft limits the ability to be towed to port for major repairs.

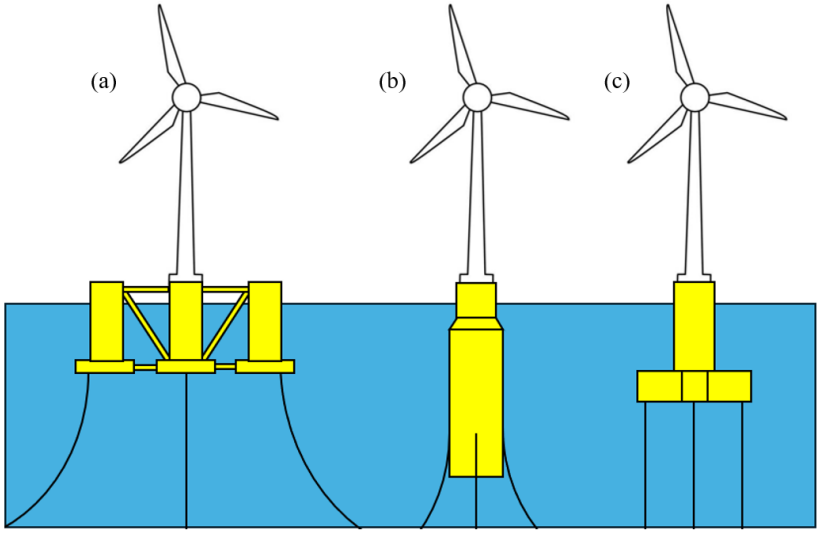

Figure 1.2: Different platform concepts for FWT: (a) Semi-submersible, (b) Spar and (c) TLP.

Regarding the installation of these platforms, the method depends on various factors, such as the platform's draft, the type of platform, the availability of special installation vessels, the draft of the port, among others. The current trend in the industry (when possible) which is attractive to them in terms of costs and logistics is to assemble the platform-tower-rotor-nacelle

assembly in the port and then tow it to the final installation site. Because of the mentioned characteristics, among the current floating platform concepts, the semi-submersible stands out as the ideal for this operation and several current and past offshore projects have chosen this platform concept [37].

1.2.2 Types of mooring systems

Mooring systems are typically composed of chain mooring lines that are fixed to the floating platform by means of a fairlead and the lower end is anchored to the seabed. The mooring systems can be classified as spread mooring or tension leg mooring. Basically, three main mooring concepts arise from that classification:

- *Catenary mooring system* (Figure 1.3a) is the most classic mooring system used in industry. The mooring lines are suspended by its own weight in water. On excursion, the line is lifted and the suspended length of the line increases. Thus, it is this weight, along with its geometry, that provides the restoring in all horizontal motions (surge, sway, and yaw), which is why the footprint is elevated in most cases.
- *Taut and semi-taut mooring system* (Figure 1.3b) is made up of stretched lines whose weight in water is very small. The line stretches when an excursion occurs, so the restoring depends on the elasticity of the line material. The mooring line is tense or semi-tense and forms an angle with the seabed, which is why anchors have a vertical load component in all working conditions, increasing their cost and complexity.
- *Tension leg mooring* (Figure 1.3c) is used in the TLPs. The tendons provide stiffness in the horizontal plane, as well as forces and moments of restoring in vertical movements. Because of this, the platforms that use this mooring system are not stable without it.

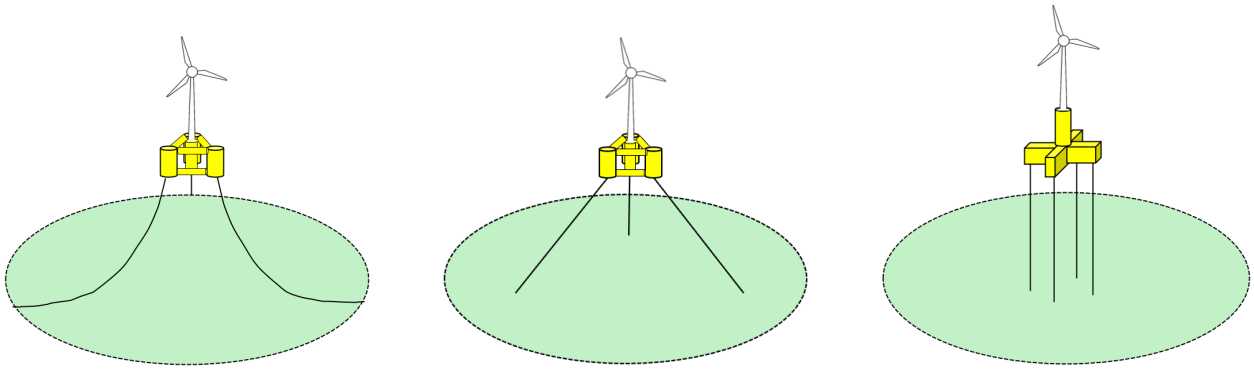

(a) Catenary mooring system (b) Taut mooring system (c) Tension leg mooring system

Figure 1.3: Mooring configurations of FWTs.

1.2.2.1 Hybrid mooring systems

As in many works that are found in the literature, we understand the technical term hybrid mooring system as a mooring system composed of different materials in addition to the chain (steel cable or synthetic materials) and/or that includes different additional devices like buoys, clump weights, etc.

1.2.2.1.1 Multi-component lines To reduce the line cost with long chain lines in deep waters, different segments of the lines are replaced with lighter and cheaper materials. Common materials used are steel wires and synthetic materials.

- Steel cable: A steel cable is a series of steel wires strands that coil about a central core. Usual configurations are the six trand steel wire and the spiral strand steel wire. They are lighter than chain and become ideal for taut lines. The poor bending properties need to be accounted for in transport and installation.
- Synthetic materials: Polyester and nylon are the two firm candidates for fiber rope mooring in the offshore wind industry; however, more research is necessary, especially regarding visco-elasticity models and the associated material hysteresis. Internal abrasion and reduced resistance against wear are the main disadvantages, while the high elasticity and strength to weight ratio are the main benefits.

For deep water, this multi-component mooring is suitable because of the combination of different materials. A proper combination that benefits from the advantages of each material could achieve a reduction in cost. Usually, a chain is used for the fairlead connection and for the part of the line that rests on the seabed due to the higher abrasion resistance.

1.2.2.1.2 Additional devices: Buoys and clump weights Inhereted from the O&G offshore industry, additional devices such as clump weights and buoys can be used in the mooring system of a FWT. A sketch of a line with these additional devices is shown in Figure 1.4. Clump weights are usually installed near the touch-down point and they prevent the line in contact with the seabed from being lifted, and consequently, the line is stiffer compared with a uniform line. Buoys are usually installed near the connection to the floating structure, and they reduce mooring line weight unloading the fairlead. Or can be installed close to the touch-down point to avoid contact with the seabed (for example, when synthetic materials are used).

In addition, in recent years, some works have carried out an investigation on the use of clump weights and buoys, with their optimal distribution and weight in water, to improve the response of the FWT and the mooring line tensions. The discussion of the literature on this matter is left for Chapter 2.

1.2.2.1.3 Additional devices: shock loads absorbers The mooring load reduction devices or shock load absorbers are elements that are integrated into the mooring systems. They can effectively reduce both peak and average loads in FWT applications (Lozon et al.

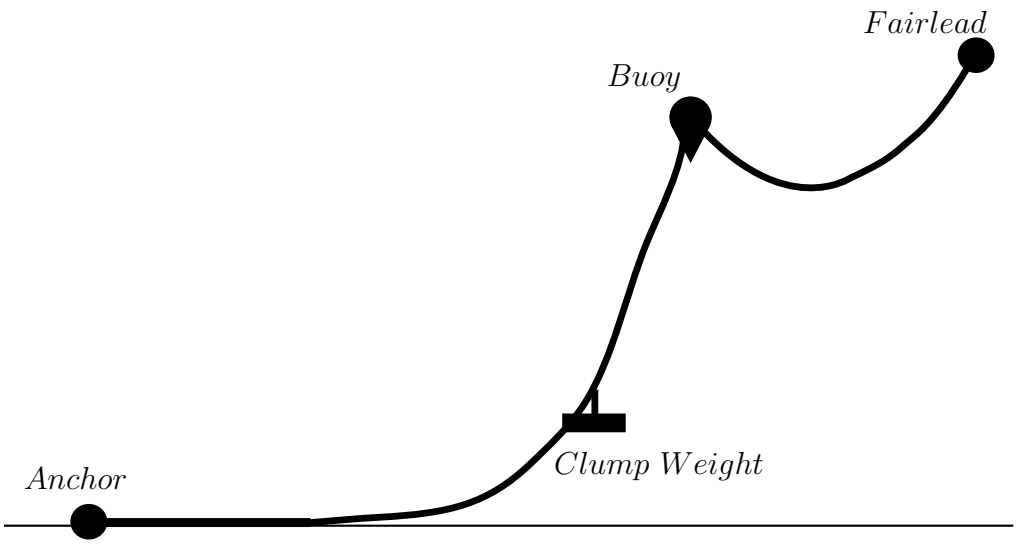

Figure 1.4: Catenary line diagram of a mooring line with a clump weight and a buoy.

[93]). Various innovative approaches, such as ballasted pendulums, thermoplastic elastomers, and hydraulic dampers, are currently being investigated and compared (Festa et al. [40]). An example of a polymer spring device attached to the mooring line is shown in Figure 1.5.

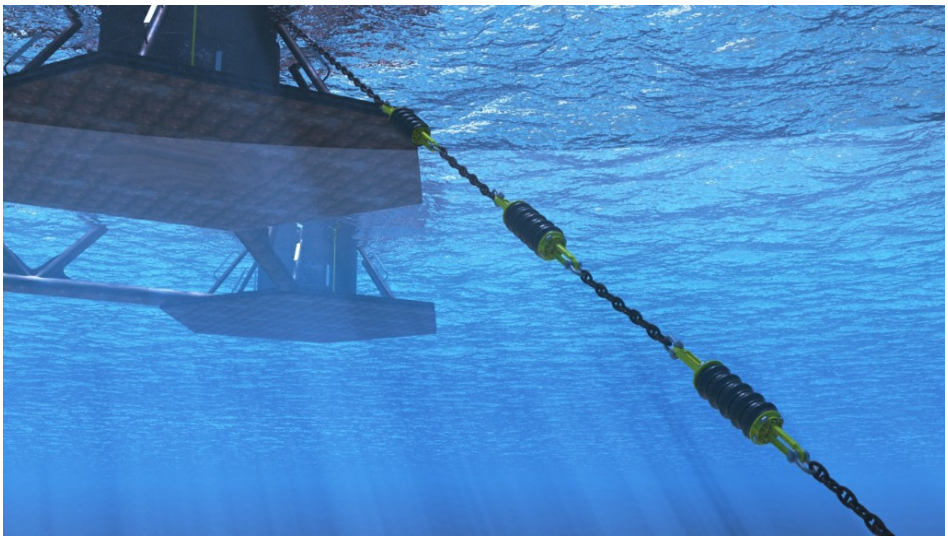

Figure 1.5: Sample of polymer springs attached to the line [97].

Although installation requires more connections on the line, these devices can enhance the mooring response to withstand environmental forces, allow the use of thinner mooring lines, lighter anchors, and prolong the operational life of systems by reducing fatigue. Such technologies are gaining traction in the design of floating offshore wind turbines (FOWTs), challenging conventional analysis and design paradigms to include non-linear effects.

1.2.2.2 Shared mooring systems

A key cost driver of an FWT project is the station-keeping system, including the mooring lines, anchors, and installation. For a farm consisting of individual floating wind turbines, each unit requires its own station-keeping system with multiple mooring lines and anchors. This redundancy results in high material and installation costs.

Among the novel cost-reduction strategies that have been investigated, the shared mooring configurations for offshore wind farms can be mentioned. Although shared moorings are further away from being understood and commercially deployed, these innovative mooring systems could achieve significant cost reductions. Even modest reductions of 10-20% in mooring costs can significantly impact lifetime project economics [129].

For a farm of N turbines, shared moorings can significantly reduce the number of lines and anchors compared to separate station-keeping systems (Chitteth Ramachandran et al. [22]). This reduction is highly dependent on the layout, but estimates indicate typical savings of 25-50% in anchors and 15-40% in total line length [129]. In addition to material savings, shared moorings reduce installation time and complexity, and therefore costs. The fewer the anchors, the lesser the time consumption in anchoring operations, while shared lines decrease cable handling. This results in less vessel days for installation. Innovative electrical network layouts also arise from direct platform connections. Overall, shared mooring systems are projected to substantially reduce FWF costs as the industry expands into deeper waters.

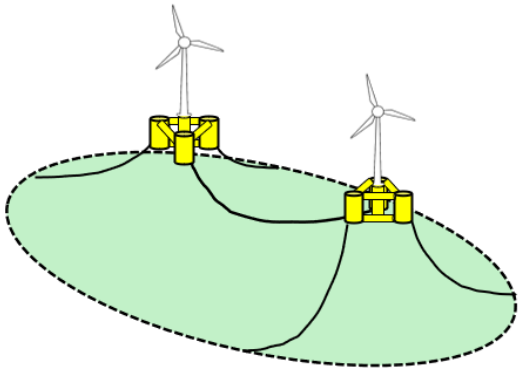

Figure 1.6: Shared mooring line between FWT.

Although offering significant cost reductions, shared mooring systems also come with design and analysis challenges that must be addressed. The main concern is the coupled dynamic behavior that arises between platforms. The motion of one turbine induces loads on the shared line that influence the dynamics of connected platforms. This interaction must be accurately modeled:

- The coupled hydrodynamic response can lead to increased or extreme motions depending on the system configuration and wave conditions. Larger excursions may occur compared to separate station-keeping. Mitigating excess platform motion is a key design consideration for dynamic cable restrains.

- Another priority is ensuring adequate system restoring to avoid resonances. Shared lines provide restoring in some modes while reducing it in others. Detailed analysis is required to achieve acceptable system stability (Lozon and Hall [92]).
- Finally, as with any new technology, the lack of operational experience creates uncertainties. Risks associated with installation, inspection, maintenance, and connection/disconnection of shared lines need to be addressed over time.

An ongoing concern with shared mooring systems is the extreme tension events and the potential for snap loads to develop in the lines. A snap load occurs when tension increases very rapidly from slack conditions, inducing a shock load.

In single platform mooring systems, extreme tension peak events typically occur near maximum platform excursion when the mooring lines become taut; this phenomenon is even more common and important in FWT in shallow water (Hsu et al. [55]). However, shared lines can experience intermittent almost complete tension loose (slack condition) and sudden tension recovery (snap condition) in certain load cases. As a loosely tensioned shared line is straightened by platform motions, acceleration generates a sudden tension spike. Snap events introduce high-magnitude fatigue loading that requires special considerations of the design of the mooring line. Mitigating snap loads can be critical to the feasibility of implementing shared mooring systems.

Despite these obstacles, research indicates that shared mooring systems can be designed to perform adequately while providing significant CAPEX reductions [129].

1.2.3 Previous and current projects

The technological evolution of FWTs has been characterized by various design approaches aimed at optimizing stability, efficiency, and cost-effectiveness. From the mentioned spar-buoy to semi-submersible and tension leg platforms, each design caters to specific conditions and challenges presented by the offshore environment.

Several flagship projects have underscored the technological and commercial viability of FWTs. The Hywind Scotland project (UK, 30 MW), for instance, became the world's first commercial-scale floating wind farm, showcasing the spar-buoy design's success. Similarly, the WindFloat Atlantic project (Portugal, 25 MW) utilized a semi-submersible platform, highlighting another effective design approach in harnessing offshore wind energy. These projects, among others, serve not only as proof of concept but also as benchmarks for the industry, providing valuable data and insights that inform ongoing research and development efforts.

A timeline of past and current projects is shown in Figure 1.7. As can be observed, the spar-buoy and semi-submersible platform concepts are the ones with more demonstration projects and pilot farms; however, there is no clear convergence in the platform choosing. Floating wind energy is still an emerging technology and is in an early stage of development.

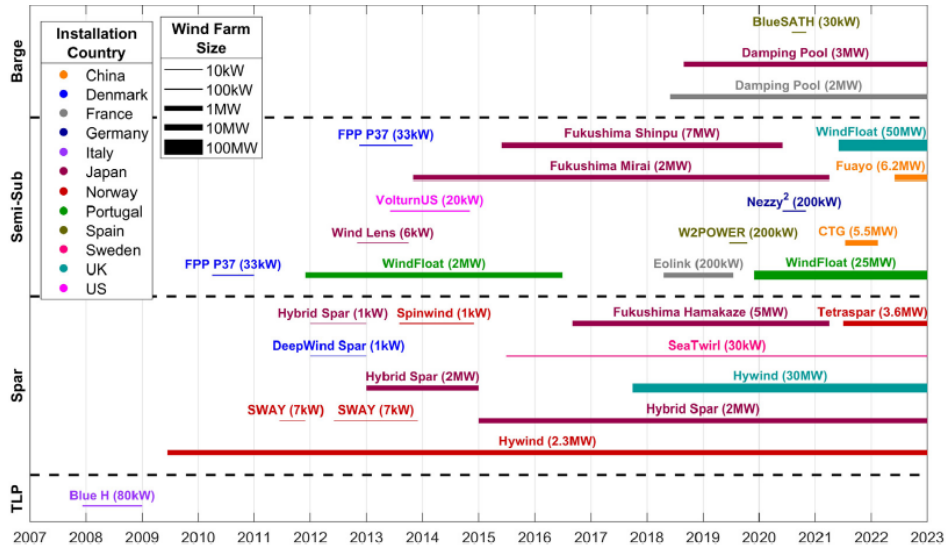

Figure 1.7: Timeline of floating offshore wind turbine deployments, including prototypes, demonstrators, and farms (Edwards et al. [37]).

1.2.4 Cost and challenges

Despite progress, FWTs face several challenges, including cost competitiveness, supply chain issues, logistic challenges of installation and maintenance in deep waters, and the need for specialized vessels. However, ongoing research and development is expected to address these challenges, improving the scalability and sustainability of FWTs.

The Levelized Cost of Energy (LCOE) for FWTs, although initially higher compared to bottom-fixed installations, has been on a downward trend (Myhr et al. [107]). This reduction is attributed to technological advances, increased turbine size, and economies of scale. The projections suggest that the FWT LCOE could become competitive with traditional offshore wind energy sources by 2030, facilitating a greater adoption of this technology (Musial et al. [104]).

The demand for the evolution of floating offshore wind technology implies the development of innovative floating platform substructures with reliable and cost-efficient mooring solutions. The total cost of the substructure and foundation (including moorings), assembly, and installation of a floating offshore wind project was estimated to be approximately 33% [104]. As the offshore wind industry has shown growing interest in locations where deep-water floating solutions are preferable, efforts to reduce these costs are needed in current and future offshore projects. For the mooring and anchoring system of a floating wind farm (FWF), novel solutions are considered necessary to achieve cost reductions in material consumption and installation.

1.3 Background and Motivation

As highlighted in this chapter, although the technical challenges that arise for floating wind energy, this technology is positioned as a key offshore technology to meet the decarbonization goals for various reasons.

It has also been clearly stated that for the demand for cost reduction of this growing technology to optimize the mooring systems, it is vital, and for this it is necessary to carry out an exhaustive and comprehensive study of their dynamics. It is crucial to know correctly the level of extreme and fatigue loads, since the components are designed on the basis of them. Consequently, the accuracy and reliability of validated computational simulation tools are important to achieve the EU's offshore wind goals [3].

A reduction in movements allows the turbine to produce electricity over a wider range of sea states, and smaller displacements reduce the stresses on the line and associated costs. Optimization of mooring systems and innovative solutions to reduce costs such as those mentioned in Section 1.2.2 emerge to address this issue.

Therefore, the main motivation behind this Ph.D. thesis is to reduce the loads on the mooring lines and enhance the motion response of FWTs. To this end, the following hypothesis is proposed. It is possible to improve the dynamics of the mooring lines by incorporating elements that increase hydrodynamic damping, added mass, and inertia; the clump weights.

1.4 Objectives

At the end of this thesis, it is intended to have carried out a complete investigation of the energy dissipation provided by the mooring system when the clump weights are attached. The expected phenomena to be observed are the achievement of a reduction in the maximum horizontal motions of floating wind turbine platforms under operating and extreme conditions; and, in addition, better analysis and prevention of impulsive loads in the mooring lines under extreme conditions when clump weights are attached.

To fully understand the dynamics of the mooring systems when clump weights are added, the physics involved is extensively studied at different scales of "zoom levels". The study starts with the problem on the smaller scale of the clump weight itself up to the broader level, a complete floating wind farm with clump weights attached on the mooring lines. Figure 1.8 illustrates these "zoom levels". Based on that, a series of specific objectives are established:

1. Establish the hydrodynamic forces contribution of the clump weights to the mooring line.
2. Extend the capabilities of the numerical tool OPASS for mooring line dynamics: implement the inclusion of clump weights along the mooring line.
3. Investigate the influence of clump weights when attached to the lines of various mooring systems configurations for FWTs.

4. Determine the influence of the clump weights in the tensions of shared mooring lines of FWFs and the impact on the multibody dynamics.

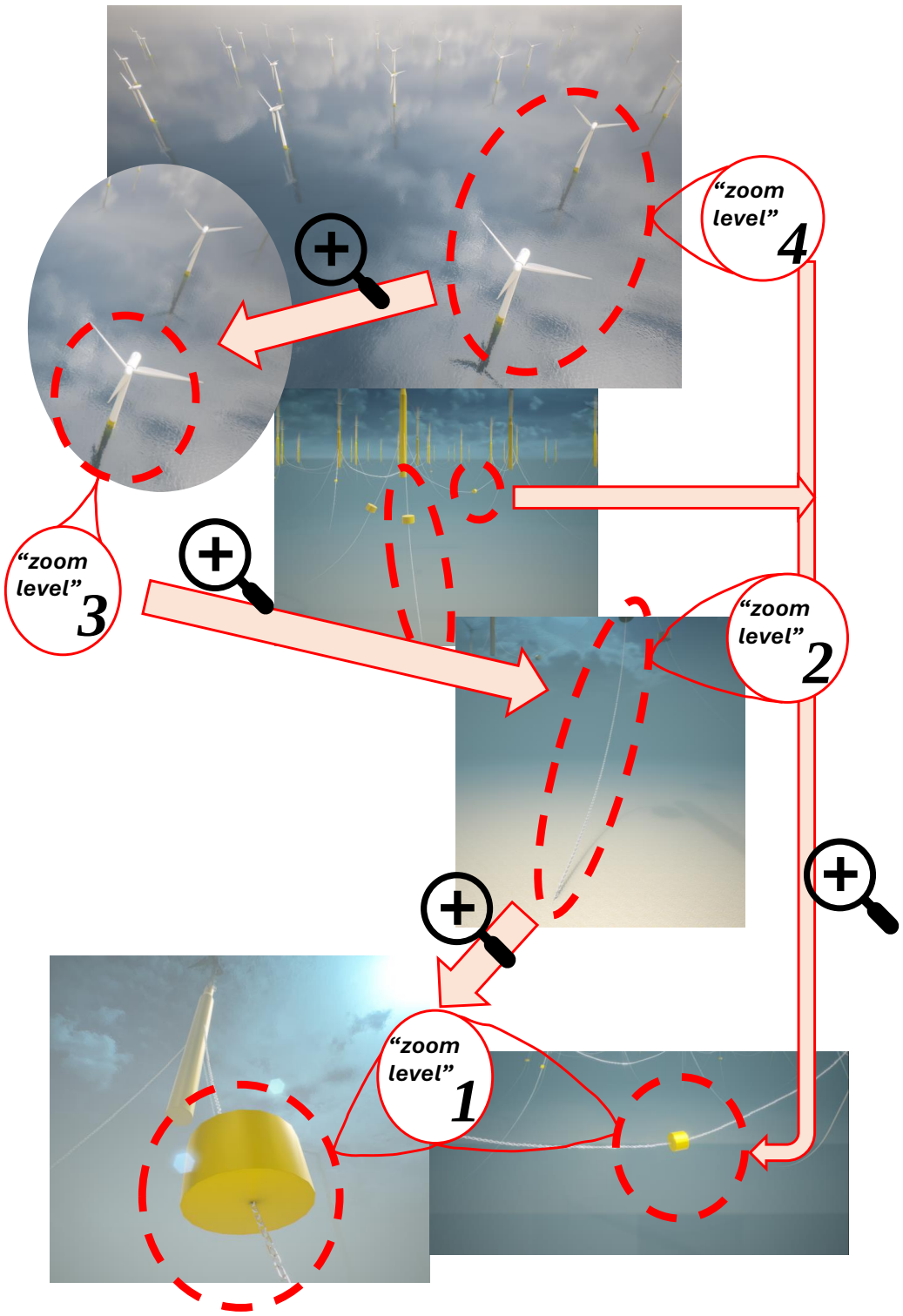

Figure 1.8: Scope of the thesis and the different "zoom levels".

1.5 Structure of the Thesis

Various tasks were carried out to fulfill the thesis objectives listed above. These tasks are carried out in a series of chapters. Each chapter is intended to cover the physics phenomena involved in each of the "zoom levels" previously described. Then, the document is organized as follows:

1. A general overview of the floating offshore wind industry is described in **Chapter 1**, where the different mooring solutions for FWTs are also discussed.
2. A thorough investigation of the state of the art of methods currently adopted to analyze the different physics involved in each of the proposed "zoom levels", as well of the different mooring systems of FWTs and FWFs is carried out in **Chapter 2**.
3. **Chapter 3** considers the hydrodynamics of an impulsively started circular disk-shaped clump weight. The hydrodynamic forces contribution of this inertial element to the mooring line dynamics is studied in this chapter.
4. **Chapter 4** describe the inclusion of the clump weight along an isolated mooring line. This chapter deals with theoretical aspects of the numerical implementation into a dynamic mooring line code based on lumped mass formulation: OPASS, the code used in part of this PhD thesis and compared with another computational software. Experimental validation of the numerical results, as well as energy dissipation aspects, is also studied.
5. A set of numerical OpenFAST simulations and experimental tests are presented in **Chapter 5**. The inclusion of the clump weights in catenary mooring systems for FWTs is studied in this chapter.
6. Finally, in **Chapter 6** the inclusion of a clump weight to reduce the snap loads in shared lines of FWFs is analyzed.
7. General conclusions and future works are left for **Chapter 7**.

Chapter 2

State of the art

As highlighted in Section 1.5, the methodology adopted in this thesis is to experimentally and computationally analyze the effects of the presence of a clump weight on the mooring lines of floating wind turbines at different "zoom levels". In this chapter a thorough investigation of the state-of-the-art of methods currently adopted to analyze each of the different "zoom levels" that are proposed in this Ph.D. thesis is performed in the following subsections.

In the following chapters, the research gaps encountered in this extensive review are tried to be filled in four different chapters, one for each of the different "zoom levels".

2.1 Clump weight hydrodynamics

The impulsive start of a bluff body in a viscous fluid has been studied extensively for many years. Many works are recursively found in the literature for a wide range of Reynolds numbers and object shapes, all of them following different approaches to the problem: numerical and/or experimental studies.

There are certain challenges related to this problem. For example, the complexity of the problem increases as the Reynolds number does, and hence the experimental references in the literature for Reynolds numbers higher than 10,000 are very scarce, especially when the hydrodynamic forces are measured. Furthermore, more challenges arise with the physical modeling of the pure impulsive start and when trying to model a 2D case, which in reality is 3D. Experimentally, Coutanceau and Bouard [25, 26], Bouard and Coutanceau [8] are one of the first approaches to the problem. The common shape of the cylinder is chosen for these works in which the main features of the hydrodynamic field of the flow are extensively studied. Specifically, the wake and the velocity distribution behind the cylinder are shown, but the forces are not measured.

Following this problem, in the past decades, several numerical research papers have been published aiming to validate some of these works. The works of Chang and Chern [17] and Koumoutsakos and Leonard [77] are the most outstanding ones, in which using a vortex

method the main flow characteristics are validated. Furthermore, although discrepancies are found in the results between these two works, the drag coefficient C_d is estimated using a numerical approach. In the following years, more numerical works have been published using different numerical methods: vortex methods (Cheng et al. [21], Ploumhans and Winckelmans [115]), the Lattice-Boltzmann method (Li et al. [80], Dupuis et al. [36]), and Smoothed Particle Method, SPH (Rossi et al. [122], Muta and Ramachandran [105]).

Up to this point, all the works that have been analyzed in this section considered the bluff body static while the flow passed over it. The equivalent problem of the static flow and the bluff body moving inside of it can be considered with some particular considerations. More recently, the experiments performed by Tonui and Sumner [133] studied the impulsive start of a bluff body moving in a still fluid and determined the wake formed by image processing. But, in general, further research work regarding the impulsive motion of an object is necessary, especially when it comes to measuring hydrodynamic forces over the object.

During all the years of numerical fluid dynamics, when using the Finite Volume Method, it has been clearly established that the mesh grid quality significantly affects numerical solutions. While high-quality structured grids can be generated for studying flows around a bluff body, maintaining grid quality becomes challenging when considering the motions of the object. In contrast, the overset technique is a relatively novel approach in Eulerian techniques that helps addressing problems with large motions as it avoids mesh deformation, maintaining grid quality. Throughout a simulation, each component grid element retains its shape, and body motions are simulated based on the relative positions of the various component grids. This approach ensures that grid quality is preserved regardless of the amplitude of body motions. Because of this, this technique has gained significant popularity in the last decade.

This is a relevant problem in many engineering applications, and therefore numerous studies have used overset grids for the mentioned reason in different contexts where large body motions can be expected: in the context of benchmark cases (Ye and Wan [144], Chandar [16], Chen et al. [19]); in the context of ship hydrodynamics (Shen et al. [125], Wang et al. [135]); and in the context of offshore renewable energies (Pinguet et al. [114], Katsidoniotaki and Göteman [74], Chen et al. [18]).

In the case of floating offshore wind applications, the clump weights installed and the mooring lines in which they are installed can suffer from these impulsive loads. Following in a similar way the Morison approach [102], this problem has traditionally been assessed with a linearized drag and an added mass coefficient provided in class rules and recommendations (i.e. DNV-OS-E301 [30]). For example, Xu and Huang [141] evaluated the drag coefficient of a studless chain with LES and RANS simulations, arriving at a similar value of the recommended coefficients.

In general, in the context of offshore wind, the hydrodynamic characterization of the impulsive start of a bluff body (for example, a clump weight), is lacking in the literature, especially validated with experiments. Chapter 3 aims to address this important research gap.

2.2 Isolated mooring lines: Fairlead prescribed motions in forced oscillations

Research on mooring systems admits different classifications, one of them being the methodology used. Most of these methodologies are experimental ones that use scaled models and numerical ones where full-scale models can be employed. In addition, there are a large number of published articles in which both approaches are used. In this section, the current and past research work on isolated mooring lines is thoroughly analyzed and classified by the two types of experiments/simulations.

The role of the mooring system has a significant contribution to the motion of floating structures, causing about 80% of the total damping of the structure at 200 m depth (Huse [56]). This energy dissipation is basically caused by three terms: hydrodynamic contribution, friction with the seabed, and the internal mechanical damping due to line deformations. Apart from this work, other available in the literature estimate this dissipation also with forced oscillations [136, 142]. The most commonly used method to estimate total mooring dissipation is the indicator diagram presented in Webster [136], which has the advantage of including all dynamic responses of the mooring line.

In the literature a vast number of works focusing on the mooring dynamics and the different regimes found for different kinds of excitation are also found. The works of Kitney and Brown [75], Bergdahl et al. [7], Barrera et al. [4] extract important conclusions in terms of dimensional analysis and show how the line should be scaled not only with Froude number (gravity forces), but also with other non-dimensional numbers such as the one associated with line stiffness by adding a spring at the anchor position. One crucial conclusion of these works is that even when using a spring connected to the mooring line, in order to have a scaled material stiffness, a correct scaling is only obtained at quasi-static level. If perfect geometrical and dynamic scaling in vacuum is addressed, the chain must be scaled to have an adequate propagation celerity for longitudinal elastic waves.

Some experiments can measure the trajectories and velocities of different points on the mooring line. Different techniques are applied to this process: either image processing methods are applied to snapshots from the camera [55] or sophisticated optical devices such as Qualysis to directly obtain the point position [4]. During experiments carried out in Hsu et al. [55] in shallow water, the importance of line stretching was demonstrated for damping, also showing that the most critical factors for snap conditions are high pretensions and low amplitudes and periods. A similar study was performed by Gao et al. [42] but also adding a uniform current to the surge and heave fairlead oscillations. A sharp increase in the maximum tension force was observed at high pretension for the mooring line with the imposed surge and heave motions.

From the numerical point of view, the computation of the mooring energy dissipation has been computed using quasi-static methods when the motion of the mooring line is very slow; see Huse [56]. For the numerical calculation of the mooring line dynamics, the OPASS code based on the finite element method was developed by Azcona et al. [2]. Other numerical alternatives such as Open-Moor software, similar to OPASS, is explained in Chen and Basu [20]

and validated against the forced isolated mooring line described in Bergdahl et al. [7]. Current simulation codes for FWTs that include mooring dynamics using the finite element method are MoorDyn (Hall and Goupee [49]), SeaFeam (Gutiérrez-Romero et al. [46]), SimoRiflex [127, 126], OrcaFlex [111], etc.

In [117], the important slack-taut phenomenon was searched by numerically changing the initial pretension, amplitude, and frequency of the fairlead excitation. The results showed that the slack-taut phenomenon, characterized by maximum tensions several times that of pretension, would occur beyond a certain threshold of amplitude, frequency, and pretension.

In addition, numerous works that combine both numerics with its experimental validation with forced oscillations are found in the past decade. The OPASS code was successfully validated in Azcona et al. [2]. A numerical validation study of Barrera et al. [4] was carried out in Barrera et al. [5], where an exhaustive sensitivity analysis was performed to evaluate the variability of mooring loads because of inaccuracies in the definition of model inputs. A nonlinear dynamic model of the mooring line based on FEM simulations was formulated in Li et al. [81] and validated with the experiments of Azcona et al. [2]. An isolated mooring line was tested for a large combination of parameters: pretension, amplitude and frequency, diameter, and modulus of elasticity. They concluded that the material stiffness of the mooring lines presents a hysteresis behavior that becomes more obvious as the suspension point frequency/amplitude gets larger. In Crudu et al. [27], a numerical and experimental study was performed for five different scales of chain mooring systems. They compared the different theoretical approaches to the problem showing the difference to the static case, where no terms including velocities or accelerations were part of the model; the quasi-static case where no terms based on accelerations were considered; and finally, the dynamic approach where accelerations and added mass forces were included.

The improvement given by the clump weights was demonstrated in Luo [95] where the key design parameters of the clump weights and their effects on the performance of the mooring system were investigated from a quasi-static point of view and assuming that dynamical effects can be neglected. The article described a methodology for determining the optimum values of these parameters to improve mooring performance.

We should remark that in this kind of research, where an isolated mooring line is studied under forced movement, only a few papers mention the presence of a clump weight, especially combining the experimental and computational perspectives. A numerical-experimental comparison was made in Nakajima et al. [108] where a lumped mass computational method was described and compared to experiments carried out in a towing tank. Both approaches were performed using a single clump weight and limiting the study to a single frequency and amplitude. Some computational models analyzed implemented the clump weight as part of the lumped-mass approach, where the total mass of the element (chain and clump weight) is concentrated in the element's adjacent nodes; see, for example, Hermawan and Furukawa [50], Hall [47].

In summary, Table 2.1 compares the state-of-the-art of forced excitation of isolated mooring lines. As shown, most of the research work in which the mooring lines are studied did not include the innovation of clump weights, either in the experiment or in the dynamic numerical

simulation. Chapter 4 aims to address this research gap.

Table 2.1: Comparison table of the existing research literature of mooring lines forced oscillations.

	Methodology	**Results**	**Use of Clumped Weights**
Nakajima et al. [108]	Experimental and numerical	Fairlead tension time series, frequency response curves of tension. Single frequency and amplitude with clumped weights.	Yes
Luo [95]	Numerical	Dynamic analysis of tension response for different positions of clumped weights.	Yes
Azcona et al. [2]	Experimental and numerical	Fairlead tension, force-displacement curves, trajectories, and numerical validation with experiments.	No
Li et al. [81]	Experimental and numerical	Time series of fairlead tension, trajectories, force-displacement curve, dissipated energy, comparison of maximum fairlead tension with the static.	No
Barrera et al. [5]	Experimental and numerical	Experimental fairlead tension time series comparison with numerics, Experimental time series of the displacement for different points of the line compared with numerics, sensivity analysis of the number of elements and computational parameters.	No
Bergdahl et al. [7]	Experimental and numerical	Fairlead tension time series compared with numerics.	No
Yan et al. [142]	Experimental and numerical	force-displacement curve and energy dissipation.	No
Barrera et al. [4]	Experimental	Time series of fairlead tension, fairlead tension-displacement curves, trajectories, accelerations, dissipated energy, sand footprints, hydrodynamic response with different sea states	No
Kitney and Brown [75]	Experimental	Force-displacement curves and energy dissipation, non dimensional analysis.	No
Gao et al. [42]	Experimental	Force-displacement curve, fairlead tension and PSD analysis, trajectories	No
Hsu et al. [55]	Experimental	Force-displacement curve, energy dissipation and mooring line velocity vectors of image processing.	No
Chen and Basu [20]	Numerical	Fairlead tension time series, validation with experiments in the literature.	No
Qiao et al. [117]	Numerical	Fairlead tension time series and PSD analysis, trajectories.	No
Webster [136]	Numerical	Force displacement curves and energy dissipation, non dimensional analysis.	No

2.3 Mooring systems of FWTs

As mentioned in Section 1.2.1, among the different concepts of the FWT platforms introduced in [14], we can find the Spar and Semisubmersible concepts leading future project prospects. Also, since the focus of this thesis is on catenary mooring lines, only these two types of platform are analyzed in this state-of-the-art review. Several approaches are found to understand physical behavior and to demonstrate technical feasibility of FWTs are found: complex fully coupled simulation tools and model scale experiments.

Firstly, the spar-buoy concept, widely studied in the literature, is a ballast-stabilized buoy type and was the first used in a commercial project [128]. The OC3-Hywind spar-type platform is one of the most widely studied, multiple numerical and experimental works have been published to understand the dynamic responses of this type of FWT under various environmental conditions.

Among the different important experimental works in the past years, we can mention the following. Nielsen et al. [109] carried out 1:47 model-scale experiments of the Hywind concept at MARINTEK (now SINTEF). The focus of this work was to test several coupled environmental conditions that were challenging to the dynamics. 6 DoFs motion, fairlead tensions, and structural response data were obtained and validated against a numerical simulation. The difficulty of the numerical model to capture the low-frequency response in surge was shown. Later on, Myhr et al. [106] compared the responses of both a TLP and OC3-Hywind concepts numerically and experimentally. With a special mooring system configuration, the 1:100 model tests showed significantly smaller motions and higher anchor tensions for the TLP when comparing. Koo et al. [76] and Goupee et al. [45] carried out a series of experiments with three different concepts of FWTs. The 1:50 models (semisubmersible, spar and TLP) were tested under several wind conditions survival sea states founding the global performance. The spar concept showed how the wind load increased the wave-frequency motions and how the surge motion was considerably lower than the other concepts. Tomasicchio et al. [132] carried out OC3-Hywind 1:40 model tests at DHI Offshore Wave Basin. The truncated mooring line technique was adopted with good results because of the depth limitations of the ocean basin. The dynamic performance in terms of motions, accelerations, and forces showed that they occur mainly at the wave frequency, with some components at the first and second harmonics. Russo et al. [123] carried out experiments at the Danish Hydraulic Institute of a 1:40 downscaled OC3-Hywind model with pitch controlled variable-speed blades. Different wind and wave operational conditions were tested and the importance of this inclusion in physical tests was concluded to assess a great influence on the overall structure dynamics. Xu and Day [140] investigated experimentally the dynamic performance of the OC3-Hywind with a 1:74 scale model subjected to several wave conditions at the Kelvin Hydrodynamics Laboratory (KHL). In this study, the original water depth of the full scale prototype was changed and a mooring redesign is proposed. The focus of this work was to study the hydrodynamic response of the spar and the dynamics of the mooring lines. Snap phenomena were detected during the regular wave test.

Other spar-buoy concepts than OC3-Hywind have been tested in ocean basins. Utsunomiya et al. [134] tested a spar-type 1:22.5 scale model at the NMRI (National Maritime Research

Institute) and compared against numerical results. Motions were analyzed and Response Amplitude Operators (RAOs) were determined in good agreement with the simulation tool for the wave frequency range, but further improvement was necessary in the damping force evaluations. Meng et al. [100] proposed a 6MMW Spar-buoy FWT for 100 m water depth and investigated it on a series of experiments of the 1:65.3 model and numerical analysis in FAST. Wave-only, wind-only, and wind-wave combined tests were carried out. In addition, natural frequencies from the decay test and mooring stiffness curves for the delta lines were obtained. Wind and current forces appeared to damp the low-frequency response, something that was also observed in the experiments carried out by Duan et al. [35].

Evidence of the presence of impulsive loads and tension peaks in mooring lines of FWTs has been studied in various publications (Shah et al. [124], Hsu et al. [53]). Masciola et al. [98] demonstrates the importance of having a good dynamic model of mooring lines for the analysis and prevention of extreme load events, as well as in regular wave situations.

An interesting study carried out at MARIN (Netherlands) at a 1:50 scale (Hsu et al. [52]) confirms that the risk of impulsive loads on floating wind turbines is significant, showing a strong correlation between waves, horizontal motions of the fairlead and tension peaks in the line. A threshold criterion derived from the crane wire lifting and lowering standards of DNV is proposed to determine the occurrence of snap events. In a later work, Hsu et al. [54] presents a statistical methodology to predict the occurrence of snap events. It is important to note that numerical models needs to capture this impulsive load physical phenomenon, besides the experiments.

One mooring solution that has been widely explored in the offshore industry is the mooring system with clump weights. If a proper design is made, they can achieve motions reductions for station-keeping purposes [65] while increasing the line dynamic tensions [95, 65]. In a later work of Cabrerizo-Morales et al. [11], in the context of offshore operations, the mitigation of the slack/snap phenomenon including clump weights in the line is proposed.

When the installation of the FWT is in shallow to intermediate water depth (50 to 100 m), mooring system challenges appear, and special interest for the use of clump weights has been raised in recent years. Footprint reduction, material savings, lower utilization factor are among the desired outcomes, consequently, cost reductions can be achieved. However, mooring system designs for FWT are quite different and require special care due to the considerable reduction in water depth.

Several experimental and numerical works highlight the influence on surge motions and line tensions when clump weights are attached. Jang et al. [64] found that the surge and sway excursions increase while the pitch and line tensions decrease. The strategic incorporation of a heavy chain or clumps is necessary to attain adequate pretension and stiffness characteristics, as it was concluded by Xu and Day [140]. Different effects were demonstrated depending on the position of the clump weight in Cao et al. [13]; if clumps are added on the suspended length of the catenary or at the sea bottom part, where dynamic line tensions increase, but in all cases the horizontal offsets and mooring footprint are reduced.

For deep water site installations, there is a lack of investigations of these mooring systems for FWT. The works of Liu et al. [88] and Bruschi et al. [10] studied numerically the influence of

mooring systems with clump weights on a spar-buoy FWT. Different positions and masses of the weights were adopted in these works, the general conclusions of which determined the reduction of the horizontal motions and the increase of the fairlead tensions. However, the seakeeping benefits of the addition of clump weights to the FWT mooring system at deep water sites are yet to be fully understood. Chapter 5 aims to address these research gaps.

2.4 Shared mooring systems of FWFs

The demand for the evolution of floating offshore wind technology implies the development of innovative floating platform substructures with reliable and cost-effective mooring solutions. As mentioned in Chapter 1, the current and future designs of floating wind farms are driven by the reduction of LCOE. Efforts are needed to reduce the mooring and anchoring systems, especially with the growing interest in deeper waters. Novel mooring solutions such as shared anchors and shared mooring systems have been introduced in the last few years as promising prospects. Cost can be lowered by reducing the number of anchors, and hence the installation costs; and shared lines can decrease the capital expenditure by reducing the total length of the mooring lines and the number of anchors. However, the principles of shared mooring are yet to be further understood prior to any practical implementation.

Shared mooring systems for spar platforms have been studied in recent years in several numerical works. The elastic catenary theory for hanging cables was used to model the shared line of a dual-spar FWF in Liang et al. [82]. In a subsequent study, Liang et al. [83] investigated the natural periods of a dual-spar FWF with a shared mooring system. The anchor lines were designed based on analysis of a single FWT. Different mooring properties were studied and a sensitivity study was performed to evaluate their contributions. The shared line showed a primary influence on the surge and sway natural periods. Following those studies extreme scenarios are studied focusing in different aspects of the problem. The influence of wind was studied in Liang et al. [84]; in Liang et al. [85] different loading directions and pretensions were studied to understand the influence on the dynamic responses of the FWF; and different innovating mooring solutions like using tethered buoys were investigated and compared to alternative layouts in Liang et al. [87]. Wilson et al. [139] studied the optimization of shared mooring systems using a linearized model for the force-displacement relationship of floating platforms. The study showed that the more complicated the shared layout is, the greater the restoring demand for the shared lines. Lozon and Hall [92] studied an array of 10 FWT of 10MW with a shared mooring system with clump weights and shared anchors to set as a benchmark case for the FAST.farm code. The work showed that the shared moorings do not add major concerns to the FWF design and can achieve potential cost savings, both CAPEX and OPEX.

Similar works on FWFs with floating platform concepts other than spars can be found with similar conclusions. For example, semi-submersibles FWF with shared mooring have been studied by Goldschmidt and Muskulus [43], Hall and Connolly [48], Connolly and Hall [24]. In conclusion, overall, FWFs with shared mooring can achieve great cost reduction potentials compared to FWFs that consist of single platforms, but larger platform motions and mooring

tensions can be the trade-off in extreme environmental conditions.

Considering the above literature review, a lack of experimental literature on the hydrodynamics of FWFs with shared mooring systems is observed, a key aspect in the validation and calibration of numerical models. Also, although clump weights are added in some of the mentioned numerical works, there is not a clear analysis of the influence of their addition on the dynamic performance of the FWF. Chapter 6 aims to address these research gaps.

Chapter 3

Hydrodynamics of impulsively started clump weights

3.1 Abstract

The objective of this chapter is to extend current research on transient drag and impulsively started bluff bodies to a device added in the mooring lines: the clump weight. Therefore, in this experimental and computational study, the focus is set on the hydrodynamics of the device itself at "zoom level" 1, isolated from the dynamics of the mooring line.

This Chapter presents a series of computational fluid dynamics (CFD) simulations of a transient flow past a circular cylinder and a disk. The flow is modeled using an effective turbulent transport equation. Numerical results are verified with the simulation results in the literature and validated with the experimental campaign conducted in the towing tank at the Universidad Politécnica de Madrid, CEHINAV.

3.2 Experiment descriptions

The objective of the experiment is to measure the hydrodynamic forces involved in the movement of a scaled clump weight with a typical constant acceleration motion with an impulsive start. The experimental set-up and the dimensional analysis are described in detail in the following subsections.

3.2.1 Experimental set-up

The experimental campaign was carried out in the towing tank at the *Canal de Ensayos Hidrodinámicos* (CEHINAV) of the Universidad Politécnica de Madrid. The main dimensions of the tank are 100 m in length, 3.8 m in width, and 2.245 m in depth. The experimental setup is depicted in Fig. 3.1.

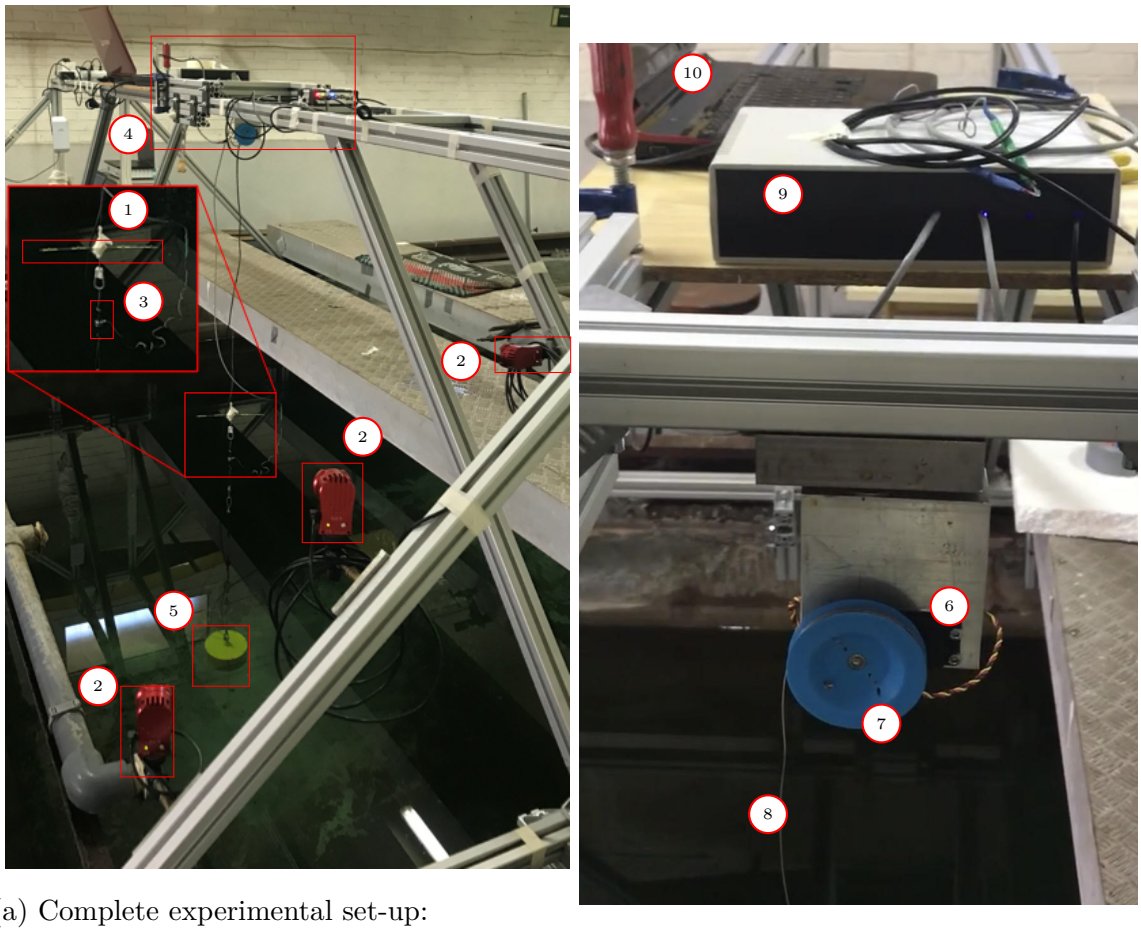

(a) Complete experimental set-up: (1) tracking markers, (2) tracking cameras, (3) load cell, (4) Actuation ensemble, (5) scaled clump weight.

(b) Actuation ensemble: (6) Servo-motor, (7) Pulley, (8) Lifting cable, (9) Arduino control system, (10) Controlling computer.

Figure 3.1: Experimental set-up.

The actuation ensemble can be observed on label 4 in Fig. 3.1a and each component is shown in detail in Fig. 3.1b. The motion of the clump weight was possible thanks to a 360°, Brushless, High Voltage, Titanium Gear Actuator Hitec model HSR-M9382TH. An Arduino program modeled and controlled the motion of a pulley. In this pulley, a flexible steel wire was rolled and attached to the clump weight. When the actuation system was triggered, the pulley rotated in such a controlled way that the wire would wind up and lift the object, following the programmed motion law described in the following section.

The movements of the clump weight underwater were recorded with three OPTITRACK-Flex 13 cameras (see label 2 in Fig. 3.1a). These marker-based optical tracking cameras were placed taking into account space restrictions, obstructions, and light conditions. To maximize tracking precision, the conclusions and recommendations of Furtado et al. [41] were followed. The cameras have a resolution of 1280 x 1024 or 1.3 megapixels and a 5.5 *mm* lens. The maximum frame rate is 120 fps. Passive tracked objects (mini-markers) were chosen because

they are widely used for validation and control in indoor laboratory settings. The trackers are small spherical markers that were placed on a rigid transverse cylindrical rod that remained outside the water for all tests (see label 1 in Fig. 3.1a). This solution was adopted to prevent the markers from getting wet to avoid reflection and refraction problems. The camera system was calibrated before each test with a maximum mean 3D re-projection error of 0.650 mm.

The tension of the lifting line was measured through an HBM one-component load cell with a full SG bridge (see label 3 in Fig. 3.1a). The measured range of the load cell was 0–10 N and the precision of the load cell was ±0.015 N. The sampling rate of the load cell was 50 Hz.

During the whole test, the clump weight moves below the free surface. The initial position of the clump weight can be observed in label 5 in Fig. 3.1a. To avoid unwanted interactions with the moving object, the clump weight is sufficiently far from the bottom of the towing tank and the free surface in both the initial and final position of the motion, respectively.

In summary, the experimental outputs are the tension in the lifting line of the object and the position of the clump weight at each time instant.

3.2.2 Dimensional analysis

For the dimensional analysis, we consider the dynamic equation for the clump weight when moving in water according to the free body diagram of Fig. 3.2 in a fixed reference system. This equation will include the tension of the pulling line, the external volumetric forces (weight), the external hydrodynamic forces (viscous drag and added mass), and the hydrostatic forces (buoyancy).

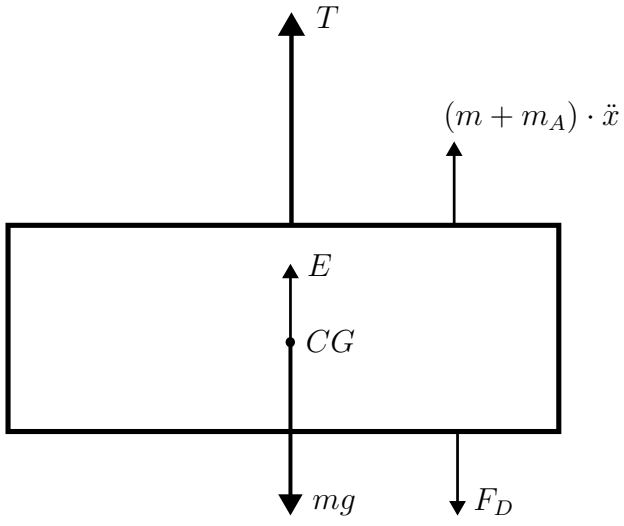

Figure 3.2: External forces acting on the scaled clump weight.

$$\mathbf{T} + \mathbf{E} - m\mathbf{g} - \mathbf{F_D} = (m + m_A)\ddot{\mathbf{x}} \ , \tag{3.1}$$

where $\mathbf{T}$ is the tension in the line, $\mathbf{E}$ is the buoyancy of the clump weight, m is the mass of

the clump weight, m_A is the added mass, $\mathbf{g}$ is the gravity acceleration, $\ddot{\mathbf{x}}$ is the clump weight acceleration, and $\mathbf{F_D}$ is the viscous drag force. Note that the bold text denotes vectorial notation.

From Eq. (3.1), we can obtain the following expression:

$$T = \frac{1}{2}C_D A_0 \rho_0 U^2 + \frac{1}{3}\rho_0 D^3 a + \rho \mathbf{g} V_0 - \rho_0 \mathbf{g} V_0 + \rho V_0 a \ , \tag{3.2}$$

where C_D is the drag coefficient, A_0 is the projected area of the clump weight, ρ_0 is the water density, U is the characteristic velocity in the dimensional analysis for the clump weight, a is the characteristic acceleration in the dimensional analysis for the clump weight, V_0 is the volume of the clump weight (since it is the shape of a circular disk, it results in $V_0 = A_0 \cdot e = \frac{\pi D^2}{4}e$), and m_A is the added mass that has been modeled with the theoretical formulation for a circular disk as $\frac{1}{3}\rho_0 D^3$ ([131]).

Both sides of the Eq. (3.2) are divided by $\rho_0 D^2 U^2$ to make them non-dimensional. The first term of the right side of the resulting equation is the non-dimensional viscous drag force, the second term is the non-dimensional added mass force, the third and fourth terms are the non-dimensional submerged weight of the moving object, and the last term is the non-dimensional mass inertia force.

$$\frac{T}{\rho_0 D^2 U^2} = \frac{C_D \frac{1}{2}\frac{\pi D^2}{4}\rho_0 U^2}{\rho_0 D^2 U^2} + \frac{\frac{1}{3}\rho_0 D^3 a}{\rho_0 D^2 U^2} + \frac{\rho g \frac{\pi D^2}{4} e}{\rho_0 D^2 U^2} - \frac{\rho_0 g \frac{\pi D^2}{4} e}{\rho_0 D^2 U^2} + \frac{\rho \frac{\pi D^2}{4} e a}{\rho_0 D^2 U^2} \tag{3.3}$$

This equation can be mathematically reduced to Eq. (3.4) and can be expressed with the list of non-dimensional parameters as shown in Eq. (3.5):

$$\frac{T}{\rho_0 D^2 U^2} = \frac{\pi}{8}\left[C_D(Re) + 2Fr_g^2 \frac{e}{D}\left(\frac{\rho}{\rho_0} - 1\right) + 2Fr_a^2\left(\frac{e}{D}\frac{\rho}{\rho_0} + \frac{4}{3\pi}\right)\right] \tag{3.4}$$

$$\frac{T}{\rho_0 D^2 U^2} = f\left(Re, \frac{\rho}{\rho_0}, \frac{e}{D}, Fr_g^2, Fr_a^2\right) \tag{3.5}$$

Eq. (3.5) represents the dependence of the non-dimensional tension in terms of the rest of the non-dimensional numbers. For the motion of the clump weight, an amplitude A of 5 m and a period T of 10 s in full scale are selected, which are close to those used in Lopez-Olocco et al. [89]. The reference velocity and acceleration in full scale are obtained by $A \cdot (2\pi f)$ and $A \cdot (2\pi f)^2$, respectively.

In this experimental campaign, the dimensional properties of a typical clump weight used in the offshore industry are scaled down using a scale factor $\lambda = 10$. The density ratio ρ/ρ_0 in full scale is 7 (cast iron) and on the model scale is 1.2 (resine). The resulting properties of the clump weight are shown in Table 3.1. and the clump weight used in the experiments is shown in Fig. 3.3.

Figure 3.3: Designed and manufactured scaled clump weight.

Table 3.1: Scaled clump weight properties

	Full-scale	Model-scale $[m]$
Diameter (D)	1.67 $[m]$	0.167 $[m]$
Thickness (e)	0.76 $[m]$	0.076 $[m]$
Mass (m)	11.5 $[Tn]$	2.153 $[Kg]$

Assuming an equal Fr_a for both scales and the previous frequency and amplitude values at full scale, we obtain an acceleration of 0.033 m/s^2 for the experiments. This acceleration is achieved in the green area depicted in Fig. 3.4, where the maximum Reynolds number reached is around 3×10^4; the other colored boxes correspond to the deceleration stage (yellow) and when the weight of the clump does not move (red zone).

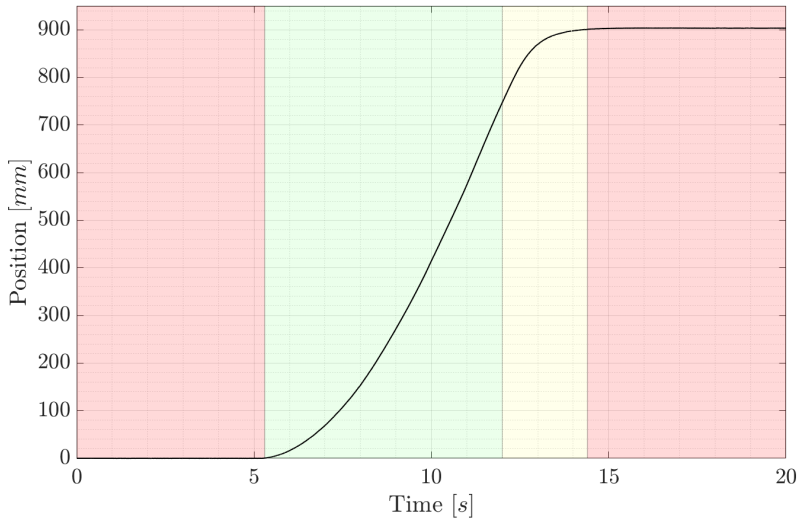

Figure 3.4: Motion law applied to the Arduino controller.

3.3 Numerical model

In this section, the numerical model that has been used is presented. The present work has been carried out with the ESI open-source software OpenFOAM® v2312. As can be concluded from this section, when dealing with overset meshes as in this work, the numerics required in OpenFOAM are quite demanding. This discussion is left for Section 3.6.

3.3.1 Governing equations

All simulations carried out in this work have been carried out with the OpenFOAM-built solver *pimpleDyMFoam*. This is an incompressible transient Reynolds averaged (RANS) model for one single fluid. Therefore, the governing equations for an incompressible fluid in OpenFOAM are [51]:

$$\begin{aligned} &\nabla \cdot \mathbf{u} = 0 \\ &\frac{\partial \mathbf{u}}{\partial t} + \nabla \cdot (\mathbf{u}\mathbf{u}) = -\nabla p^* + \nabla \cdot \tau \,, \end{aligned} \tag{3.6}$$

where $\mathbf{u}$ is the velocity field, p^* the kinematic pressure (p/ρ), and τ the shear rate tensor.

3.3.2 Turbulence modeling

The solver *pimpleDyMFOAM* allows turbulence modeling by different means. In this work, a Reynolds Average Navier Stokes approach (RANS) is used combined with an effective turbulent transport equation. The RANS approach is based on averaging in time the fields in a sufficiently long time period, e.g. for the velocity field:

$$\mathbf{u}(\mathbf{x}, t) = \bar{\mathbf{u}}(\mathbf{x}, t) + \mathbf{u}'(\mathbf{x}, t), \tag{3.7}$$

with $\bar{\mathbf{u}'} = 0$ for the reason explained above.

The corresponding equation for the effective transport to be solved is done from the effective shear rate term as follows:

$$\nabla \cdot \tau = \nabla \cdot \left(\nu_{\text{eff}} (\nabla \mathbf{u}) + \nu_{\text{eff}} (\nabla \mathbf{u})^T \right) = \nabla \cdot \left(2\nu_{\text{eff}} \left[\frac{1}{2} \left\{ (\nabla \mathbf{u}) + (\nabla \mathbf{u})^T \right\} \right] \right). \tag{3.8}$$

In the above expression, the last term in brackets corresponds to the deformation rate tensor $\mathbf{D}$. The viscosity ν_{eff} is in fact the effective viscosity composed of the physical viscosity and a turbulent viscosity. To compute the latter, a k-ω-SST model [101] is used.

3.3.3 Overset technique

The overset dynamic mesh library in OpenFOAM is well suited for scenarios involving large body motions, where mesh deformation may be excessive up to the point of negative volumes, with subsequent numerical instability (Katsidoniotaki and Göteman [74]). The overset method involves defining two independent mesh sets: a relatively large background mesh and a local overset mesh, surrounding the moving body. These two meshes are identified by the assigned value in the *zoneID* field.

The computational domain is created through cell-to-cell mappings between these overlapping and disconnected meshes. While the background mesh remains stationary, in our case the overset mesh moves fixed to the body motion, prescribed in advance using OpenFOAM's motion libraries. Computational cells in the fluid domain are classified into three types: calculated, interpolated, and holes. This classification is taken into account with the field *cellTypes*, where a value of 0, 1, and 2 is given automatically by OpenFOAM, respectively. The incompressible flow governing equations described in Section 3.3.1 are solved for the calculated cells. Interpolated cells facilitate the exchange of flow information between the two mesh regions. The hole cells, representing the moving body in the background mesh, are excluded from the calculations in this mesh.

However, when dealing with moving objects in CFD, due to interpolation between different mesh regions, the Overset mesh technique can be more computationally expensive than the mesh deformation technique (Jung and Kwon [73]). To minimize interpolation error and expedite overset mesh computation, it is advisable to use similar cell sizes for the background and overset meshes near the overset patch (Chen et al. [18]). More details on the overset interpolation schemes adopted for each of the simulated cases to increase computational efficiency with reasonable accuracy are given in Section 3.3.4.1.

3.3.4 Numerical schemes and solver parameters

Numerical schemes face challenges in accurately capturing the thin boundary layers that are created in impulsive start problems, and consequently, it has a strong impact in calculating the drag coefficient (Koumoutsakos and Leonard [77]). The linear equation solvers and numerical discretisation schemes that are selected in this work aim to address these local problems, and, in the following, they are described in detail.

3.3.4.1 Numerical discretization schemes: fvSchemes

In this work, an implicit second-order time scheme was required because of the demand for high temporal accuracy and to enable greater computational efficiency for large time steps. The adopted discretisation for the gradient terms is the standard in finite volume, a second-order Gaussian integration scheme. The advective terms (divergence terms) of the turbulence model fields schemes that are adopted are all based on Gauss integration, with an interpolation scheme that is linear (second order) that is strongly limited towards upwind

for regions of rapidly changing gradients. For the advective flux, instead, a blended scheme is adopted. To account for non-orthogonality correction and to achieve a stable accurate solution, for the surface normal gradient terms (required to evaluate a Laplacian term using Gaussian integration), the limited corrected scheme with a ψ coefficient of 0.5 is adopted. For the diffusion term in the momentum equation (Eq. (3.6)), the Gauss scheme is the only choice of discretisation. As it requires a surface normal gradient scheme, the same limited corrected scheme with a ψ coefficient of 0.5 is adopted.

Regarding the Overset interpolation schemes, by selecting the available interpolation schemes, the one with better results in terms of accuracy at low computational cost is the *inverseDistance* one. Therefore, in this work, this is the selected interpolation scheme used to capture the impulsive start but with lower computational cost, as it is less expensive than other available options (Lemaire et al. [78]).

3.3.4.2 Linear equations solvers: fvSolution

The linear matrices for the fields involved (pressure and velocity) are asymmetric because of the overset interpolation process. Therefore, all asymmetric linear solvers available in OpenFOAM except GAMG are supported. For the transport equations, the smooth solver with symGaussSeidel smoother is adopted, while for the elliptic equations the PBiCGStab solver with DILU preconditioner is used.

To achieve pressure-momentum coupling stability in the transient flow, the pressure field is corrected 3 times and produces a non-diverging accurate solution of the solver. In addition, the PIMPLE loop is activated, and a recalculation of the pressure-momentum coupling is performed 5 times at each time step. To obtain a smooth convergence rate, relaxation factors are applied for fields and equations. Moreover, an additional corrector in the PIMPLE solver is adopted to account for mesh non-orthogonality and large mesh deformation. Lastly, in all simulations, an adaptive time step determined based on a maximum Courant number ranging from 0.7 to 0.9 is used in all simulations.

In order to reduce the computational cost, the turbulence equations are solved only at the end of the PIMPLE loop.

3.4 Test cases description and set-up

3.4.1 Numerical model verification: impulsively started circular cylinder

In this work, an impulsively started circular cylinder is studied as a verification case. The 2-D cases at two different Reynolds numbers of 3000 and 9500 studied in Koumoutsakos and Leonard [77] are used as reference cases. In contrast to the literature case where the circular cylinder is fixed and the fluid moves impulsively, in this study the circular cylinder moves using the overset technique while the fluid moves accordingly. For the movement of the overset

region, the function *tabulated6DoFMotion* from the solver *multiSolidBodyMotionSolver* is used. The moving object is displaced by a distance of $3D$ at a constant velocity of 1 m/s, since a unit diameter of the circular cylinder D is adopted, the kinematic viscosity is varied to achieve the desired Reynolds number. The dimensions and boundaries are shown in Fig. 3.5. To avoid any influence of the boundary conditions on the results, a sufficient distance is adopted from the circular cylinder to the domain limit walls.

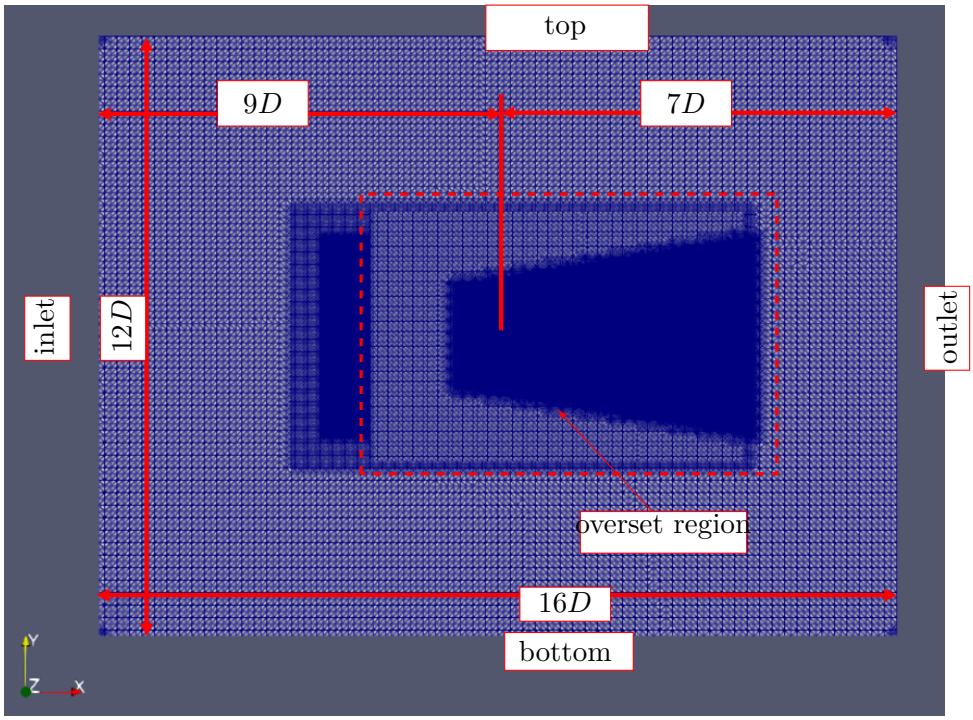

Figure 3.5: Computational domain with labels corresponding to the boundaries.

In Fig. 3.5, the overset zone is labeled and highlighted with the discontinuos red line box. As described in Section 3.3.3, the *zoneID* of this moving part is assigned to 1 (see Fig. 3.6b) using the *topoSet* and *checkMesh* utilities. The *cellTypes* for the walls cells of the moving box are assigned to *interpolated* by the overset boundary condition, and the OpenFOAM solver automatically assigns the type of cells in the proximity of the circular cylinder (see Fig. 3.6a and 3.7).

Fig. 3.7 shows the mesh around the circular cylinder. As can be appreciated, special care is taken to achieve similar mesh size in both the overset mesh and the background mesh. This is done to increase the accuracy of the overset interpolation between the donor and receptor cell points.

The selected boundary conditions (BC) are stated in Table 3.2. The boundary conditions are selected in the inlet and outlet patches to allow the entry and exit of the fluid domain, while the slip conditions are adopted in the top and bottom patches. The overset dynamic mesh technique is employed to manage the motion of the circular cylinder mesh. Consequently, the boundary conditions for the overset patches are managed entirely by OpenFOAM's integrated

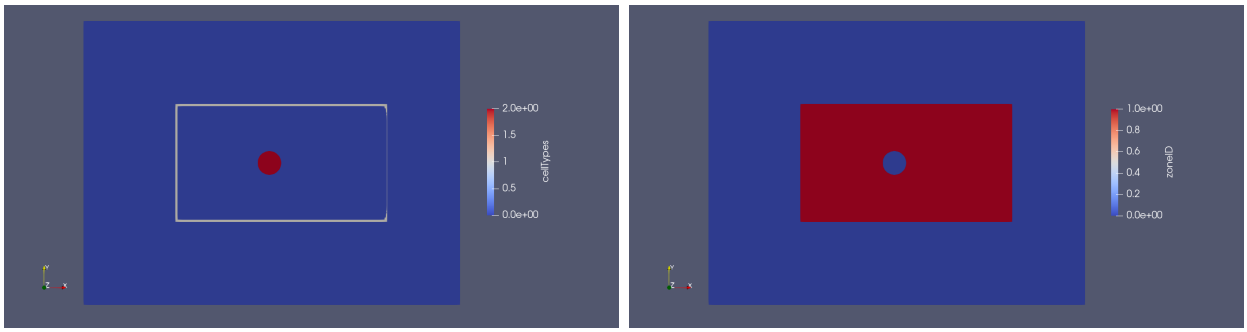

(a) cellTypes (b) zoneID

Figure 3.6: Overset boundary assignment

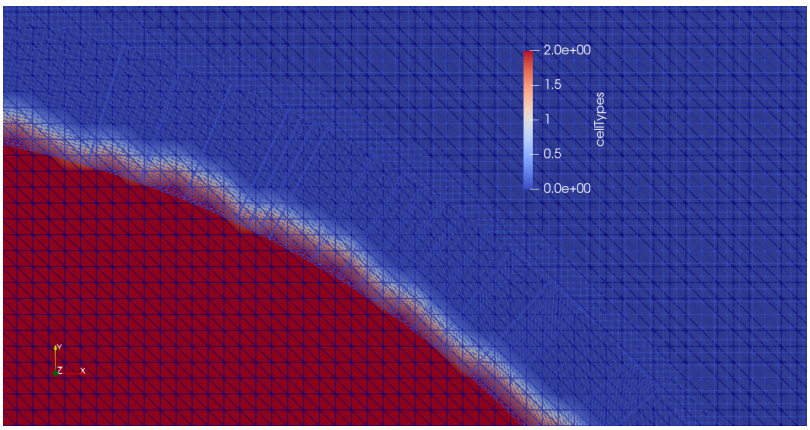

Figure 3.7: Background and overset mesh around the circular cylinder.

overset library. Empty boundary conditions are adopted for the front and back patches to account for the 2-D case setup.

Table 3.2: Boundary conditions used in the verification case.

	Pressure (p)	Velocity (U)	Turbulent kinetic energy (k)	Turbulent viscosity (ν_t)	Turbulence dissipation rate (ω)
inlet	totalPressure	pressureInletOutletVelocity	zeroGradient	calculated	outletInlet
outlet	totalPressure	pressureInletOutletVelocity	zeroGradient	calculated	inletOutlet
bottom	zeroGradient	slip	zeroGradient	calculated	zeroGradient
top	zeroGradient	slip	zeroGradient	calculated	zeroGradient
front	empty	empty	empty	empty	empty
back	empty	empty	empty	empty	empty
cylinder	zeroGradient	movingWallVelocity	kqRWallFunction	nutkWallFunction	omegaWallFunction
overset patches	overset	overset	overset	overset	overset

As introduced in Section 3.3.4, the numerical schemes are carefully selected for the simulations and summarized in Table 3.3. Challenges in accurately capturing the boundary layer at the beginning of the impulsive start and the high temporal accuracy with good computational efficiency are the main motivation behind the schemes selection in this work. In addition, achieving numerical stability was a challenge, especially at the initial time steps because of the impulsive start of the motion. The number of iterations and corrections that are adopted for this case is described in Section 3.3.4.2.

Table 3.3: Numerical schemes used in the verification case.

Time scheme	backward
Gradient scheme	Gauss linear
Divergence scheme	(ϕ, U): Gauss LUST ∇U (ϕ, k): Gauss limitedLinear 1 (ϕ, ω): Gauss limitedLinear 1
Laplacian scheme	Gauss linear corrected 0.5
Overset interpolation	inverseDistance

3.4.2 Numerical model validation: experimental case

The experiments described in Section 3.2 are used as the validation case for the simulations. The computational domain for this case is shown in Fig. 3.8. A sufficient space from the clump weight (of a diameter D, see Table 3.1) to the lateral walls of $12D$ is adopted to avoid any blockage effect. Also, to achieve numerical stability faster, only the parts of the motion law in which the clump weight is moving (see green and yellow boxes in Fig. 3.4) are simulated. Then, the complete motion of the clump weight is around $5.4D$, and to have enough far-field, a distance of $12.5D$ from the clump weight to the closest wall at the beginning and at the end of the motion is adopted. Therefore, the computational domain has a total length of $30.4D$.

In Fig. 3.8, the overset zone is highlighted with a red circle. As described in Section 3.3.3, the zone ID of this moving part is assigned to 1 (see Fig. 3.9a) using the *topoSet* and *checkMesh* utilities. The cellTypes for the walls cells of the moving box are assigned to interpolated by the boundary condition, and the OpenFOAM solver automatically assigns the type of cells in the proximity of the clump weight (see Fig. 3.9b).

The overall quality of the mesh using the utility *snappyHexMesh* is acceptable, achieving a maximum non-ortogonality of 65°. In Fig. 3.10, the different refinement zones are shown. As can be seen, a good refinement was required in the proximity of the clump weight and in the wake zone. It should be noted that, as mentioned in Section 3.3.3, special care was taken to have similar cell sizes in the overset interpolation regions.

In the same fashion as for the verification case, for the motion of the overset region, the function *tabulated6DoFMotion* from the solver *multiSolidBodyMotionSolver* is used. The raw data was not an option due to the major numerical instabilities found at the beginning of the impulsive motion, as a consequence of the noise in the signal of the tracked motions of the clump weight. Instead, the tabulated file that is provided contains the post-processed signal rebuilt with smoothed 6th-order splines.

The boundaries, which are labeled in Fig. 3.8 and the imposed boundary conditions are shown in Table 3.4. As can be seen, they are practically the same as the ones adopted for the verification case (see Table 3.2). Only the front and back patches change, and a slip boundary condition is adopted for these walls.

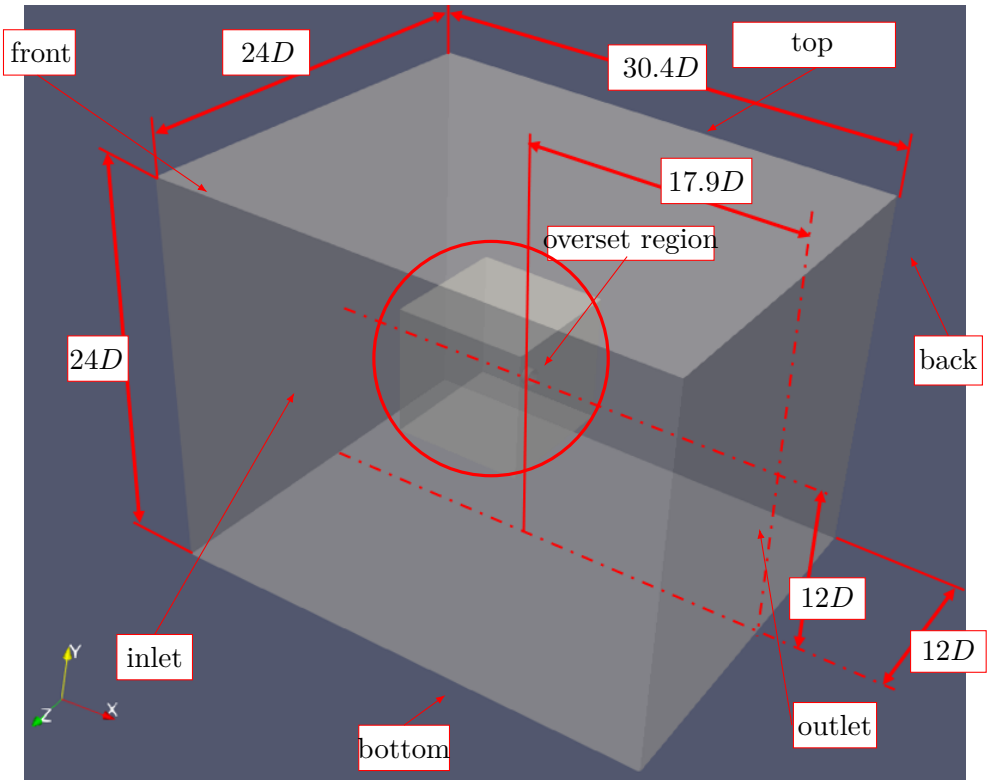

Figure 3.8: Computational domain for the validation case.

Table 3.4: Boundary conditions used in the validation case.

	Pressure (p)	Velocity (U)	Turbulent kinetic energy (k)	Turbulent viscosity (ν_t)	Turbulence dissipation rate (ω)
inlet	uniformTotalPressure	pressureInletOutletVelocity	zeroGradient	calculated	outletInlet
outlet	uniformTotalPressure	pressureInletOutletVelocity	zeroGradient	calculated	inletOutlet
ground	zeroGradient	slip	zeroGradient	calculated	zeroGradient
atmosphere	zeroGradient	slip	zeroGradient	calculated	zeroGradient
front	zeroGradient	slip	zeroGradient	calculated	zeroGradient
back	zeroGradient	slip	zeroGradient	calculated	zeroGradient
clump weight	zeroGradient	movingWallVelocity	kqRWallFunction	nutkWallFunction	omegaWallFunction
overset patches	overset	overset	overset	overset	overset

The numerical schemes provided in *fvSchemes* are shown in Table 3.5. As highlighted in Section 3.3.4.1, a second-order time scheme is used due to the highly unsteady flow past of the impulsively started clump weight. Therefore, for the overset interpolation as mentioned in Section 3.3.4.1, the *inverseDistance* method is selected because of its accuracy at the expense of its computational cost, as it is more expensive than other available options.

To obtain the solution, the numerical solver parameters that are adopted are already described in Section 3.3.4.2.

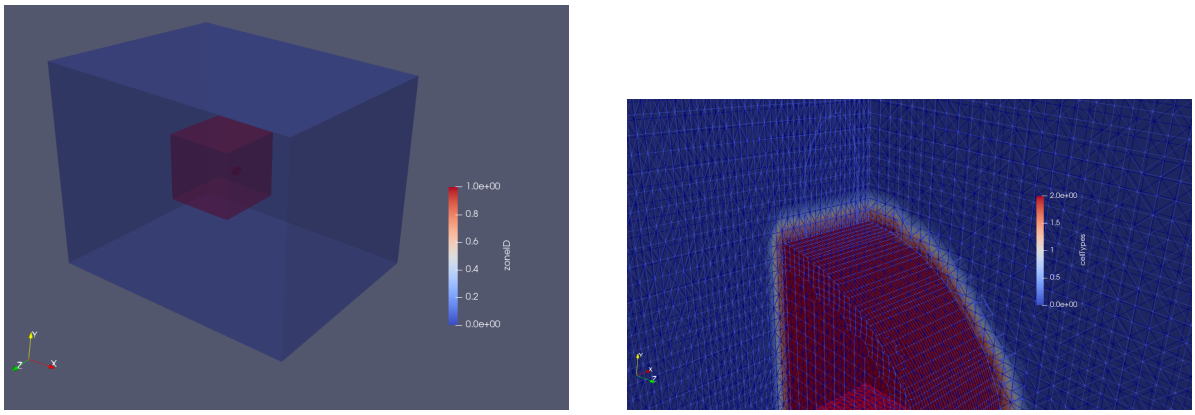

(a) Assigned zoneID for the computational domain.

(b) Detailed view of the assigned cellTypes in the proximity of the clump weight.

Figure 3.9: zoneID and cellTypes assigned for the overset dynamic mesh.

Table 3.5: Numerical schemes used in the validation case.

Time scheme	CrankNicolson 0.9
Gradient scheme	Gauss linear
Divergence scheme	(ϕ, u): Gauss limitedLinearV 1 (ϕ, k): Gauss limitedLinear 1 (ϕ, ω): Gauss limitedLinear 1
Laplacian scheme	Gauss linear corrected
Overset interpolation	inverseDistance

3.5 Results

In this section, the simulation results of the early stages of the flow past an impulsively started circular cylinder and a disk are presented. As highlighted in section 3.3, the overset interpolation is computational demanding; despite the numerical schemes and linear equation solvers selected in the numerical model to address an optimal computational cost with reasonable accuracy, peaks in the pressure field are found as a consequence of the overset interpolation. Therefore, to cancel this noise and enhance clarity for the reader, in this section, only the post-processed signals after a filtering process are shown. A 30th-order median filter is applied to smooth the signal output of the OpenFOAM simulations with overset. Fig. 3.11 shows an example of the post-processing that is applied to the results.

The convergence of the numerical method is showed only for the highest Reynolds number of the verification cases.

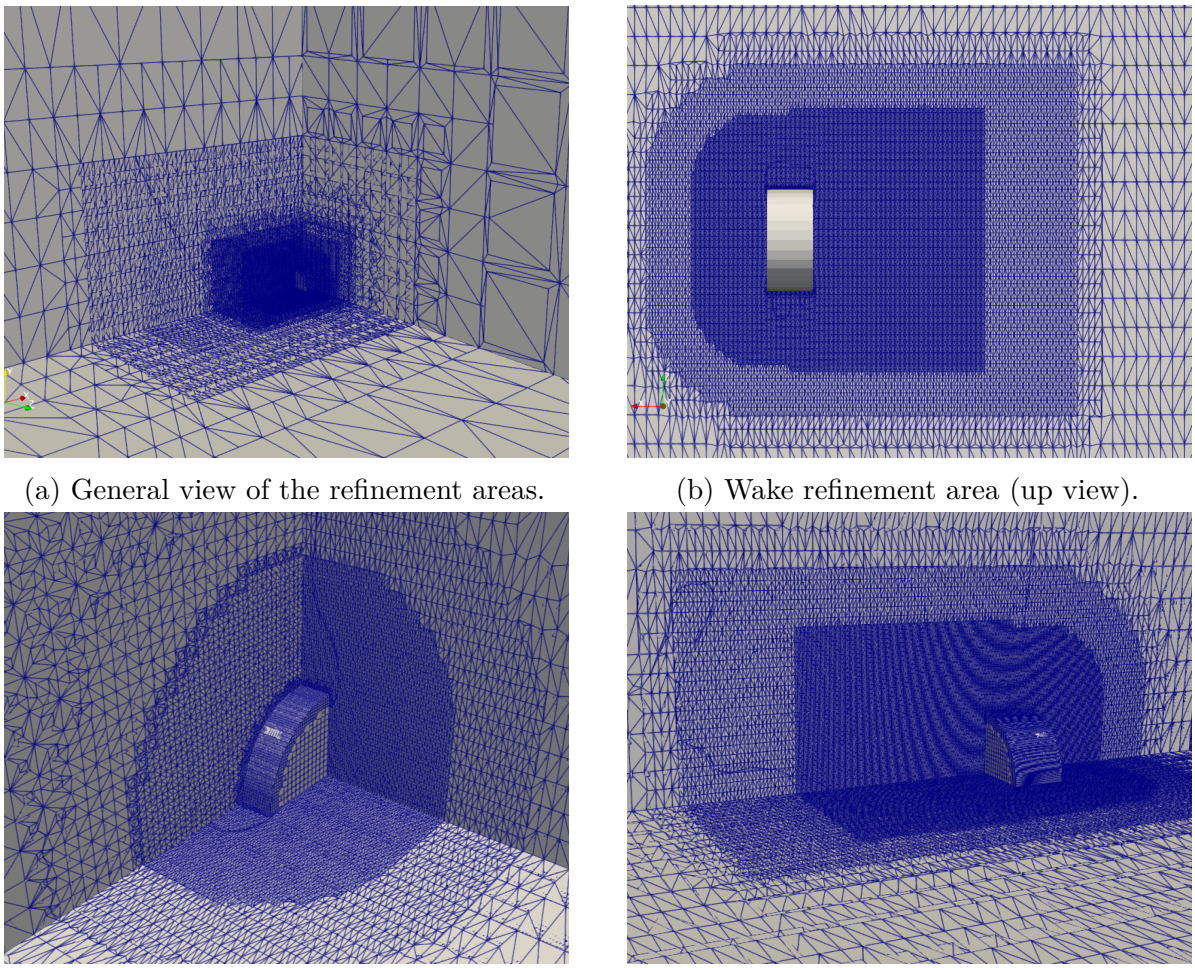

(a) General view of the refinement areas.

(b) Wake refinement area (up view).

(c) Clump weight refinement (front).

(d) Clump weight refinement (back).

Figure 3.10: Detailed view of the different refinement areas.

3.5.1 Unsteady flow past a impulsively started circular cylinder

The results presented in this section correspond to the case described in Section 3.4.1. In the following, the two Reynolds numbers tested are presented. It should be noted that, as highlighted in Section 3.4.1, a different technique is adopted in which the circular cylinder moves within the fluid domain.

The results presented in this section are verified with different simulation results available in the literature, Koumoutsakos and Leonard [77] and Rossi et al. [122]. We should take into account that the objective of these verifications is just a test for the overset technique as none of these results are validated experimentally, being these flows intrinsically 3D for these Reynolds numbers.

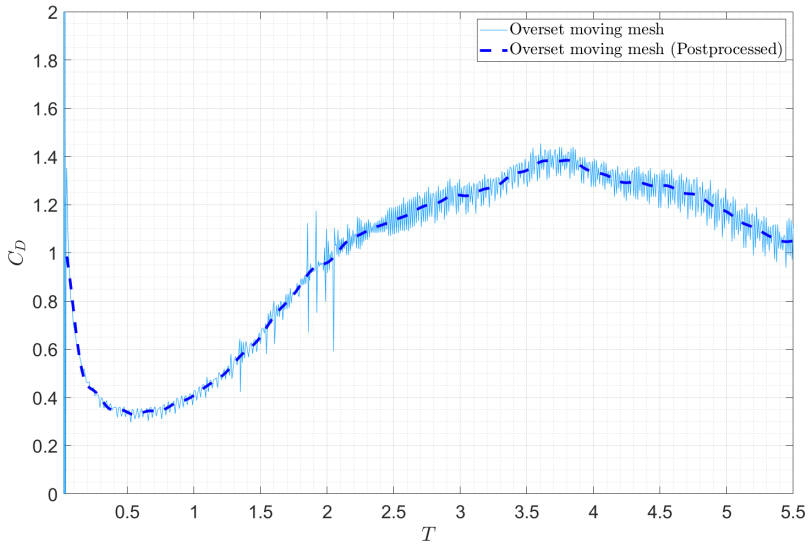

Figure 3.11: Result of the moving average mean postprocessing applied for de overset results (C_D comparison).

3.5.1.1 Re = 3000

As the Reynolds number is moderate and laminar and turbulent flow can be found in the simulation (Zdravkovich [145]), both a RANS and a DNS approach are considered.

Fig. 3.12 shows the comparison for the drag coefficient of an impulsively started circular cylinder at Re = 3000 with the work of Koumoutsakos and Leonard [77]. The time is expressed in non-dimensional form as $T = tU/R$ (being U the free-stream velocity and R the radius of the circular cylinder).

For the sake of completeness, in Fig. 3.12 the curves with the turbulence model are compared when the circular cylinder with and without moving the overset region. The monotonic increase of the drag coefficient and, in particular, a flat region of the drag coefficient ($2.5 < T < 3.0$) due to the separation phenomenon is reasonably well captured in all simulations. However, the results are improved when no turbulence model is used (orange curve). Similarly to Koumoutsakos and Leonard [77], the DNS approach is able to capture all complex vortical structures formed in the vicinity of the shear layers without any turbulence modeling.

3.5.1.2 Re = 9500

To further study the initial stages of the flow past the circular cylinder with an impulsive start, the Re = 9500 is also studied since it is closer to the reference Reynolds number of the validation case (around 3×10^4, see Section 3.2). At this higher Reynolds number, laminar to turbulent transition flow is also found in shear layers, and again both a RANS and a DNS approach are also considered.

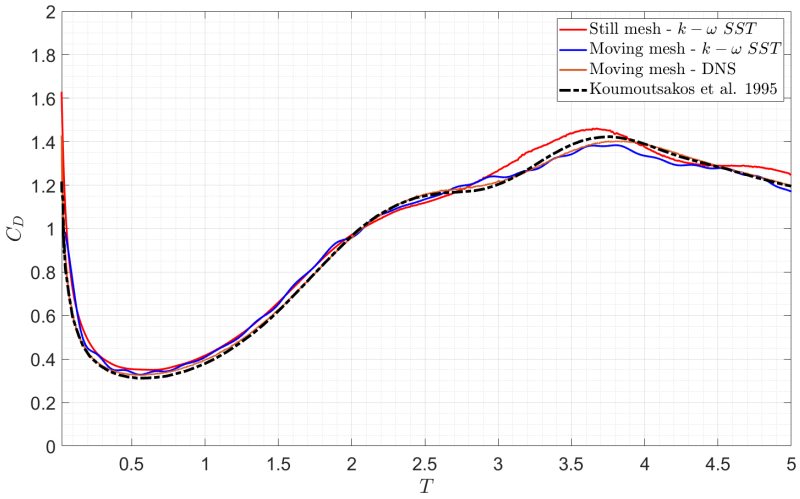

Figure 3.12: C_D comparison for different dynamic meshes and turbulence model of an impulsively started circular cylinder at Re = 3000.

Fig. 3.13 shows the instantaneous streamlines at non-dimensional time $T = 2$ presented in the different numerical works in the literature and in experiments. In addition, to further understand the mechanisms by which the vorticity near the circular cylinder affects the drag coefficient of the body, Fig. 3.14 shows the vorticity field at three non-dimensional times T. As shown in both figures, a good comparison is achieved in the present simulations; the vortices separation occurring from very early stages is accurately captured with our numerical solution.

To understand the variation of the drag coefficient in the initial stages of an impulsively started circular cylinder, it is necessary to understand the dissipation mechanisms described in Koumoutsakos and Leonard [77]: The initial layer of vorticity around the circular cylinder (see Fig. 3.14b) continues to grow until the formation of a secondary vortex (which can be seen in Fig. 3.13) induces the eventual detachment of the primary vortex from the circular cylinder. This detachment severs the strength of the secondary vortex, reducing the drag coefficient. By $T = 3$ it can be seen in Fig. 3.14d how the primary vortex has already reached the outer flow and the secondary vortex is also detaching. This process continues to evolve, and more eddies of smaller scales are formed and detached from the boundary layer. See, for example, in Fig. 3.14f how the two mentioned eddies have already reached the outer flow.

Fig. 3.15 shows the comparison of the drag coefficient, using laminar and turbulent approaches, with the works in the literature. The comparison seems reasonably good, with the DNS clearly better than the RANS result. The discussed interaction of the vorticity in the vicinity of the boundary, the reason behind the reduction and increase in drag coefficient (Koumoutsakos and Leonard [77]), is captured in the simulations. Since the mesh used in the simulations is the same, the differences between both approaches show that the averaging process of the RANS formulation does not capture the physical dynamics of the vortical structures in the same way as the DNS approach.

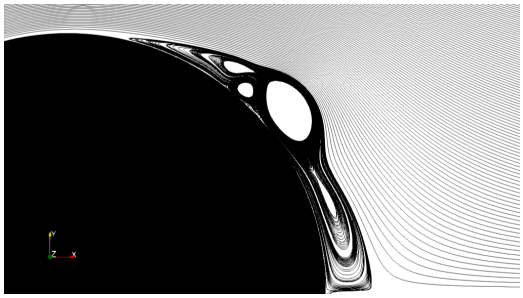

(a)

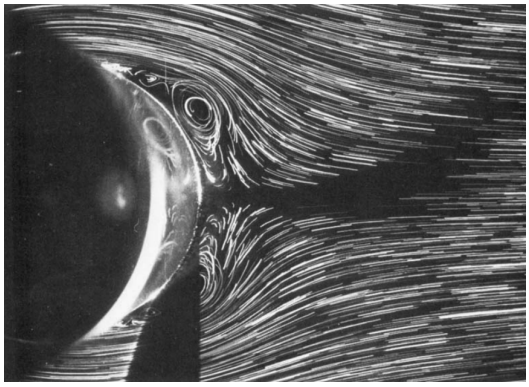

(b)

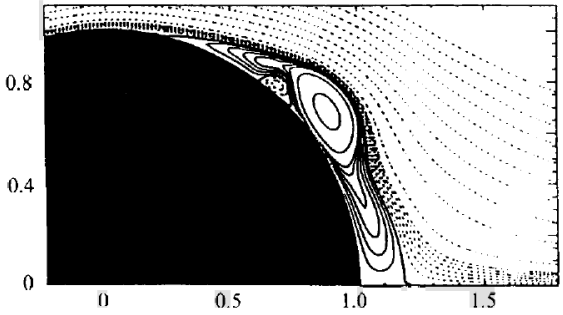

(c)

Figure 3.13: (a) Instantaneous streamlines from present work, (b) Experiments from Bouard and Coutanceau [8], and (c) Instantaneous streamlines from [77], of an impulsively started circular cylinder for Re = 9500 at $T = 2.0$.

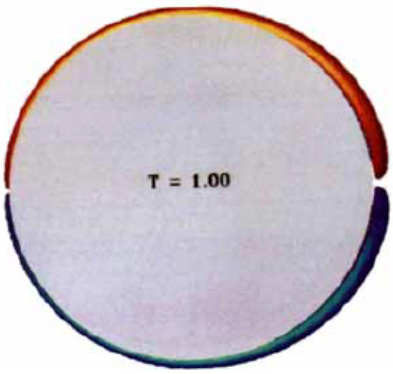

(a) Koumoutsakos and Leonard [77].

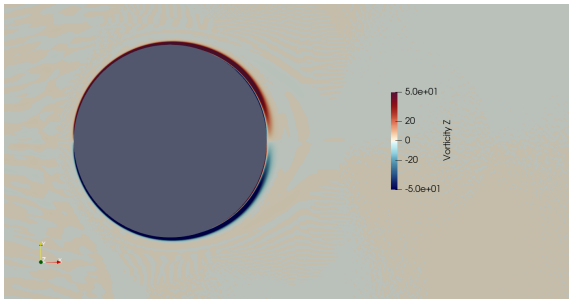

(b) Present work.

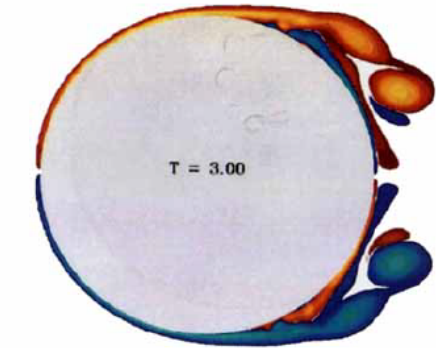

(c) Koumoutsakos and Leonard [77].

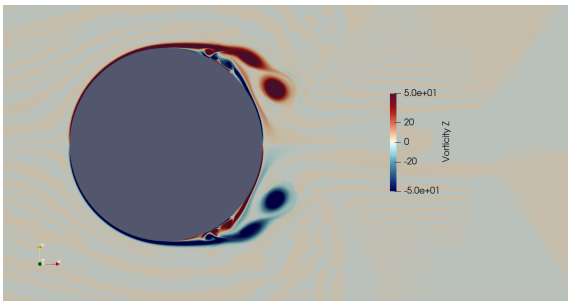

(d) Present work.

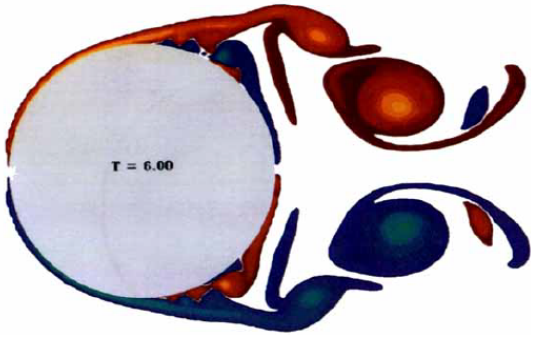

(e) Koumoutsakos and Leonard [77].

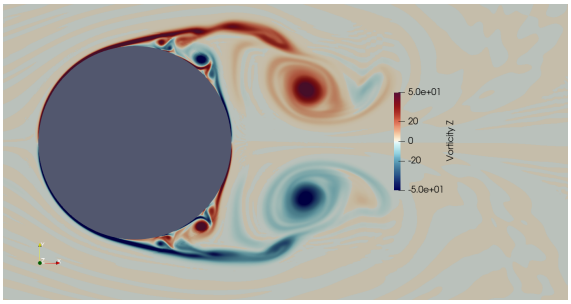

(f) Present work.

Figure 3.14: Vorticity field of an impulsively started circular cylinder at adimensionalized time $T = 1$, $T = 3$, and $T = 6$ (Re = 9500).

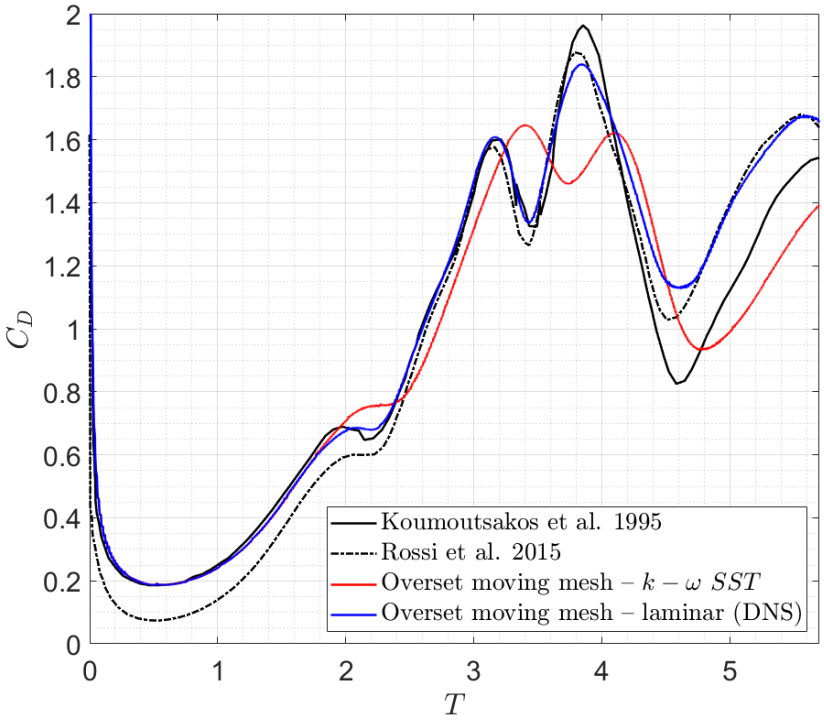

Figure 3.15: C_D comparison for different turbulence modeling.

The differences found in the RANS simulations with the literature do not seem to be induced by the lack mesh of resolution in such a time dependant problem. The mesh convergence was performed for five grid levels, increasing the number of elements, especially around the circular cylinder. To understand how the turbulence model impact in the results, the same convergence analysis is carried out for the laminar cases simulating the same meshes. Fig. 3.16 shows the convergence analysis for the two approaches. The refinement consisted of reducing the size of the first cell in the direction of the flow (x-axis) while maintaining the y^+ constant for all the simulations. Therefore, the thickness of the boundary layer is kept constant, and the number of layers varies for each grid level. This is the explanation why the difference in the results from the coarse meshes to the finer ones is so notorious.

After reaching a convergence, with the turbulence model, although the physics involved seemed to be partly captured, phase shift and magnitude discrepancies are still found. The higher Reynolds number for this case than for the previous case (Re = 3000) may penalize the results and is attributed to the fact that the numerical scheme proposed by the RANS formulation does not capture the intrinsic time scales of the vortices.

When simulating the DNS case, it is observed in Fig. 3.15 how the comparison improves considerably, smaller magnitude differences are found, and the phase shift is almost eliminated. This is expected since both of the literature results that are compared do not model the turbulence with a RANS formulation. However, even though the mesh is in the range of the reference cases, an exact match to the results from the literature is not achieved. Up to $T = 3.5$ the numerical results are close to the vortex method [77], but from the remaining

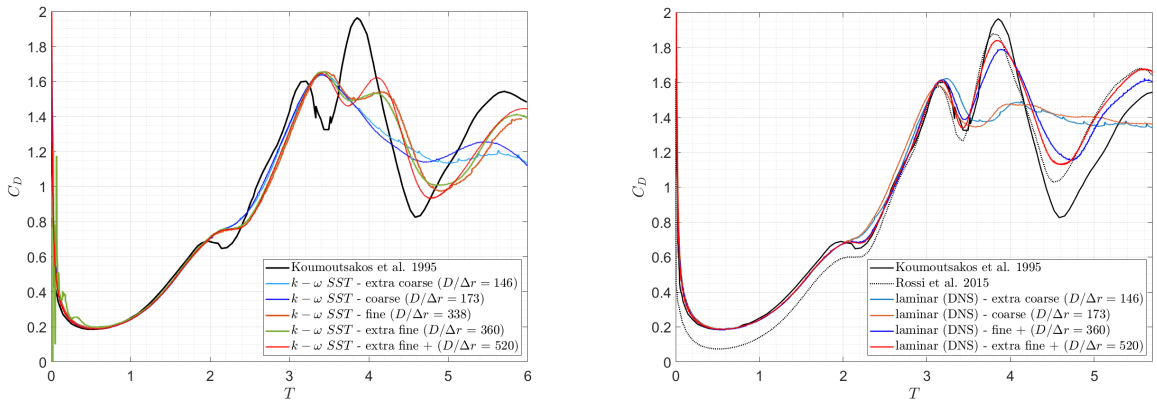

(a) $k-\omega$ SST. (b) DNS.

Figure 3.16: Mesh convergence for the verification case (Re = 9500) for different turbulence modeling.

time $3.5 < T < 6$ our solution is closer to the SPH formulation [122]. However, it should be remarked that the curves associated with the drag coefficient were used as reference values for verification purposes, and they do not have any experimental validation.

3.5.2 Numerical validation with experiments

In this section, the results of the experimental campaign described in Section 3.2 are compared with the computational results. As discussed in Section 3.2, only the red and yellow parts of the motion law are simulated (see Fig. 3.4). Because this is a 3-D case, to solve the Kolmogorov scale and be able to capture the smaller eddies, a number of $27Re^{(9/4)}$ cells would be necessary. Due to the high Reynolds number (maximum of 3×10^4) the computational resources that are required are too demanding and certainly out of the scope of this engineering problem. Therefore, the DNS approach is not followed in this section, and only the results with a turbulence model are shown.

3.5.2.1 Hydrodynamic force

For the first approach of the problem, instead of using the experimental motion law (see Fig. 3.4), the objective nominal scaled acceleration a of 0.033 m/s^2 indicated in Section 3.2 is used for the clump weight motion law. Since the shape of the clump weight is a circular disk, the total hydrodynamic force F_H can be modeled with the following equation:

$$\mathbf{F_H} = \mathbf{F_D} + m_A\ddot{\mathbf{x}} = \frac{1}{2}\rho C_D \pi D^2 \dot{\mathbf{x}}^2 + m_A\ddot{\mathbf{x}} \ , \tag{3.9}$$

where C_D is the drag coefficient of a disk as a function of the Reynolds number (see White [138]), D is the diameter of the disk, and m_A is the added mass.

Fig. 3.17 shows the comparison of the empirical approach and the OpenFOAM simulations for this case, in which a motion law with constant acceleration is used. As shown, a fair comparison is achieved between the two approaches. Discrepancies around the simulated time $t = 6s$ can be appreciated, but in general acceptable results can be achieved at a computational cost insignificant with this quasi-static empirical model.

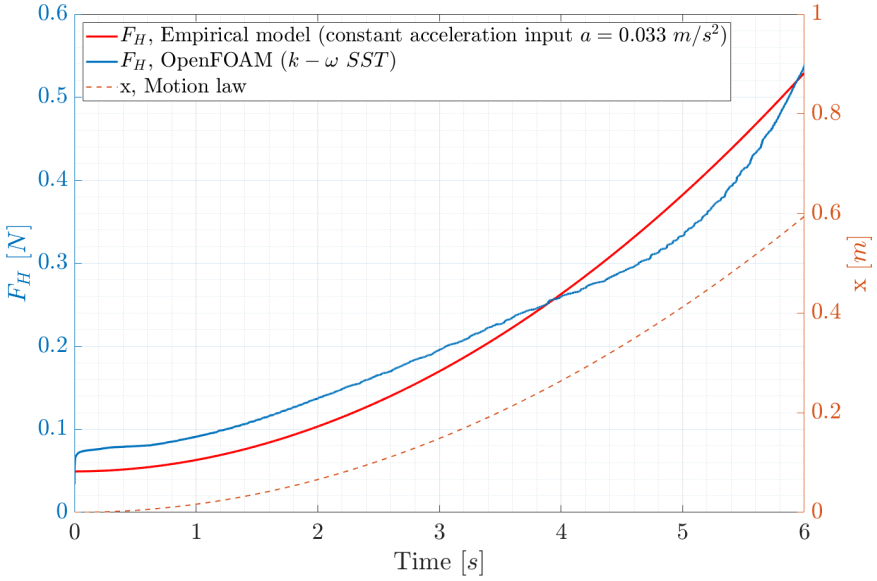

Figure 3.17: Numerical comparison of the CFD results and the quasi-static empirical model approximation.

Based on the free body diagram of the experiments (see Fig. 3.2), the hydrodynamic force obtained from OpenFOAM needs to be processed to obtain the tension in the line that pulls the clump weight ($\mathbf{T}$). Then, to compare with the load cell from the experiments, the following equation, derived from Eq. (3.1), is used:

$$\mathbf{T} = \mathbf{F_H} + m\mathbf{g} - \mathbf{E} + m\ddot{\mathbf{x}} \ , \tag{3.10}$$

where the tension of the wire $\mathbf{T}$ is the one measured with the load cell, $\mathbf{F_H}$ is the hydrodynamic force from OpenFOAM, m is the mass of the scaled clump weight, g is the acceleration of gravity, $\mathbf{E}$ is the buoyancy of the scaled clump weight, and $\ddot{\mathbf{x}}$ is the acceleration that is obtained from a double derivation of the experimental instantaneous position of the clump weight (which is measured with the OptiTRACK cameras and markers, see Fig. 3.18). Note that this instantaneous position is post-processed before applying as an input motion law to the clump weight in OpenFOAM as already described in Section 3.4.2.

Fig. 3.19 shows the numerical and experimental comparison of the force (in the motion direction). For the sake of clarity in the figure, only the post-processed results, both from the OpenFOAM (CFD) and the experiments (EFD), are shown (left axis). Additionally, in the same axis, the quasi-static empirical approach using the instantaneous values of velocity and

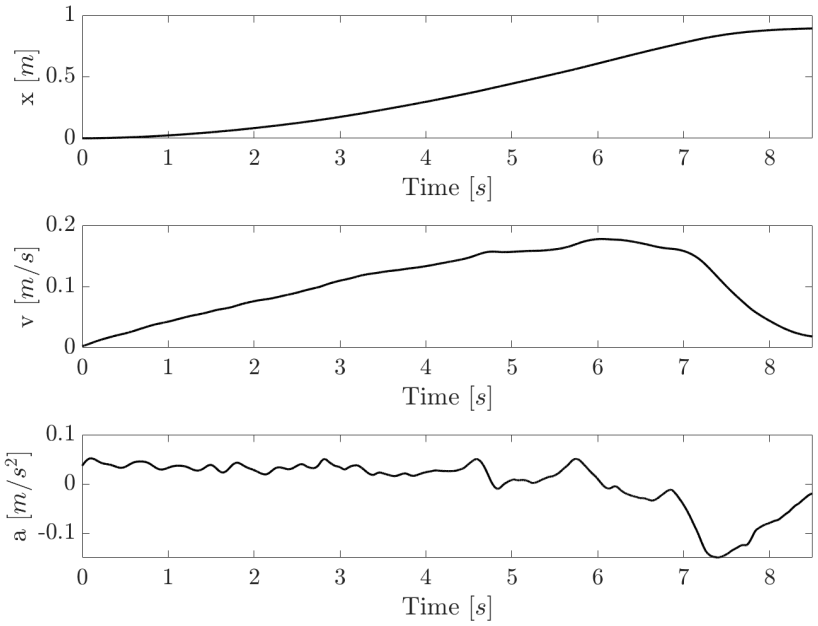

Figure 3.18: Post-processed instantaneous position x of the clump weight (top), the derived velocity v (middle), and acceleration a (bottom).

acceleration is also shown. To clearly identify the stages of the motion law, the instantaneous acceleration of the clump weight is also plotted (right axis).

In general, the maximum error in magnitude of the CFD predictions along the experimental curve is around 5%. The error margin increases when the acceleration is impulsively changed.

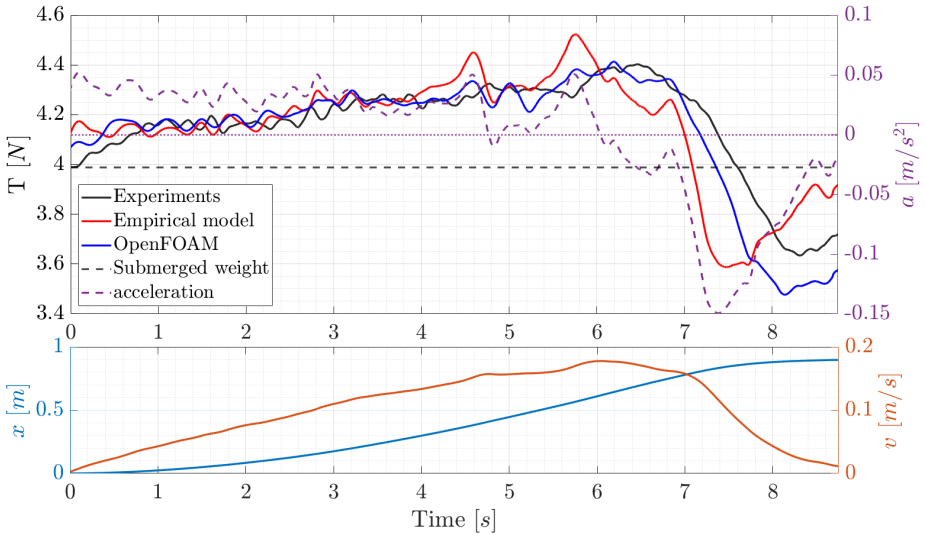

Figure 3.19: Experimental force (EFD) and numerical force (CFD) comparison.

Therefore, as expected, the initial instants (from 0 to 1 s) and the deceleration instants (from 7 to 8.75 s) of the motion, where inertia plays an important role, are the periods of time with the largest differences. Also, differences of the signals can be attributed to the fact that in the experiments the motion is not purely in one direction. Instead, flow instabilities induce lateral motions that can be captured by the load cell.

The oscillations that are seen are clearly induced by the instantaneous acceleration of the clump weight (see the purple curve in Fig. 3.19). The numerical and experimental curves capture these oscillations reasonably well in terms of frequency.

Since acceleration and inertia are strong components in the force of this motion, it can be clearly seen that the predictions of the quasi-static empirical model do not accurately approximate the experiments. It seems that the transient behavior present at the initial and deceleration stages of the impulsive motion is not captured well enough. An important delay of around 1 s in the minimum force peak is shown around 8 s. This time shift is not evidenced in the CFD results. However, in the stages of the motion where the acceleration remains more constant (1 to 5 s), smaller differences are found. We can conclude then that more development of the quasi-static empirical model is necessary if transient effects need to be considered; but, if only a steady state wants to be considered, the forces involved in the motion of the clump weight can be reasonably well captured with the simplified empirical model (C_D and m_A both remain close to 1 during all the motion).

3.5.2.2 Flow description and features

To understand the evolution of the flow past an impulsively started scaled clump weight, some flow features and fields are described. The total simulation time is divided into two major stages: the acceleration stage (green part of Fig. 3.4, 0 to 6s) and the deceleration stage (yellow part of Fig. 3.4, from 6 to 8.75s). During this time, the clump weight moves a distance of almost 1 m, which means about 5.5 times its diameter.

Fig. 3.20 includes different snapshots of the pressure field around the scaled clump weight in the acceleration stage. All figures are generated every second of the simulated time.

In Fig. 3.20 it is clearly observed how symmetric the flow around the clump weight is in all the evaluated instants. As the velocity increases due to the acceleration, the pressure in front of the clump weight grows, producing the hydrodynamic force to increase in the upper surface. As the flow evolves further, this trend continues, as expected from the results of the force illustrated in Fig. 3.19.

To see the 3-D vortical structures, the Q-criterion isosurfaces are included in Fig. 3.21. As shown, the vortex structures formed around the clump weight are asymmetric and can induce the intrinsic instabilities of the flow. They can be a source of contribution to the tension oscillations in Fig. 3.19, but, since the quasi-static empirical model also shows them, it is concluded that the contributions of these instabilities are smaller compared with the contribution of fluid inertia due to changes in acceleration.

Fig. 3.22 includes different snapshots of the pressure field around the scaled clump weight

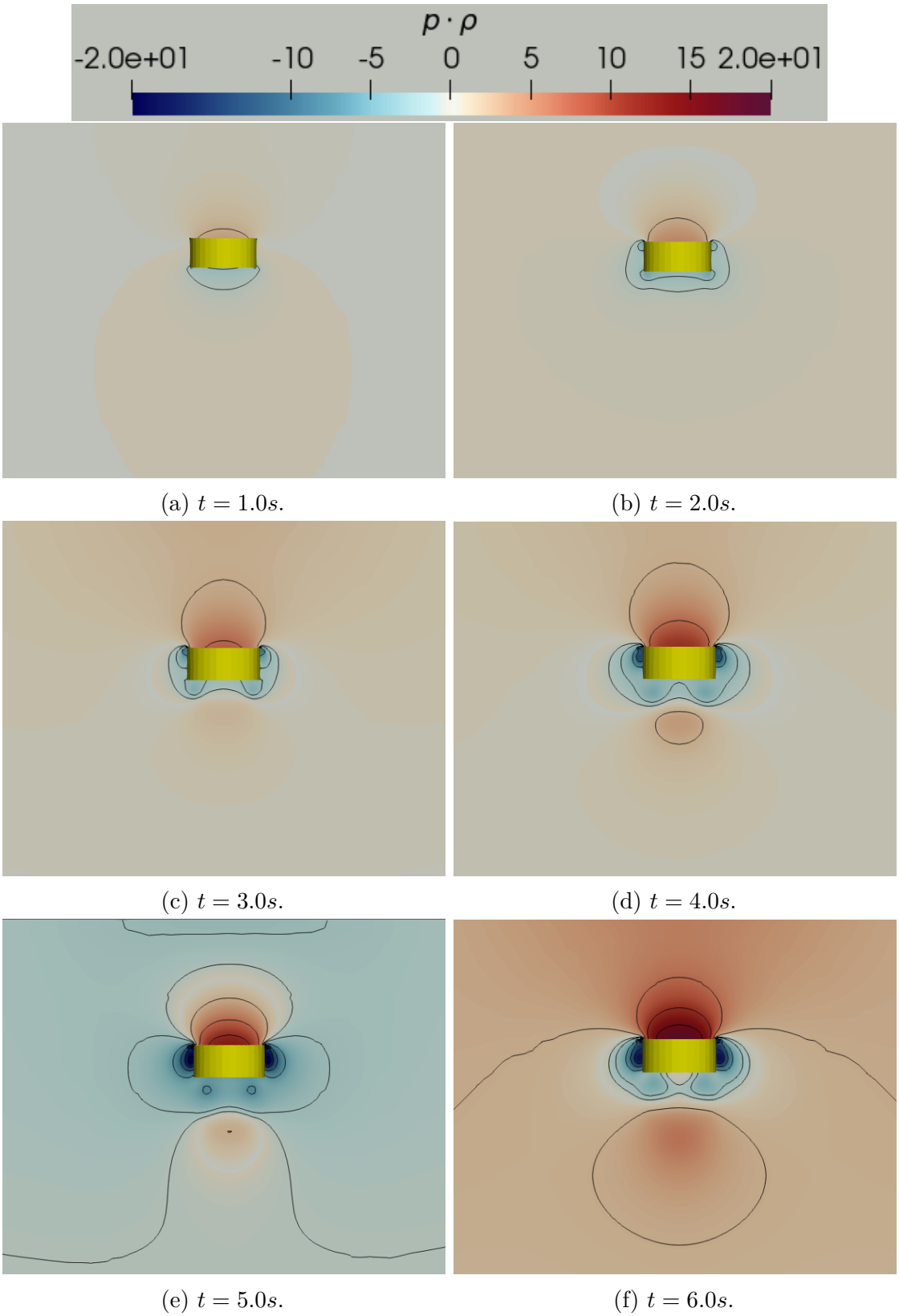

(a) $t = 1.0s$.

(b) $t = 2.0s$.

(c) $t = 3.0s$.

(d) $t = 4.0s$.

(e) $t = 5.0s$.

(f) $t = 6.0s$.

Figure 3.20: Pressure field of the flow around the impulsively started clump weight at times $t = 1.0s$, $t = 2.0s$, $t = 3.0s$, $t = 4.0s$, $t = 5.0s$, and $t = 6.0s$. The motion is in the upward direction.

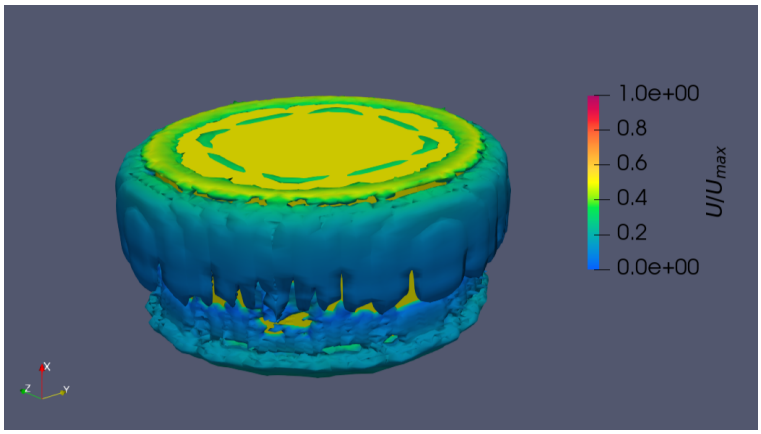

Figure 3.21: Q-criterion isosurfaces. $Q = 1$ at $t = 2.0s$.

at the deceleration stage. All figures are generated every 0.5 s of the simulated time. As can be seen, the velocity reduction produces the detachment of the main vortex that was growing in the acceleration stage but in the opposite direction, in the same direction as the motion of the clump weight product of the fluid inertia. This fluid inertia is the cause that reduces the hydrodynamic force substantially. When the vortex has passed, the inertial effects slowly disappear until the recovery of the initial value of tension (submerged weight). As was mentioned in the previous section, this particular phenomenon is not properly captured in the quasi-static empirical model since the theoretical added mass might be overestimated. However, in the CFD it is well matched, and the contribution of this acceleration seems to be captured, although with a small difference in magnitude.

3.6 Computational resources

All simulations presented in this work have been performed on the Magerit Supercomputer, using OpenMPI parallel programming for 48 processors and 100GB of memory. As mentioned in section 3.3.4.2, the advantages of the overset interpolation in terms of large mesh deformation come with an elevated computational cost; the solver requirements for the cases are quite demanding, requiring at least 5 pimple loop iterations. The computing time for the simulations described in 3.5.2 was around 72 hours for the simulated time of 8.75 s, the most demanding in terms of computational resources.

Table 3.6 includes a summary of the computational resources used in all the simulations carried out in this work.

As can be concluded from this section, having an exact matching of the results is too computationally expensive when using the overset technique. Therefore, when the interest lies in capturing the physics involved in the impulsive start of a body rather than in instantaneous values, reasonable engineering results can be obtained by modeling the turbulence and assuming a number of cells limitations.

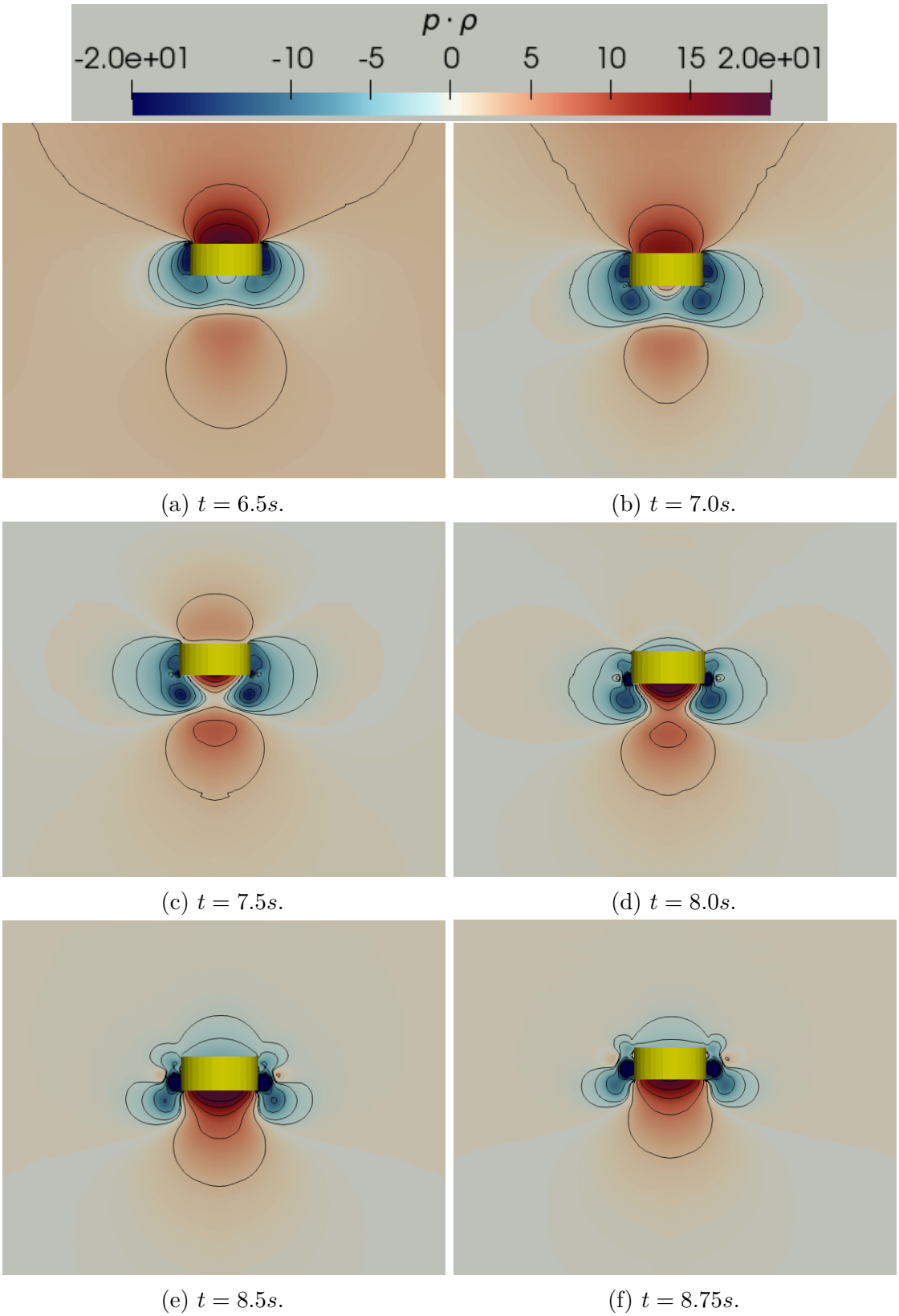

(a) $t = 6.5s$.

(b) $t = 7.0s$.

(c) $t = 7.5s$.

(d) $t = 8.0s$.

(e) $t = 8.5s$.

(f) $t = 8.75s$.

Figure 3.22: Pressure field of the flow around the impulsively started clump weight at times $t = 6.5s$, $t = 7.0s$, $t = 7.5s$, $t = 8.0s$, $t = 8.5s$, and $t = 8.75s$. The motion is in the upward direction.

Table 3.6: pimpleDyMFoam solver CPU time costs and parameters for the simulated cases. The diameter D is taken as the characteristic length for all the cases.

	Flow around circular cylinder (Re=3000)	Flow around circular cylinder (Re=9500)	Experimental case (Re=$9500_{MAX} = 3 \times 10^4$)
$D/\Delta r$	20	360	132
y^+	1	1	1
N cells	$0.6M$	$1.1M$	$4.5M$
simulated time	$6s$	$6s$	$8.75s$
$dt_{initial}$	$0.07s$	2e-3s	2e-5s
CPU time	37 *hours*	48 *hours*	90 *hours*

3.7 Concluding remarks

In this chapter, the hydrodynamics of clump weights when subjected to impulsive starts are investigated. The methodology adopted during this chapter is to approach the problem from three different perspectives, using computational fluid dynamics (CFD) simulations, empirical modeling, and experiments.

The use of overset mesh techniques in OpenFOAM proved effective in simulating the complex flow dynamics associated with impulsive starts, despite computational challenges. The numerical results are verified against the literature data for impulsively started cylinders at Reynolds numbers of 3000 and 9500, and validated with the experimental data obtained from tests conducted in the towing tank at CEHINAV.

The CFD simulations captured the intricate vortical structures and the transient behavior of the flow, showing good agreement with the experimental measurements. The empirical model provided a reasonable approximation of the hydrodynamic forces, especially under steady-state conditions, although it was less accurate during transient phases, where fluid inertia played a significant role.

The findings of this chapter suggest that for practical engineering applications, a combined approach of CFD and simplified empirical models can be used to estimate hydrodynamic forces on clump weights with acceptable accuracy. This has implications for modeling hydrodynamic forces of the clump weight in other simulation software, such as mooring line dynamics codes, maintaining result fidelity.

Future work should focus on refining the empirical model to better capture transient effects and further optimizing the computational efficiency of overset mesh simulations for large-scale problems. Additionally, extending the validation to higher Reynolds numbers and more complex flow conditions will enhance the robustness and applicability of the proposed methodologies. Including the real motions in the 6 DOF the clump weight that can be subjected product of the line motions, to understand the hydrodynamic forces involved in other directions (like transverse, predominant in viscous drag of a mooring line) can be a valuable future prospect for exploration.

Chapter 4

Inclusion of clump weights on isolated catenary mooring lines

4.1 Abstract

In this chapter, the focus is on the isolated mooring dynamics with a prescribed motion for the fairlead. The influence of clump weights when added to a mooring line is studied from a dual point of view: experimentally, using forced oscillations scaled experiments in a towing tank, and numerically, using a finite element numerical tool where the dynamics of the clump weights has been modeled.

For the numerical computation of the mooring line, the OPASS dynamic code based on the finite element method is used. This code was successfully validated for an isolated line in Azcona et al. [2], but a new implementation in the code is proposed to include the dynamic effects of clump weights on the line. The numerical tool with the new implementations is successfully validated against experiments and verified with MoorDyn, a well-known commercial open-source code for the dynamics of the mooring line from NREL.

Since both simulation codes are based on a lumped mass formulation, the comparison is logical. MoorDyn is a simple, efficient, and versatile mooring system dynamics model designed to work coupled with other simulation tools such as OpenFAST [110]. MoorDyn is based on a lumped mass formulation of a mooring line's dynamics, to enable simulation of a wide variety of mooring and cabling arrangements. It has already been successfully validated with experiments in Hall and Goupee [49] coupled with OpenFAST, but to the author's knowledge, it has not been validated standalone to date.

The experiments include different configurations of clump weights to assess their influence on the system's dynamics and serve as validations for the numerical tools. These configurations included different weight locations and adjustment of the fairlead pretension.

This chapter contributes to understanding the dynamics of the mooring line, focusing on the effects of clump weights when added to the isolated line. The accuracy of the numerical simulations is analyzed and compared, particularly in how these devices are modeled in both

numerical tools. Most of the findings and conclusions of this chapter have already been published in Lopez-Olocco et al. [89].

4.2 Experiments description

In Chapter 1 the semi-submersible platform type is highlighted as one of the most promising FWT floating substructures due to its numerous advantages. Therefore, for the experimental validation of the implementations in OPASS, the reference mooring system of the OC4-DeepCWind FWT has been selected. Fig. 4.1 shows the OC4-DeepCWind FWT mooring system.

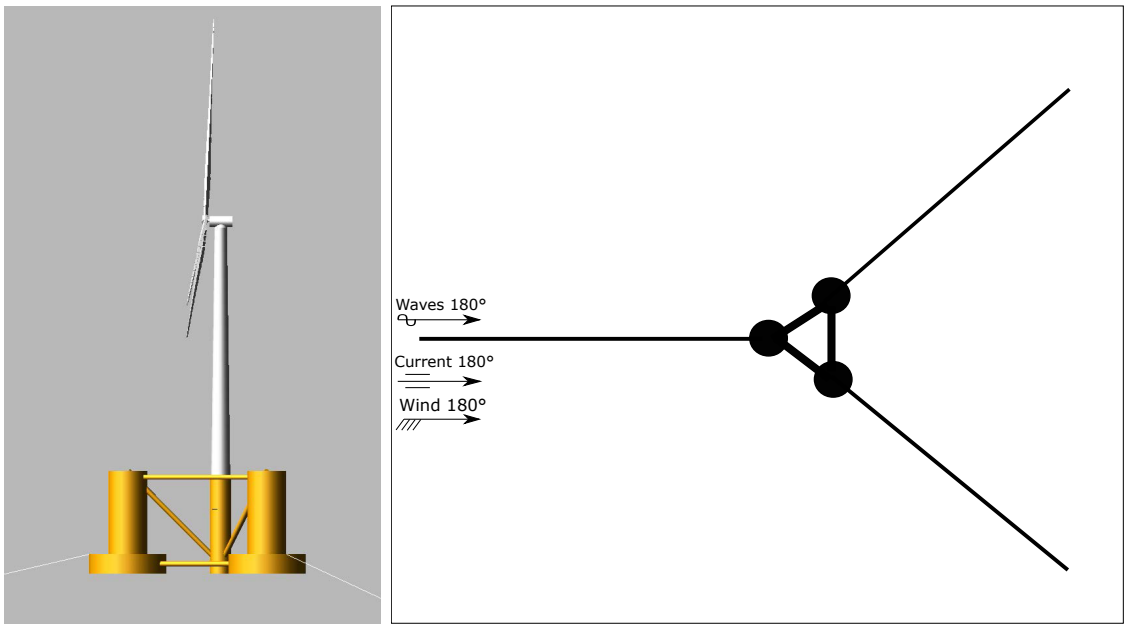

Figure 4.1: (**Left**) OC4-DeepCWind FOWT design. (**Right**) Top view of the mooring system of the OC4-DeepCWind FWT [121].

Considering the worst case scenario where waves and wind are aligned in the 180 *deg* direction as shown in the right panel of Fig. 4.1. This situation in which the environmental conditions align with the upwind mooring line causes it to become the most loaded one. It is well known that in this scenario, the surge motions of the moored platform will become very important, and therefore need to be analyzed (see Huse [56]).

The experimental campaign was carried out in the calm water tank in *Canal de Ensayos Hidrodinámicos de el Pardo* (CEHIPAR), see Fig. 4.2a. The main dimensions of the tank are 320 m in length, 12.5 m in width, and water depth is kept at 6.5 m. The tank is equipped with a towing carriage, which supports all the necessary equipment for the tests (see Fig. 4.2b).

The experiments consist of the excitation of the Fairlead with horizontal periodic movements reproducing the platform surge motion. Depending on the installation site, when surge motion

(a) (b)

Figure 4.2: CEHIPAR facilities. (**a**) CEHIPAR towing tank. (**b**) CEHIPAR towing tank carriage.

is considered in normal operation conditions, these types of platform typically have periods ranging from 10 to 30 s and amplitudes from 3 to 12 m (see Azcona et al. [2]).

For the experimental validation of the implementations in the code, four different configurations of the scaled upwind mooring line are analyzed:

1. The isolated scaled mooring line.
2. The same line with the addition of a single clump weight at location 1.
3. The same line with the addition of a single clump weight at location 2.

Additionally, a line with a single clump weight at location 1 but with the same initial pretension as the line without clump weight is analyzed. The details of the positions chosen for the clump weights are described in Section 4.2.1.

Following the general statements of the dimensional analysis, the maximum possible number of terms are scaled in the differential equation that represents the mooring line Eq. (4.1).

$$\gamma\ddot{\mathbf{R}} - \frac{(\partial EA\varepsilon\mathbf{t})}{\partial l_0} - \mathbf{F}_D - \mathbf{F}_W - \mathbf{F}_{CW} - \mathbf{F}_{AM} = 0, \tag{4.1}$$

where $\mathbf{F}_D$, $\mathbf{F}_W$, $\mathbf{F}_{CW}$, $\mathbf{F}_{AM}$ are the drag, weight in water, clump weight, and added mass forces to the mooring line, respectively, γ is the mass per unit length of the mooring line, $\ddot{\mathbf{R}}$ is the acceleration of the line element and the partial differential term is the tension of the line element, where ε and $\mathbf{t}$ are the deformation of the line element and the vector tangential to the line element, respectively. Bold text denotes vectorial notation.

This implies scaling the dominant hydrodynamic loads apart from the weight of the mooring line and the inertial loads. However, as the Reynolds number in the experiments is far from the full-scale value, the hydrodynamic loads due to drag are not scaled according to the

scaling laws and a different scale factor is chosen for the diameter of the chain. More details of the dimensional analysis can be found in Lopez-Olocco et al. [89].

Table 4.1 summarizes the most important properties of the full-scale mooring system. The dimensional analysis performed in Webster [136] is extended to this case where the clump weight is attached to the mooring line using a line scale factor λ. As the OC4-DeepCWind is placed at a 200 m water depth and the CEHIPAR calm water tank has a 6.5 m water depth, a scale factor $\lambda = 30$ is chosen.

Table 4.1: OC4-DeepCWind mooring system properties [121].

	Value	**Units**
Number of mooring lines	3	–
Angle between adjacent lines	120	deg
Depth to Anchors below SWL	200	m
Depth to fairlead below SWL	14	m
Radius to Anchors from Platform Centerline	837.6	m
Radius to fairleads from Platform Centerline	40.868	m
Unstretched mooring line length	835.5	m
Mooring line diameter	0.0766	m
Equivalent mooring line mass density	113.35	Kg/m
Equivalent mooring line mass in water	108.63	Kg/m
Equivalent mooring line extensional stiffness	753.6 $\times 10^6$	N
Hydrodynamic Drag coefficient for mooring lines	1.1	–
Hydrodynamic added-mass coefficient for mooring lines	1.0	–
Seabed drag coefficient for mooring lines	1.0	–
Structural damping of mooring lines	2.0	%

For scaled experiments, a 27 m long DIN5685A studless chain was selected as its properties are close to the OC4-DeepCWind platform's mooring system when the non-dimensional ratio of $\lambda = 30$ is used. The chain used for the dynamic load test is made of stainless steel, see Fig. 4.3 where the main dimensions are indicated. The diameter D_w of the chain is 7 mm and the length L is 27 m. The length of the link t_w is 16 mm and the diameter of the chain link d_w is 2 mm. The measured mass per unit length γ of the mooring line is 67.8 g/m. These values approximate those used by other reference works in the literature, such as Azcona et al. [2], Barrera et al. [4].

When the chain is submerged, it acquires a typical catenary shape, see Fig. 4.4. The fairlead is connected to the moving and measurement devices and the bottom end of the chain is anchored to the floor. Special care has been taken to place the anchor at 25 m in the horizontal direction from the initial fairlead position for all the configurations. In this way, the theoretical objective pretension was ensured.

The dimensions of the model-scale clump weight are defined as follows. Assuming typical industrial values of a clump weight, this is a weight in water of 1 Tn, a cylindrical shape volume is approximately $V_{CW} = 2.4\ m^3$ ($D_{CW} = 1.5\ m$, $L_{CW} = 1.33\ m$). An example of an

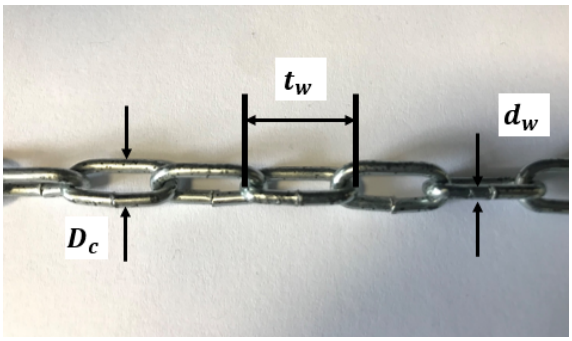

Figure 4.3: Main dimensions of the selected chain.

industrial clump weight is shown in Fig. 4.5. In our case, instead of using a block shape, the clump weight design was modeled as a rigid circular disc characterized by a length L_{CW} and a diameter D_{CW}, in order to maximize drag.

The chosen values for the scaled clump weight are collected in Table 4.2 and the manufactured

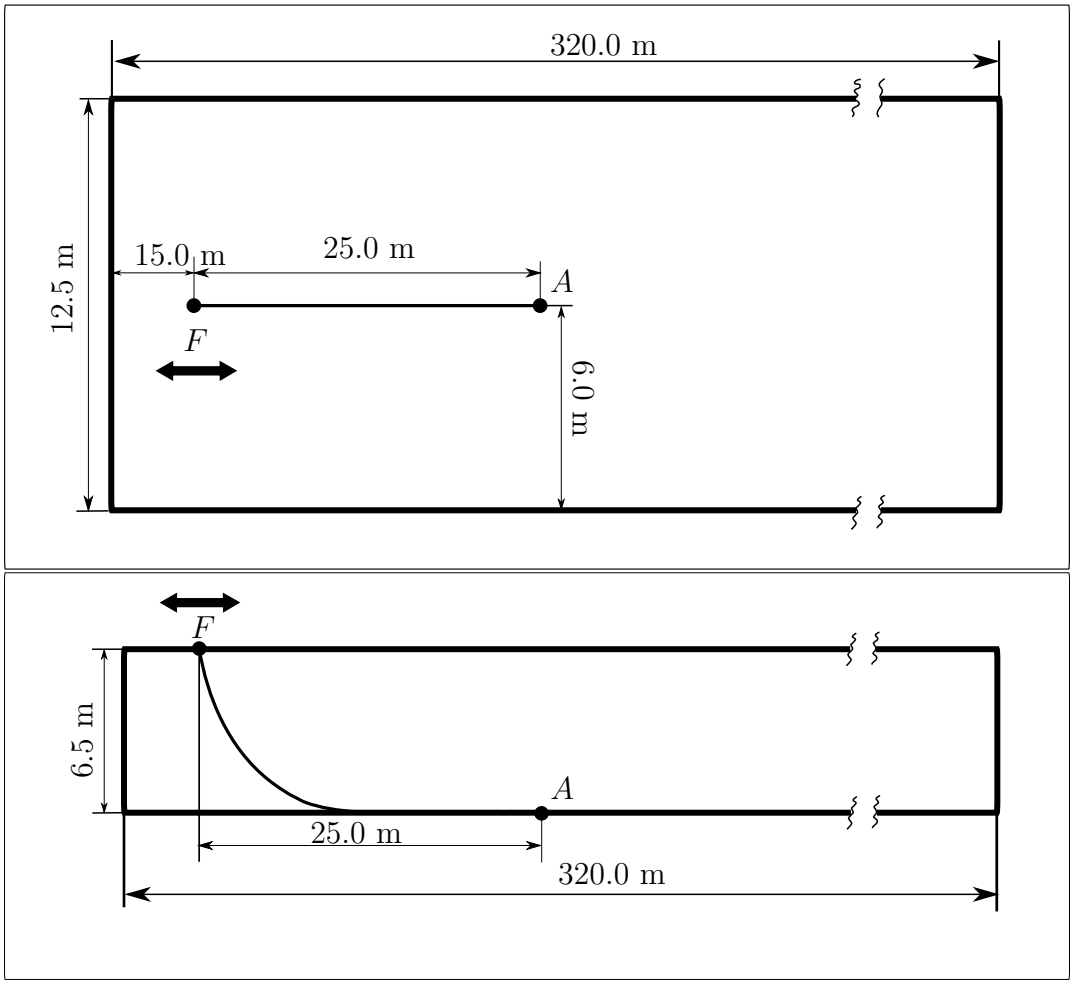

Figure 4.4: Schematic layout of the top and side views of the experimental setup.

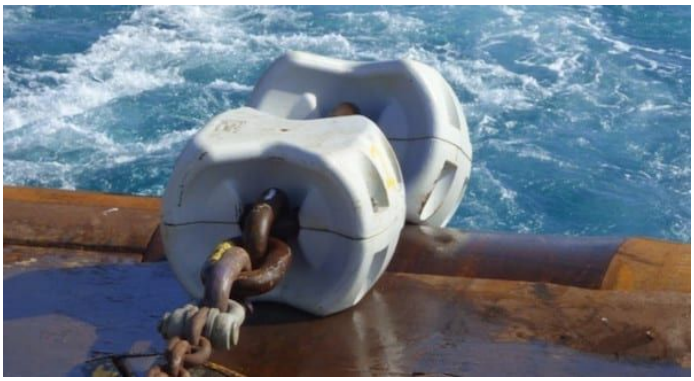

Figure 4.5: Typical clump weight used in the offshore industry.

device is shown in Fig. 4.6. The manufacturing of the scaled clump weight was simple. First, a mold was made on a milling machine with precise dimensions. The mold was then used to construct the device using resin with the desired density to achieve the necessary mass. After that, the holes were drilled to attach the device to the line.

Table 4.2: Involved variables in the design of the scaled clump weight.

	Symbol	**Value**	**Units**
Mass	$(M_{cw})_m$	122.0	g
Volume of displaced water	$(V_{cw})_m$	80.0	cm^3
Diameter	$(D_{cw})_m$	82.3	mm
Width	$(L_{cw})_m$	16.5	mm

The clump weight was attached directly to the chain, as shown in Fig. 4.6. The same line has been used for all configurations of the experimental campaign. Consequently, to insert the devices, the chain was cut twice, one for each position of the clump weight. Special care has been taken to preserve the total length of the line for each configuration. After the aforementioned procedure, the static tension of the line at the fairlead was measured before prescribing the imposed motions.

The fairlead was connected to both a load cell and a dynamometer through a metal ring. The measuring devices where fixed to an aluminum beam. Fig. 4.7 shows the described connection. The auxiliary aluminum structure was connected to a linear guide designed to impose surge motions on the water tank when connected to the actuator.

The motions were generated by a mechanical actuator driven by an electrical motor fixed in the structure above the towing carriage shown in Fig. 4.2. The maximum acceleration that the motor–actuator system could provide was 1.2 m/s^2, which is higher than the maximum acceleration required in the test matrix for this experimental campaign.

To measure the axial tension load of the mooring line, the one-component load cell HBM with an SG full bridge was used. To ensure a precise measurement of the tension regardless of the chain rotation, the connection of the load cell to the beam attached to the actuator allowed

Figure 4.6: Designed and manufactured scaled clump weight (**left**) and snapshot of the clump weight installed in the mooring line obtained with the submerged camera (**right**).

the load cell to freely rotate, as can be seen in Fig. 4.7. In addition, to prevent the ingress of humidity into the device during the experiments and alter the measurements, it was covered with a special foam material.

As it is necessary to simultaneously measure both the horizontal and vertical components of the fairlead tension, a 6 DOF dynamometer was also used. The fairlead motions of the mooring line were obtained by a double numerical integration using the trapezoid rule of the acceleration signal measured with a three-component accelerometer HBM with an SG full bridge.

Figure 4.7: The load cell and dynamometer connection to the aluminum beam attached to the linear guide.

In this facility, neither the side walls nor the bottom of the water tank are made of transparent material, so a low-cost submerged camera was used to record the line movements. An underwater BARLUS camera was used to record the evolution of the mooring line.

The technical characteristics of the electrical motor and measuring devices can be found in Lopez-Olocco et al. [89]. Also, the calibration and determination of uncertainties of the sensors are described in detail in the Appendix of the referred publication.

Special care was taken to place the camera's line of sight perpendicular to the plane of the catenary-shaped line. The camera was fixed to an auxiliary structure to ensure the same position throughout the experimental campaign. The distance between the camera and the line was selected to record the largest area possible to obtain the best image quality with minimal optical error. A first calibration process was addressed to determine the equivalent distance of a pixel image.

In order to represent the kinematics of a discrete number of points of the mooring line, equally spaced red marks were distributed along the mooring line. The distance between two adjacent marks along the mooring line is approximately 27 *cm* and the exact position of these markers is provided in Table 4.3. The trajectories of the marks were obtained by image processing. As discussed in Chapter 2, this kind of experiments can be also found in the literature, with isolated chains (see Azcona et al. [2], Barrera et al. [4]), but none is found when clump weights are added to the line.

Table 4.3: Position of the red marks used for capturing the line movements.

Marker Number	**Position along the Line Measured from the Fairlead (m)**
1	1.62
2	1.89
3	2.16
4	2.43
5	2.70
6	2.97
7	3.24
8	3.51
9	3.78
10	4.05
11	4.32

4.2.1 Test matrix

The surge motions of the fairlead are driven by an electrical motor placed on the top of the carriage. The imposed top-end surge motions are sinusoidal motions described by Eq. (4.2).

$$\delta = A \sin \frac{2\pi t}{T}, \tag{4.2}$$

where δ represents the fairlead horizontal displacement with respect to the position where the pretension is measured, A and T represent the imposed amplitude and period, respectively. The amplitude values used are in the range [0.125,0.225] m, which correspond to [3.875,6.975] m at real scale, and are presented in Table 4.4. Model-scale and the corresponding full-scale periods are presented in Table 4.5.

Table 4.4: Amplitudes of the fairlead motions for $\lambda = 1/30$.

ID	**Model Scale (m)**	**Full Scale (m)**
A01	0.225	6.975
A02	0.200	6.200
A03	0.175	5.425
A04	0.150	4.650
A05	0.125	3.875

Table 4.5: Fairlead motions periods in seconds for $\lambda = 1/30$.

ID	**Model Scale**	**Full Scale**
T01	2.80	15.590
T02	3.00	16.703
T03	3.50	19.487
T04	4.00	22.271
T05	4.50	25.055
T06	5.00	27.839
T07	5.50	30.623

A total number of 105 dynamic tests were conducted. The time duration of the force measurement for each case was about 180 s to ensure an acceptable number of cycles in the periodic regime, according to ITTC standards [63]. For each amplitude and period, four configurations have been tested: in the first one, no clump weight is used and, then two other configurations that include a clump weight are used, the clump weight is placed at $L_s/3$ (Configuration 1, position 1) and $L_s/2$ (Configuration 2, position 2) from the fairlead, where L_s is the suspended length of the line. Additionally, an additional configuration in which the initial pretension of the line is preserved but the clump weight is placed at the same position as Configuration 1. To see the clump weight location in each configuration, Fig. 4.8 shows the catenary-shaped mooring line in the three configurations in which the pretension is not preserved. As shown, the three lines are almost overlapping, the catenary shape is slightly changed in each configuration.

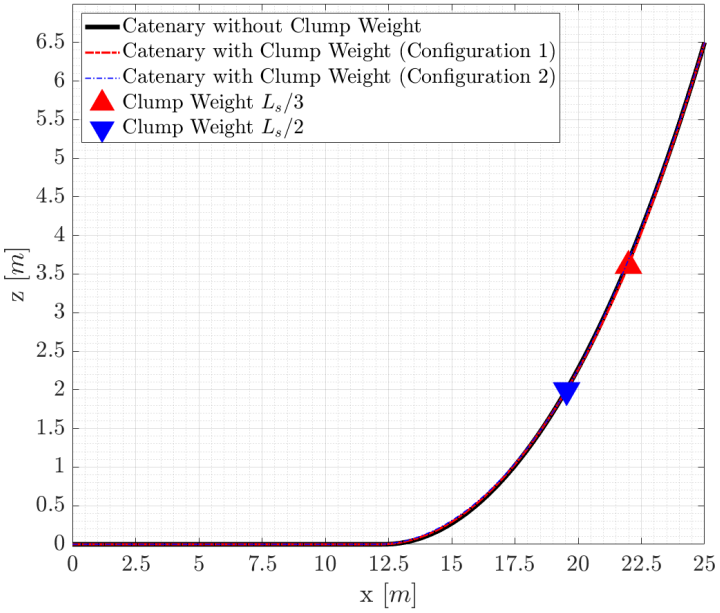

Figure 4.8: Catenary shape of all the tested configurations.

4.3 Numerical implementation: Theoretical background

4.3.1 Quasi-static approach

For the quasi-static analysis, the analytical solution of a catenary line detailed in Jonkman [71] is used. The equations for a line, with a portion of the line resting on the seabed, are as follows.

$$x_F - x_A = L - \frac{V_F}{\gamma_w} + \frac{H_F}{\gamma_w}\ln\left[\frac{V_F}{H_F} + \sqrt{1+\left(\frac{V_F}{H_F}\right)^2}\right] + \frac{H_F L}{EA} + \frac{C_B\gamma_w}{2EA}\left[-\left(L-\frac{V_F}{\gamma_w}\right)^2 + \left(L - \frac{V_F}{\gamma_w} - \frac{H_F}{C_B\gamma_w}\right)MAX\left(L-\frac{V_F}{\gamma_w}-\frac{H_F}{C_B\gamma_w}, 0\right)\right], \tag{4.3}$$

$$z_F - z_A = \frac{H_F}{\gamma_w}\left[\sqrt{1+\left(\frac{V_F}{H_F}\right)^2} - 1\right] + \frac{V_F^2}{2EA\gamma_w}, \tag{4.4}$$

and

$$\gamma_w = \frac{\rho_c - \rho_0}{\rho_c}\gamma g, \tag{4.5}$$

where L is the total unstretched length of the line, EA is the extensional stiffness, γ_w is the apparent weight in fluid per unit length, C_B is the seabed friction coefficient, H_F and V_F are the horizontal and vertical forces applied at the fairlead, respectively, ρ_c is the density of the

chain, ρ_0 is the density of the water, γ apparent mass per unit length of the chain, and g is the acceleration due to gravity.

When the line does not rest on the seabed, the analytical formulation represented by the Eq. (4.3) and (4.4) are replaced by Eq. (4.6) and (4.7). Note that the equations are presented slightly differently than in [71] due to the change in the reference system and the assumption that the chain is modeled as a Morison's slender cylinder.

$$x_F - x_A = \frac{H_F}{\gamma_w}\left\{\ln\left[\frac{V_F}{H_F} + \sqrt{1+\left(\frac{V_F}{H_F}\right)^2}\right] - \ln\left[\frac{V_F-\gamma_w L}{H_F} + \sqrt{1+\left(\frac{V_F-\gamma_w L}{H_F}\right)^2}\right]\right\} + \frac{H_F L}{EA} \tag{4.6}$$

$$z_F - z_A = \frac{H_F}{\gamma_w}\left[\sqrt{1+\left(\frac{V_F}{H_F}\right)^2} - \sqrt{1+\left(\frac{V_F-\gamma_w L}{H_F}\right)^2}\right] + \frac{1}{EA}\left(V_F L + \frac{\gamma_w L^2}{2}\right) \tag{4.7}$$

A scheme of the mooring line, in which a clump weight has been added, is illustrated in Fig. 4.9. The line can be divided into two segments, the first segment going from the anchor to the point mass position, while the second starts at the point mass location to the fairlead position. The equations of the catenary are applied to each segment before and after the clump weight was added and solved together as a nonlinear system of six equations: four catenary Equations (4.3), (4.4), (4.6), and (4.7) and two extra equations for the local force equilibrium at the position of the clump weight (4.8) and (4.9)). A Newton–Raphson iterative method is used to solve the resulting system of 6 nonlinear equations (4.3-4.9) with 6 unknowns: H_F and V_F of the two segments, the position of the clump weight (x_P and z_P).

$$T_{Hs1} - T_{Hs2} = 0 \tag{4.8}$$

$$T_{Vs1} - (T_{Vs2}) - P = 0 \tag{4.9}$$

4.3.2 Dynamic approach

4.3.2.1 Basic dynamic equations

Using the finite element method, the partial differential Equation (PDE) (4.10) which models the mooring line elements is transformed into a nodal system of ordinary differential equations (ODE). This ODE system is discretized in time and solved by the OPASS code [2].

$$\gamma\ddot{\mathbf{R}} + C_4\left(1+\varepsilon\right)\left[\ddot{\mathbf{R}} - \left(\ddot{\mathbf{R}}\cdot\mathbf{t}\right)\mathbf{t}\right] - \frac{\left(\partial EA\varepsilon\mathbf{t}\right)}{\partial l_0} - \frac{\left(\partial\beta EA\dot{\varepsilon}\mathbf{t}\right)}{\partial l_0} - \mathbf{F_1} - \mathbf{F_2} - \mathbf{F_3} = 0, \tag{4.10}$$

where γ is the line mass per unit of mooring line unstretched length, $\mathbf{R}$ is the position of the line element analyzed, $\mathbf{t}$ is the vector tangential to the line at the point analyzed, ε is the deformation, EA is the extensional stiffness, C_4 is constant for the calculation of the hydrodynamic inertial force per unit of unstretched line length, β is a coefficient for the calculation of the structural damping force, and l_0 is the location of the point analyzed along the line.

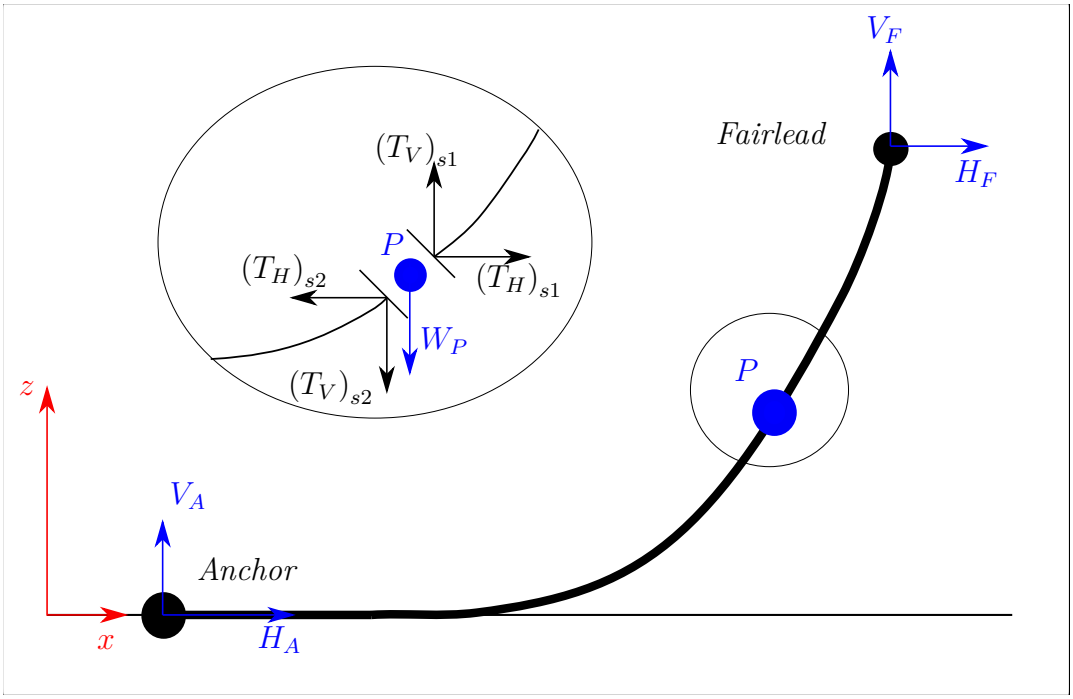

Figure 4.9: Free body diagram of a mooring line with a clump weight positioned at point P.

The external forces $\mathbf{F_1}$, $\mathbf{F_2}$, $\mathbf{F_3}$ are the resultant forces from weight in water, the tangential and normal drag components, respectively, per unit of unstretched length. These hydrodynamic forces are modeled by Equations (4.11)–(4.13).

$$\mathbf{F_1} = -\gamma_r g\mathbf{k} = -\frac{\rho_c - \rho_0}{\rho_c}\gamma g\mathbf{k}, \tag{4.11}$$

where γ_r is the mass in water per unit length of the element, and $\mathbf{k}$ is the unit vector parallel to the z axis.

The normal and tangential drag forces are modeled by the Morison equation [102], as follows:

$$\mathbf{F_2} = C_2\,(1+\varepsilon)\,V_t^2\mathbf{t} = \frac{1}{2}C_{dt}D\rho_0\,(1+\varepsilon)\,V_t^2\mathbf{t} \tag{4.12}$$

$$\mathbf{F_3} = C_3\,(1+\varepsilon)\,V_n^2\mathbf{n} = \frac{1}{2}C_{dn}D\rho_0\,(1+\varepsilon)\,V_n^2\mathbf{n}, \tag{4.13}$$

where the vector $\mathbf{V} = V_t\mathbf{t} + V_n\mathbf{n}$ denotes the relative velocity between the water and the mooring line, expressed by its tangential and normal components. Moreover, C_2 and C_3 are coefficients used to model the hydrodynamic forces to simplify notations (C_{dt} and C_{dn} are the tangential and normal drag coefficients of the bare line, and D is the diameter of the line element).

Using bar elements for the spatial discretization of the mooring line, linear polynomials for the elements' internal interpolation of the line motions, and 0-order polynomials for the mass

and added mass terms, the global equation of motion is condensed into Eq. (4.14)

$$M \cdot \ddot{\mathbf{X}} + C \cdot \dot{\mathbf{X}} + K \cdot \mathbf{X} - \mathbf{F} = 0, \tag{4.14}$$

where M is the mass matrix of the system, C is the damping matrix, K is the stiffness matrix, $\mathbf{F}$ is the vector of external forces, and $\ddot{\mathbf{X}}$, $\dot{\mathbf{X}}$, and $\mathbf{X}$ are, respectively, the vectors of acceleration, velocities, and positions of the line DOF defined at the nodes.

4.3.2.2 Clump Weight implementation

The presence of a clump weight modifies the system of equations (4.14), where an additional weight in water, drag, inertia, and added mass due to the clump weight are added to the matrix system. A rigid union between the clump weight and the mooring line is assumed, where all local forces due to the clump weight are distributed per unit length. The external forces acting on the mooring line element i are weight in water $\mathbf{F_{1i}}$, tangential drag $\mathbf{F_{2i}}$ and normal drag $\mathbf{F_{3i}}$, and the added mass $\mathbf{F_{4i}}$.

The weight of the mooring line element is increased by the weight of the clump weight, resulting in an external force for that element (see Eq. (4.15)).

$$\mathbf{F_{1i}} = -\left(\gamma_r g + \frac{W_{CW}}{L_i}\right)\mathbf{k}, \tag{4.15}$$

where W_{CW} is the weight of the Clump Weight in water and L_i is the length of the chain element. As described in Section 4.2, the shape of the clump weight is a circular disk represented as a schematic view in Fig. 4.10.

In Chapter 3 is demonstrated that, despite some small magnitude differences, the hydrodynamic forces of the clump weight can be modeled with a quasi-static empirical model with reasonably good engineering results. Therefore, for elements that include a clump weight, the mooring line coefficients used are modified using additional linearized viscous drag and added mass coefficients of the attached device.

The coefficient to model the tangential drag forces of the line C_2 is replaced by the coefficient C_2^{CW} presented in Eq. (4.16):

$$C_2^{CW} = \frac{1}{2}\rho_0 C_{dt} D + \frac{1}{2}\rho_0 C_{dtCW}\frac{\pi D_{CW}^2}{4}\frac{1}{L_i}, \tag{4.16}$$

where the second term is the tangential drag force per unit length added by the clump weight. The tangential drag coefficient C_{dtCW} is interpolated for every time step according to its local clump weight Reynolds number, where the characteristic length used is the clump weight diameter D_{CW}. The selected C_D-Re curve for a disk is illustrated in White [138].

Regarding the inertial forces, the implementation of the clump weight impacts the mass matrix. The body mass of the element that includes the clump weight is increased, and the

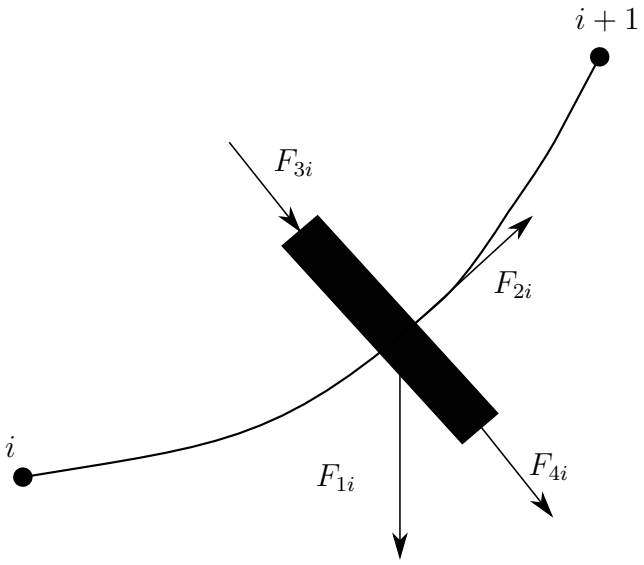

Figure 4.10: External forces acting on an element of line.

mass per unit length of the line γ of Eq. (4.10) is increased by the mass of the device per unit length of the line in a quantity of $\frac{m_{CW}}{L_i}$.

Similarly to drag forces, the added mass force per unit of unstretched line length is calculated in OPASS by replacing the coefficient C_4 based on a normal added mass coefficient C_{mn} for the Morison approach by the constant C_4^{CW} presented in Eq. (4.17).

$$C_4^{CW} = C_{mn}\rho_0\frac{\pi D^2}{4} + \frac{1}{3}\rho_0\frac{D_{CW}^3}{L_i}, \tag{4.17}$$

where the second term of Eq. (4.17) is the well-known theoretical ideal fluid added mass per unit length of the mooring line element for a circular disk described by Patton [112]. This term is only considered for those elements that include a clump weight.

4.3.2.3 Computational parameters used in the simulations

4.3.2.3.1 OPASS numerical tool The dimensions of the chain are described in Section 4.2. A mass per unit length $\gamma = 0.0678\ Kg/m$ and a wire diameter of the chain link $d_w = 2\ mm$ were measured. Eq. (4.18) determines the axial stiffness in kN when d_w is in meters of the chain used in the simulations [111].

$$EA = 0.854 \cdot 10^8 d_w \tag{4.18}$$

As the computational model considers the chain to be a line with a constant circular section (Morison approach), an equivalent hydrodynamic diameter has to be determined. Consequently, the diameter of the equivalent circular section was calculated assuming the same mass per unit length of the chain, see Eq. (4.19). This procedure is based on the assumption that in

catenary mooring lines, the weight in water has a dominant effect on motions, loads, and restoring forces.

$$D = \sqrt{\frac{4\gamma}{\pi\rho_c}} \tag{4.19}$$

The added mass coefficient C_{mn} of 1.0 is determined following the standards NR 493 R02 E [33] and the normal and tangential drag coefficients C_{dn} and C_{dt} were obtained following the indications of DNV-OS-E301 [30]. For a studless chain, this guideline provides a value for C_{dn} of 2.4 and, for C_{dt}, a value of 1.15; these values correspond to the wire diameter of the chain link. For the numerical implementation, the values have to be referred to the equivalent hydrodynamic diameter, and in order to obtain the equivalent drag coefficient, the same drag force per unit length is assumed and proceed as follows:

$$C_{Dn} = \frac{C_{dn} d_w}{D} \quad ; \quad C_{Dt} = \frac{C_{tn} d_w}{D} \tag{4.20}$$

The seabed contact model implemented in OPASS uses bi-linear springs. When a node is in contact with the seabed, a spring with stiffness K_{sc} provides the floor reaction force per indentation depth and per unit of line length. A damping D_{sc} is also included in the model. The resulting parameters are summarized in Table 4.6.

Table 4.6: Parameters of the computational model.

	Value	**Units**
Equivalent hydrodynamic diameter (D)	0.0033	m
Unstretched Length (L)	27.0	m
Line mass density (ρ_c)	7850	Kg/m^3
Mass per unit length (γ)	0.0678	Kg/m
Axial stiffness (EA)	3.416×10^5	N
Coefficient for the structural Rayleigh damping (β)	0.0007	–
Added mass coefficient (C_{mn})	1.0	–
Normal drag coefficient (C_{Dn})	1.445	–
Tangential drag coefficient (C_{Dt})	0.697	–
Vertical seabed stiffness (K_{sc})	20.0	N/m^2
Vertical seabed damping (D_{sc})	0.1	Ns/m^2
Tangential friction coefficient (C_{ft})	0.0	–
Normal friction coefficient (C_{fn})	0.0	–

4.3.2.3.2 MoorDyn numerical tool As introduced in the abstract of this chapter, MoorDyn is also used to compare with the experiment and OPASS. Due to the similarity in the modeling of the line, the same computational parameters for the line are used for the MoorDyn model (see Table 4.6). However, the clump weight has been implemented in MoorDyn slightly different from that in OPASS. In MoorDyn, the discretization of the

line is selected in such a way that the location of the clump weight (in every configuration) corresponds to a node's location in the initial static equilibrium conditions. Subsequently, the submerged weight of the clump weight is designated as a nodal mass and displacement of that particular node. As for the drag forces, they are the result of multiplying a drag coefficient of 1.12 (disk) with the projected area of the scaled clump weight specified in the input file. Additionally, an equivalent added mass coefficient similar to the one in OPASS is selected.

4.4 Experimental results and numerical validation

4.4.1 Static cases

Once the shape and position of the catenary have been verified, the static tension measured by the load cell is compared to the quasi-static pretension predicted with the formulation described in Section 4.3.1. The largest difference in the experimental measures from the numerical predictions is approximately 0.21%, see Table 4.7. For the selected configurations in the experiments, the maximum difference in the initial pretension is obtained when the clump weight is placed in Configuration 2, resulting in an increase of 10% with respect to the mooring line without clump weight.

Table 4.7: Experimental-numerical comparison of pretension of each configuration.

Mooring configuration	Quasi-static numerical model $[N]$	Experimental measurement $[N]$
Without clump weight	11.51	11.49
With clump weight (Config. 1) - same pretension	11.51	11.48
With clump weight (Config. 1)	12.14	12.10
With clump weight (Config. 2)	12.41	12.42

Fig. 4.11 shows the horizontal tension curve of the line for each configuration as a function of the offset value. The offset distance is defined as the horizontal distance between the fairlead in the initial static equilibrium and the new fairlead location to analyze. As expected for a catenary line, the horizontal stiffness of the system is nonlinear, and, as observed, this does not change with the inclusion of the clump weight.

As expected, a higher line pretension means a stiffer system, therefore, for the same offset value, higher tension values for Config.1 and Config.2 are observed in Fig. 4.11. However, when the pretension is maintained, due to the weight addition, the horizontal component of the fairlead tension is reduced. As observed in Fig. 4.12, the magnitude of the vectors for the line without clump weight (black solid arrow) and the line with clump weight (red dashed arrow) is the same, but not for the components. This means that the geometric stiffness of the line is modified due to the angle change, and this is verified when the horizontal stiffness of the line is reduced when the clump weight is added in Config. 1 but with the same pretension (red dashed line), see Fig. 4.11.

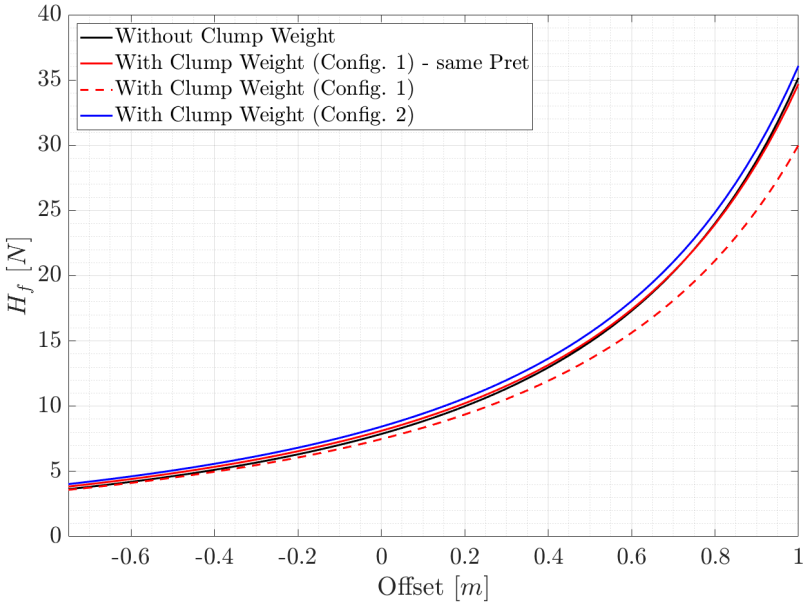

Figure 4.11: Horizontal stiffness of the line in all tested configurations.

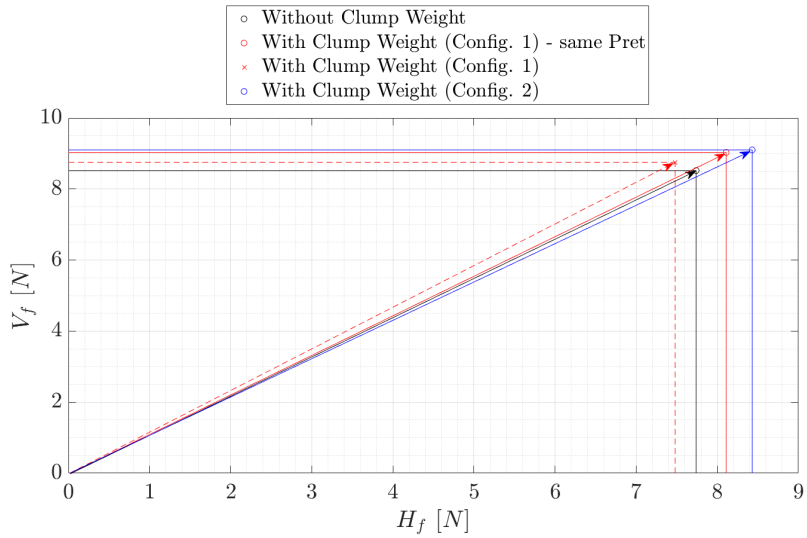

Figure 4.12: Pretension of the tested configurations - vector representation.

4.4.2 Dynamic cases

4.4.2.1 Tensions response

In this section, the fairlead tension measured by the load cell is represented and compared to the fairlead displacement for different values of the period $T = 2.8,\ 3.5,\ 5.5\ \ s$ and amplitudes $A = 0.125,\ 0.175,\ 0.225\ \ m$. After reaching a periodic regime and assuming that the measurements satisfy the ergodic theorem, the tension values are the time average during

20 periods and the vertical bars represent its standard deviation.

As shown in the results, the maximum and minimum values of the fairlead tension during the cycle are obtained for the minimum displacement relative to the initial position. As expected, it is observed that for constant amplitudes, smaller periods imply larger accelerations and tensions. Similarly, for constant periods, larger amplitudes also imply larger accelerations and fairlead tensions.

From Fig. 4.13, it is clearly observed that the effect of adding a clump weight to the isolated mooring line in the position closer to the fairlead (Config. 1) is to increase the fairlead tension for all amplitudes and periods. This can be expected due to the stiffer system produced by the higher pretension.

Similarly, in Fig. 4.14, the fairlead tension for the isolated mooring is also compared to the line with a clump weight at the location farther from the fairlead (Config. 2) for the same set of amplitudes and periods. It is observed that the change in the position of the clump weight position has an important influence on the magnitude of the increase of the fairlead tension. The maximum fairlead tension grows approximately the same magnitude as the weight of the attached device in Config. 1, while the maximum fairlead tension is increased by almost double of this weight in Config. 2. In other words, when clump weights are present and the pretension is increased, the maximum fairlead tension is increased by just 6% in Config. 1 and by 9% in Config. 2, with respect to the isolated mooring line. This result is aligned with the increased stiffness of the system since Config. 2 has a higher pretension than Config.1. The maximum and minimum fairlead tension of the complete test matrix cases can be checked in [89].

However, the result is different when the clump weight is added and the pretension is maintained. Fig. 4.15 shows the comparison of the fairlead tension measured by the load cell to the fairlead displacement for this case with and without clump weight. As can be observed, just the addition of the clump weight to the isolated mooring line slightly decreases the fairlead tension. This could be expected since the stiffness of the system was reduced, as already discussed in Section 4.4.1.

To fully understand this phenomenon of the reduction in tensions when pretension is maintained, Fig. 4.16 shows the comparison of the fairlead tension time series (with and without clump weight) for the case with the highest dynamic tensions, which is an amplitude $A = 0.225$ m and a period $T = 2.8$ s. It is observed that the maximum dynamic tension amplitude is reduced by a 4% when the pretension is maintained, while the dynamic tension peaks are larger than the line without clump weight when the clump weight is added, and pretensions are increased.

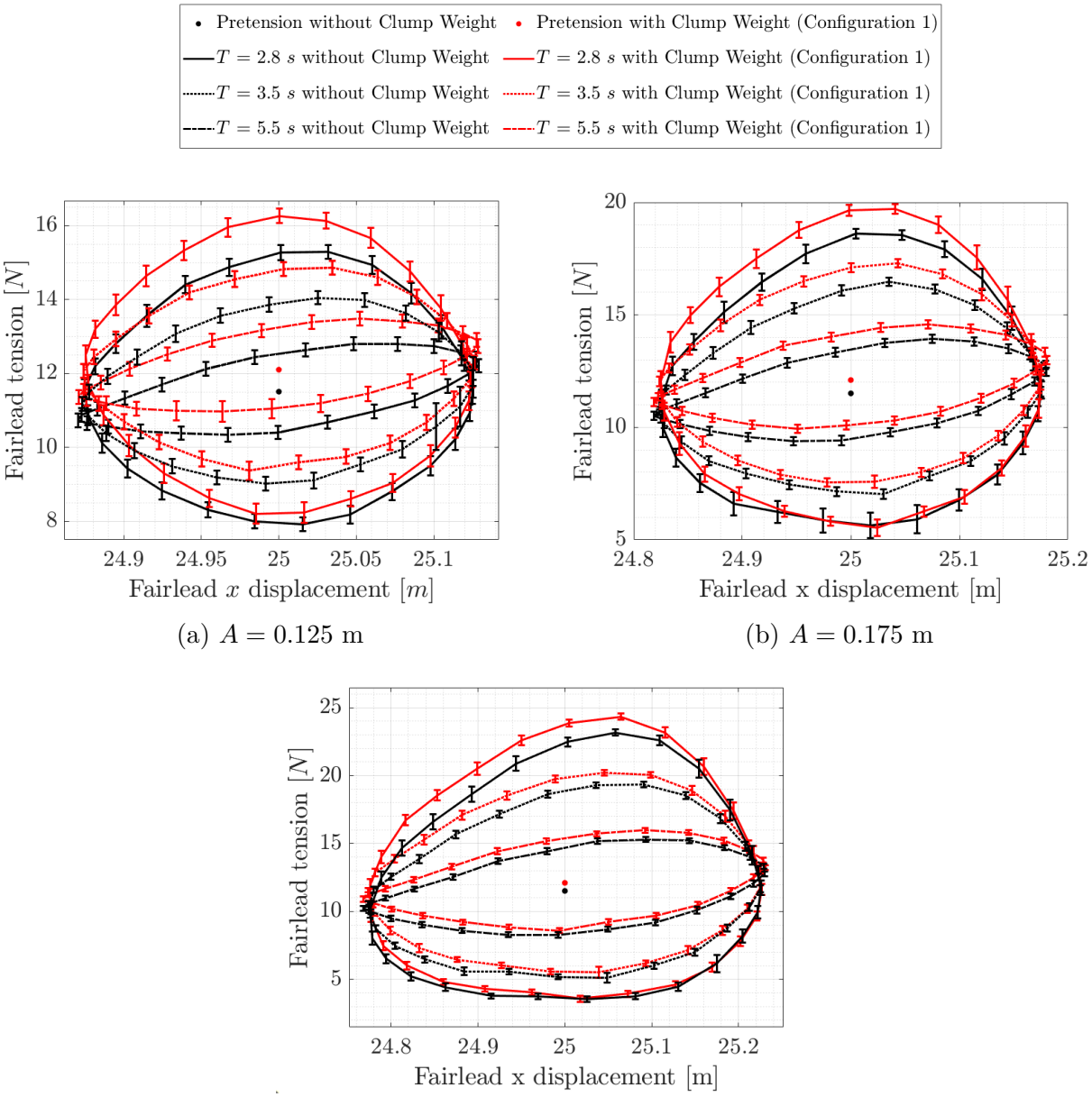

(a) $A = 0.125$ m

(b) $A = 0.175$ m

(c) $A = 0.225$ m

Figure 4.13: Fairlead tension during the fairlead displacement with and without clump weight for three different fairlead amplitude values for Configuration 1.

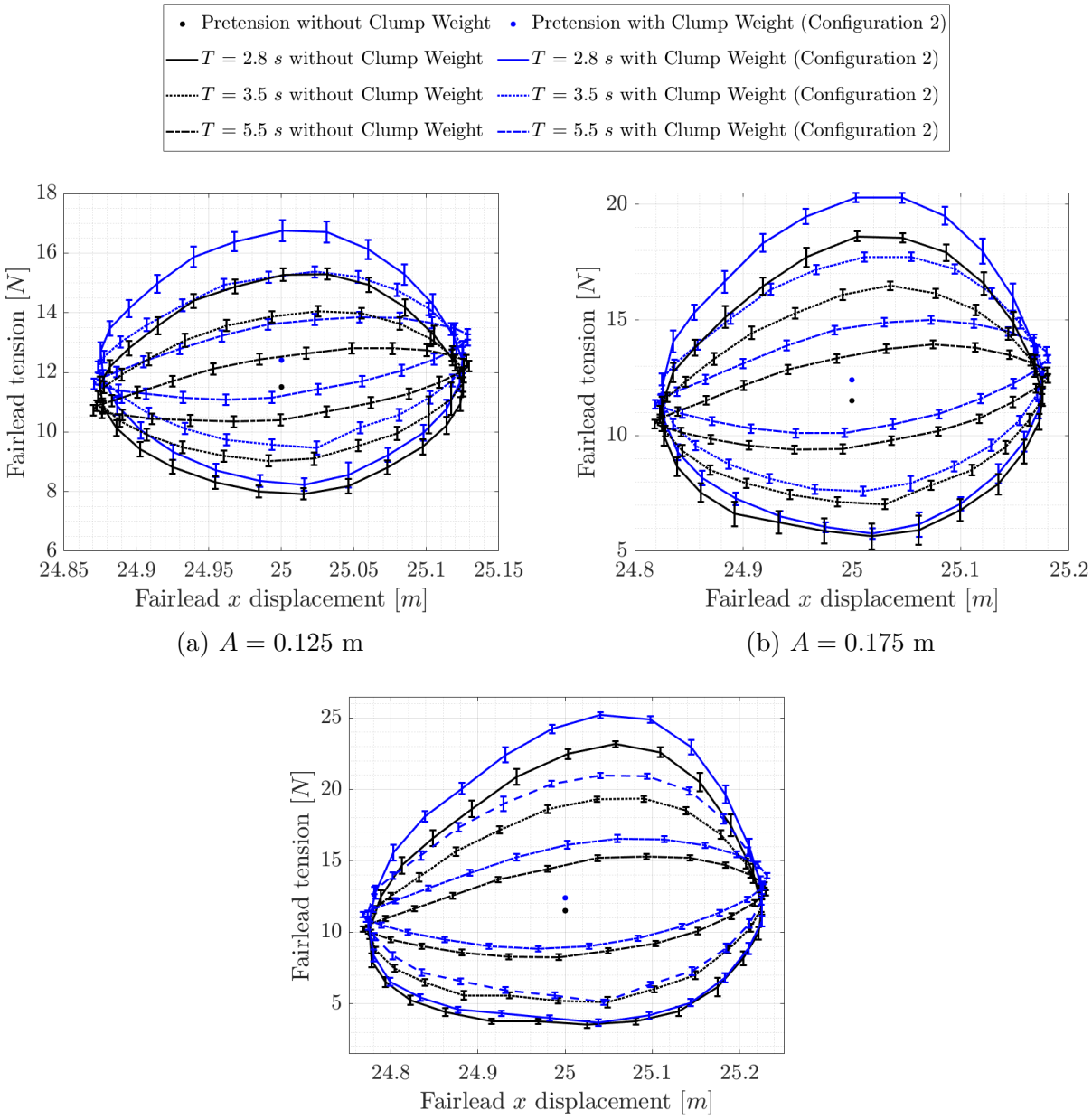

(a) $A = 0.125$ m

(b) $A = 0.175$ m

(c) $A = 0.225$ m

Figure 4.14: Fairlead tension during the fairlead displacement with and without clump weight for three different fairlead amplitude values for Configuration 2.

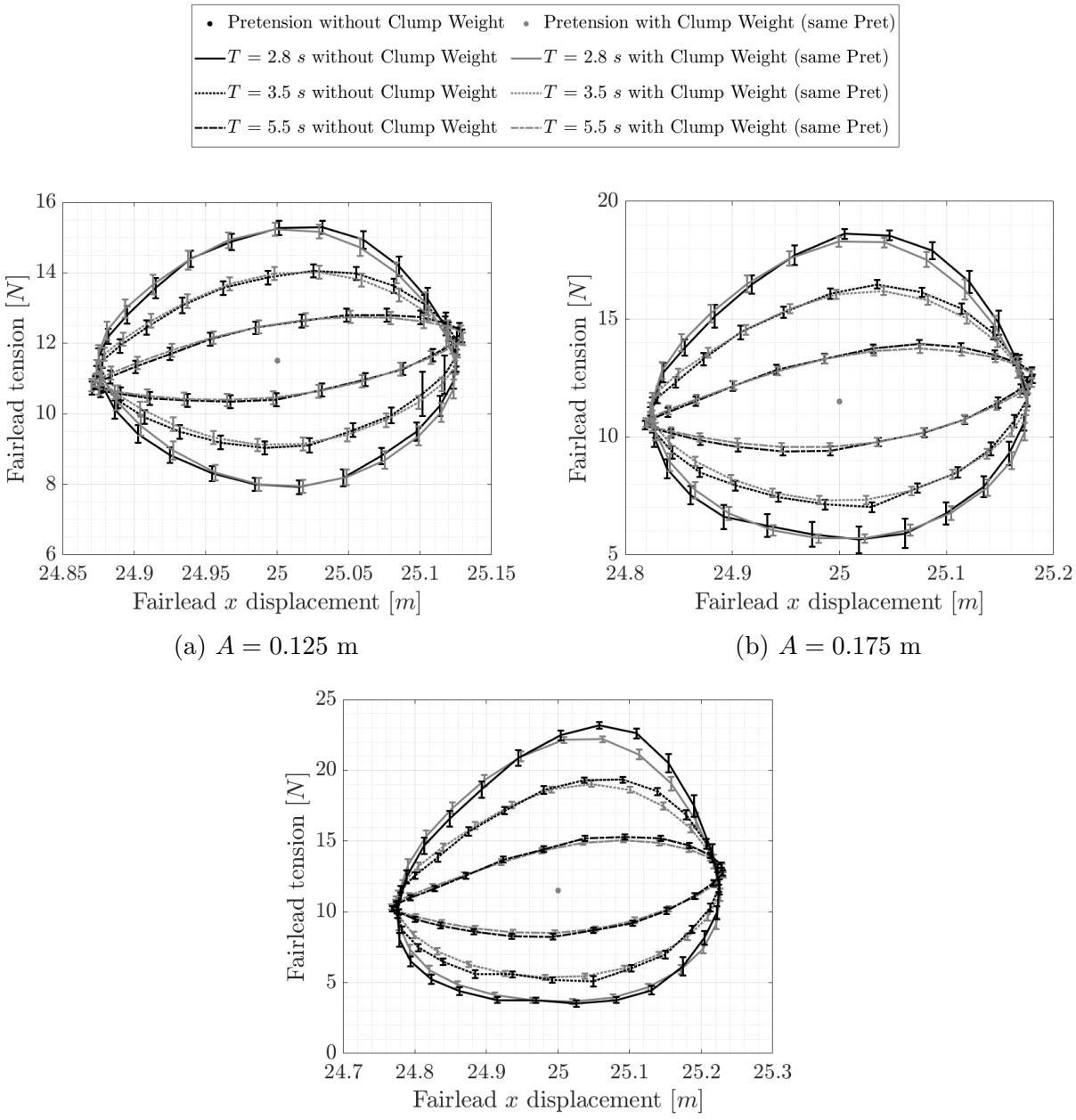

(a) $A = 0.125$ m

(b) $A = 0.175$ m

(c) $A = 0.225$ m

Figure 4.15: Fairlead tension during the fairlead displacement with and without clump weight for three different fairlead amplitude values for Configuration 1 (with the same pretension).

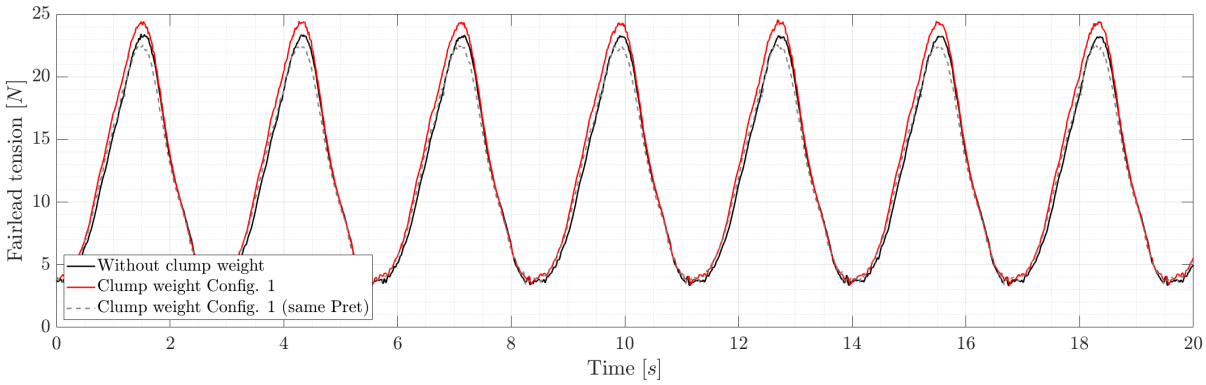

Figure 4.16: Experimental comparison fairlead tension time series for $A = 0.225\ m$ and $T = 2.8\ s$.

4.4.2.1.1 Dissipated energy The energy dissipation is calculated using the diagram method detailed in Webster [136], where the dissipated energy of the mooring line is the area enclosed in one cycle by the hysteresis loop:

$$E = \oint F_d \cdot d\delta, \tag{4.21}$$

where F_d and δ are the dissipation force and the displacement of the fairlead, respectively.

The dissipation of energy in a mooring line is mainly caused by structural damping, viscous drag with possible VIV, and friction with the seabed [116]. In this study, a simplification is made and the structural damping and friction with the seabed are considered negligible with respect to viscous drag. Therefore, the dissipation force can be modeled the following way.

$$F_d = F_D = \frac{1}{2}\rho_0 C_D D L_s \dot{\delta}^2 \tag{4.22}$$

Since displacement is periodic, $\delta = A \cdot sin(\omega t)$, the dissipation energy can be calculated as:

$$E = 4\int_0^{\delta_{max}} F_d \cdot d\delta = \frac{4}{3}\rho_0 D L C_D A^3 \omega^2 \tag{4.23}$$

The dissipated energy depends on several factors, such as frequency and amplitude, as shown in Figs. 4.13 and 4.14 where the enclosed areas are larger when the frequencies and amplitudes are increased.

The dissipated energy of the complete test matrix computed in non-dimensional form according to Eq. (4.21) is shown in Fig. 4.17. The non-dimensional dissipated energy is obtained by dividing by a reference potential energy, $A \cdot w \cdot H$, as performed by Webster [136]. The tendency of larger amplitudes to implicate a larger dissipated energy can be appreciated. This pattern is presented in several publications dealing with isolated mooring lines, e.g., Barrera

et al. [4], Li et al. [81], Yan et al. [142]. Similarly, smaller periods increase the dissipated energy. This is expected due to the higher acceleration that implies larger inertial loads, which are predominant in a catenary mooring line.

In addition, when clump weights are present, the pattern is consistent and dissipation increases in all imposed motions, regardless of the location along the line if the pretension is not maintained. In contrast, as expected, when pretension is not altered, the dissipation in all imposed motions is lower than the line without clump weight.

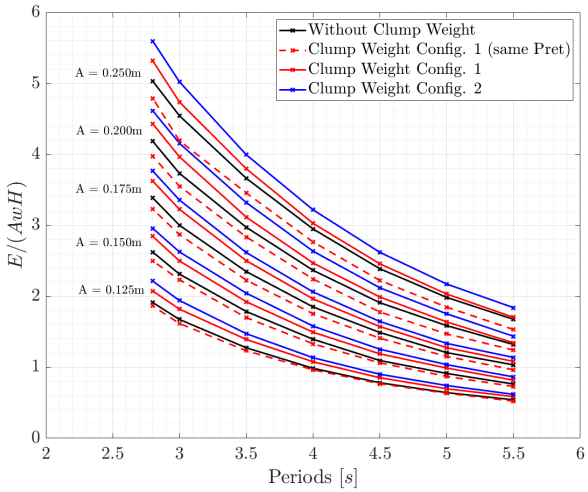

Figure 4.17: Dissipated energy for all the test matrix in the non-dimensional form.

The energy dissipated for the line without clump weight is plotted against $\omega^2 A^3$ in Fig. 4.18 for all the motions of the test matrix. Similarly to Li et al. [81], a good linear fit is achieved for the experimental results. The same linear tendency is also observed when clump weights are added in all configurations.

Assuming that the damping coefficient C_D can be obtained from the slope of the fitted curves, which is $\frac{4}{3}\rho_0 DLC_D$, the mean value obtained for the complete test matrix was $C_D = 1.75$ for the isolated mooring line, which is a little higher than the standard value used for simulations $C_{Dn} = 1.455$, see Section 4.3.2.3. The mean values of C_D obtained when clump weights are present were 1.82 and 1.90 for Config. 1 and Config. 2, respectively. This increase in the damping coefficient explains why the line dissipates more energy when clump weights are added. In contrast, the mean value of C_D obtained when the clump weight is present but the pretension is maintained is $C_D = 1.64$, this also explains why the line dissipates less energy in this case when the clump weight is added.

The non-dimensional increase of dissipated energy due to the clump weight is expressed by Eq. (4.24).

$$\frac{\Delta E}{E_{CW}} = \frac{\Delta E}{\rho_0 A^3 \omega^2 D_{CW}^2} \tag{4.24}$$

The dimensionless increase of dissipated energy for all clump weight configurations with

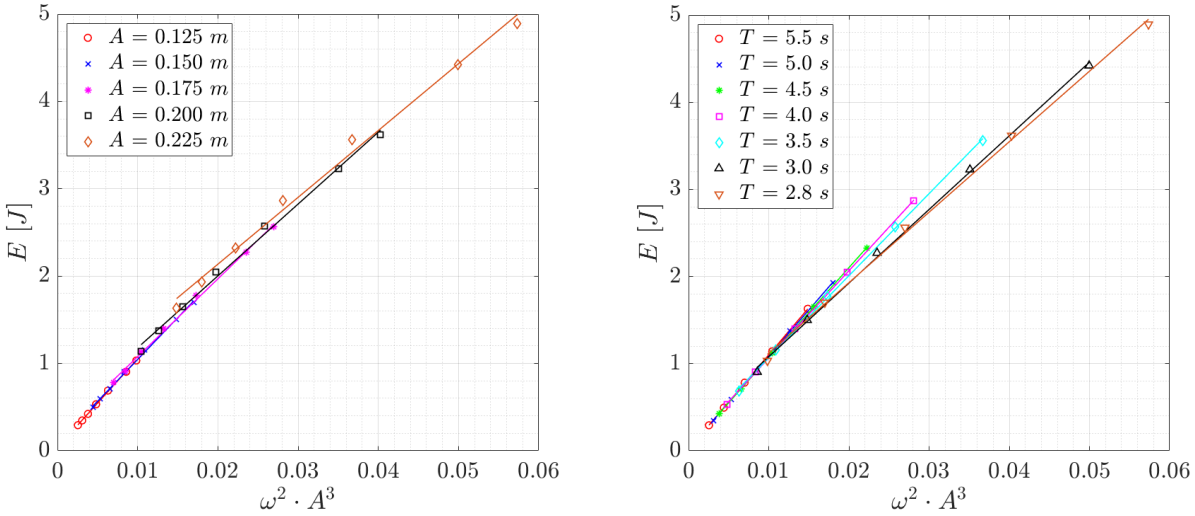

Figure 4.18: Dissipated energy under the imposed top-end motions for the mooring line without clump weight.

respect to the line without clump weight, for each of the different amplitudes and periods tested, is shown in Fig. 4.19. Config. 2 shows an evident increase in the dissipated energy, almost two times higher than that of Config. 1 for all cases. It is clearly observed that the dissipated energy of the mooring line is lower in the case where the pretension is maintained.

The amplitude of the motion has more influence than the period in the increase of dissipated energy, as seen in Fig. 4.19. The presence of the clump weights shows a more dominant effect for smaller amplitudes in terms of dissipated energy. When the clump weight is added and the pretension is maintained, the dissipated energy gets decreased but remains almost constant in all the amplitude range.

When the clump weight is closer to the fairlead and the pretension is increased, the line dissipates less energy than when placed further away. Therefore, setting the clump weight farther from the fairlead with the obvious limitation of seabed contact could be an adequate practice to reduce the surge motion of the moored platform. Keeping in mind that in this scenario, the role of the clump weights is also to increase the dissipated energy, the clump weight's presence is more effective in terms of non-dimensional energy dissipation when low amplitude motions of the fairlead are present. However, in the scenario in which a fairlead tension reduction is intended, the presence of the clump weight while maintaining the pretension seems more effective, since the tension reduction could be achieved due to the geometric stiffness reduction.

4.4.2.1.2 Numerical validation The implementations in the numerical code OPASS have been validated with these new experimental results, where the clump weights are part of the mooring line. First, the fairlead tension in the absence of clump weights has been computed and compared with the experimental results for three oscillation periods $T = 2.8,\ 3.5,\ 5.5\ s$ and three amplitudes $A = 0.125,\ 0.175,\ 0.225\ m$ in Fig. 4.20. As can

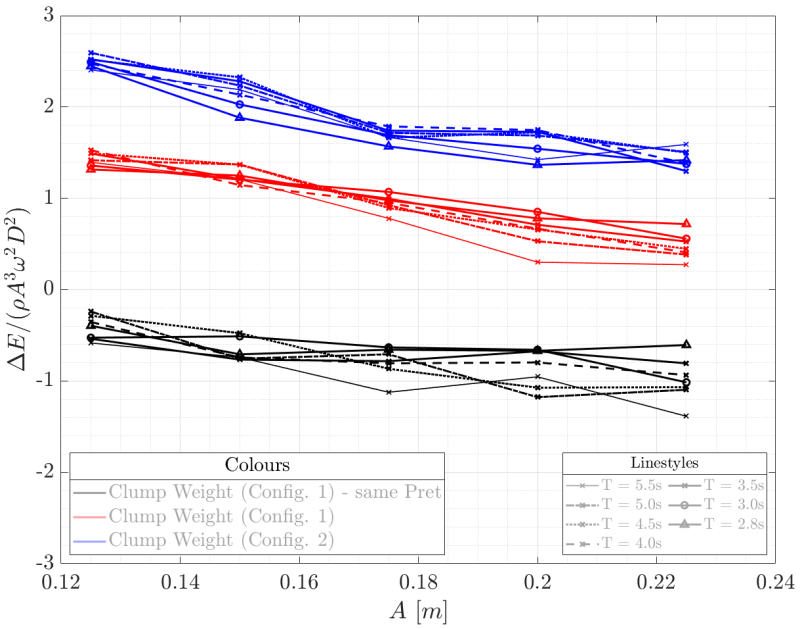

Figure 4.19: Dimensionless increase of dissipated energy due to the clump weights.

be observed, the prediction of the numerical tool OPASS approximates the values measured in the experiments for all periods and amplitudes tested very well. The comparison with MoorDyn is very similar, achieving slightly better results for the dynamic higher acceleration tension, but less accurate in the lower acceleration part, especially in the lower amplitude case ($A = 0.125\ m$). This discrepancy can be caused by the values chosen for the hydrodynamic coefficients, which can show a dependency or correlation with the velocity (a function of the amplitude and period of the forced oscillation), and the constant value provided by the standards may be varied to account for that. However, the differences for both numerical tools are still acceptable, achieving a maximum error of around 4% for the maximum tension.

When the clump weight is added, the prediction of the numerical code with the implementations is still valid, see Figs. 4.21 and 4.22. From these figures, a slightly over-predicted fairlead tension can be observed under the maximum tension conditions both for OPASS and MoorDyn. This tendency appears in all the cases tested. In addition, the numerical code can capture the increase of the fairlead tension in approximately the same proportion as the experimental results shown in Figs. 4.13 and 4.14 due to the clump weight inclusion.

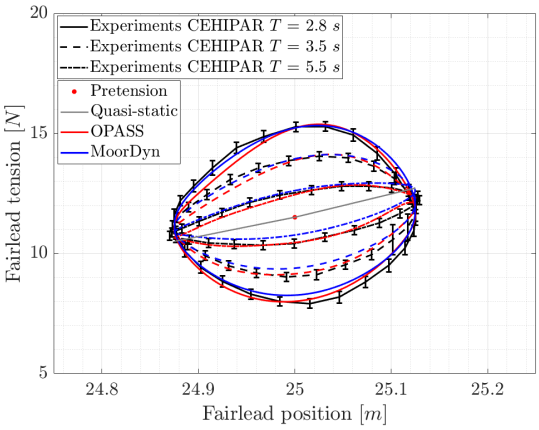

(a) $A = 0.125\ [m]$

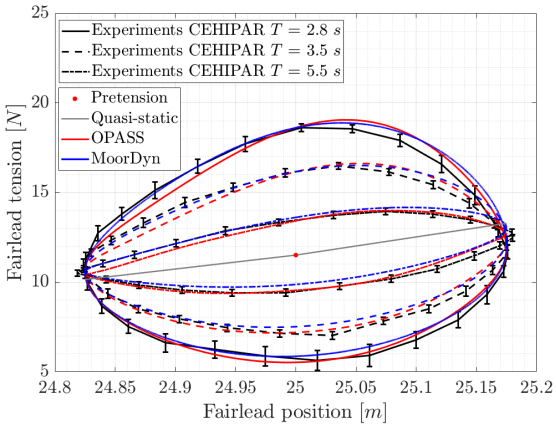

(b) $A = 0.175\ [m]$

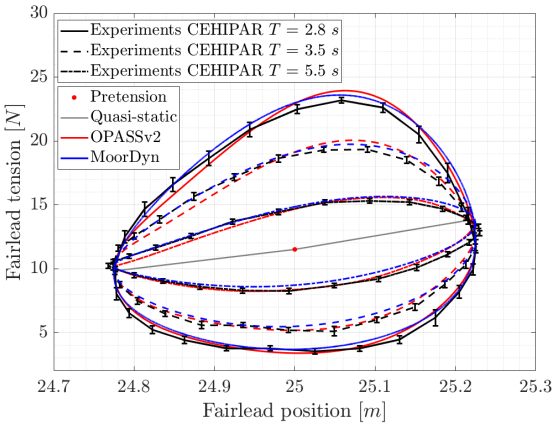

(c) $A = 0.225\ [m]$

Figure 4.20: Comparison between the computed fairlead tension values and the experimental measurements of the isolated mooring line for three different oscillation amplitudes $A = 0.125,\ 0.175,\ 0.225\ [m]$ and three different periods $T = 2.8,\ 3.5,\ 5.5\ [s]$ for the isolated mooring line.

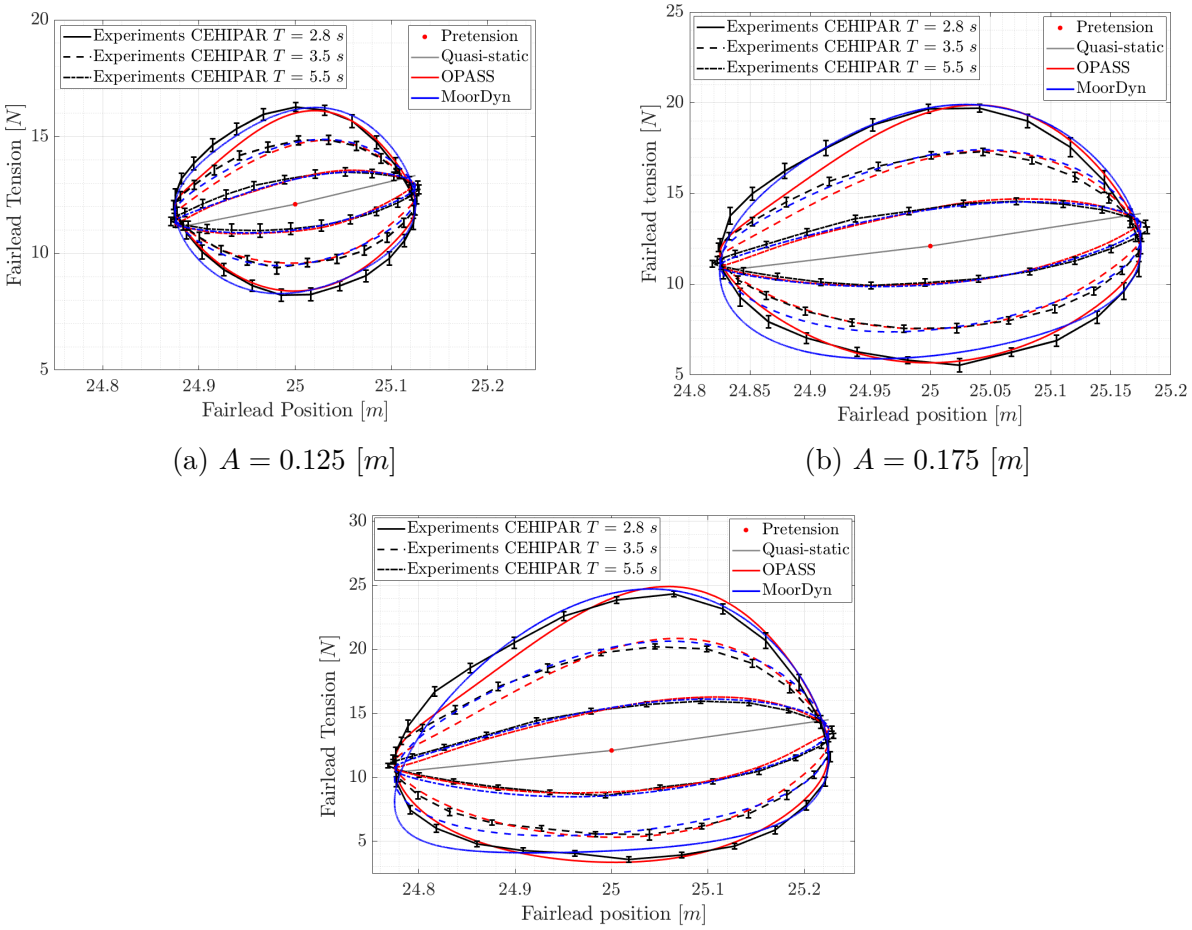

(a) $A = 0.125\ [m]$

(b) $A = 0.175\ [m]$

(c) $A = 0.225\ [m]$

Figure 4.21: Comparison between the computed fairlead tension values and the experimental measurements of the isolated mooring line with the clump weight in Config. 1 for three different oscillation amplitudes $A = 0.125,\ 0.175,\ 0.225\ [m]$ and three different periods $T = 2.8,\ 3.5,\ 5.5\ [s]$ for the isolated mooring line.

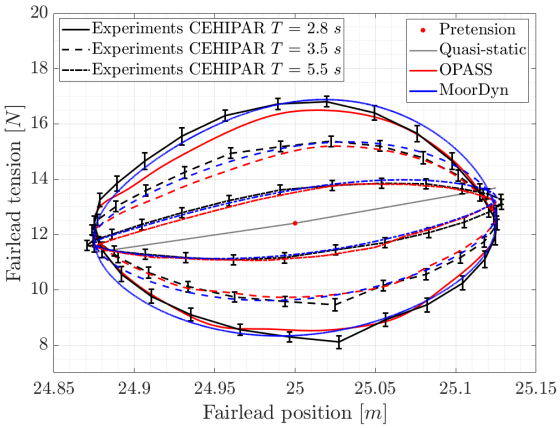

(a) $A = 0.125\ [m]$

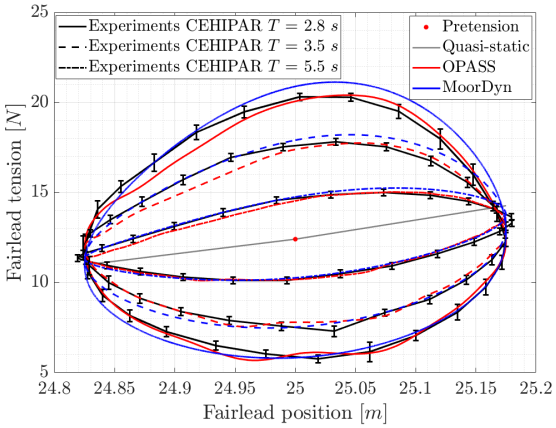

(b) $A = 0.175\ [m]$

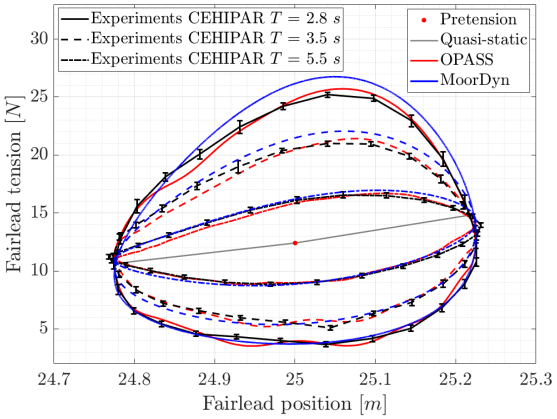

(c) $A = 0.225\ [m]$

Figure 4.22: Comparison between the computed fairlead tension values and the experimental measurements of the isolated mooring line with the clump weight in Config. 2 for three different oscillation amplitudes $A = 0.125,\ 0.175,\ 0.225\ [m]$ and three different periods $T = 2.8,\ 3.5,\ 5.5\ [s]$ for the isolated mooring line.

4.4.2.2 Motions response

In this section, the results of the image processing of the camera recordings are presented. The postprocessing of the visual data was performed with MATLAB tools and consisted of applying a moving method to detect local outliers according to a specified window. A Piecewise Cubic Hermite Interpolating Polynomial (pchip) has been used to replace outliers. Finally, a classical filter for frequencies higher than the third harmonic has been applied, and optical errors have been excluded.

Fig. 4.23 shows the trajectories of markers 2 to 10 for the mooring line without clump weight and with clump weight in the first position (Config. 1). The results show the same pattern described in previous publications of Azcona et al. [2], Barrera et al. [4], where the points near the top of the line move very similarly to the fairlead, while deeper points move more vertically. Despite the slightly changed trajectories of the points, the pattern barely changes with the addition of clump weights in all configurations. Trajectories of the mooring line with clump weight in the second position (Config. 2) have not been added because the similarity in the results overlaps with the other two configurations with a slight change of position because of the different initial catenary shape.

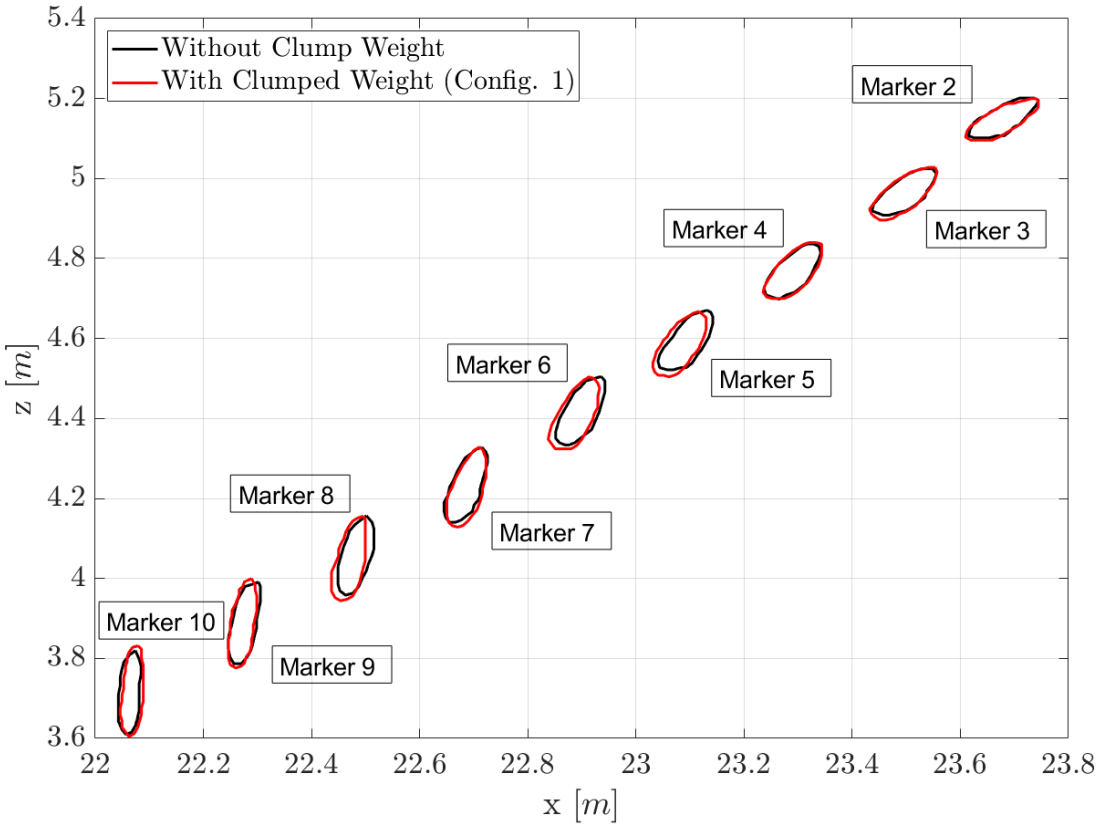

Figure 4.23: Trajectories of the tracked points of the mooring line for a top-end motion of an Amplitude of 0.175 m and periods 3.5 s. Markers 2 to 10 are indicated in the figure.

Fig. 4.24 presents the tracked motions of three mooring line points with and without clump weight in the first position (Config. 1), for an amplitude of 0.125m and three periods of $2.8, 3.5, 5.5$s. For all points, the ranges of motion in the x- and z-axis of the reference system in Fig. 4.9 are practically the same, with some minor changes observed for the shortest periods, and a slight change in the initial position of the marker due to the different catenary shapes caused by the presence of the clump weight. Then it can be concluded that the kinematics of the mooring line remain practically unchanged with the addition of the device. This can possibly be explained because the amplitudes of the fairlead tensions are very similar when the clump weight is added to the line in Config. 1 (refer to Fig. 4.16).

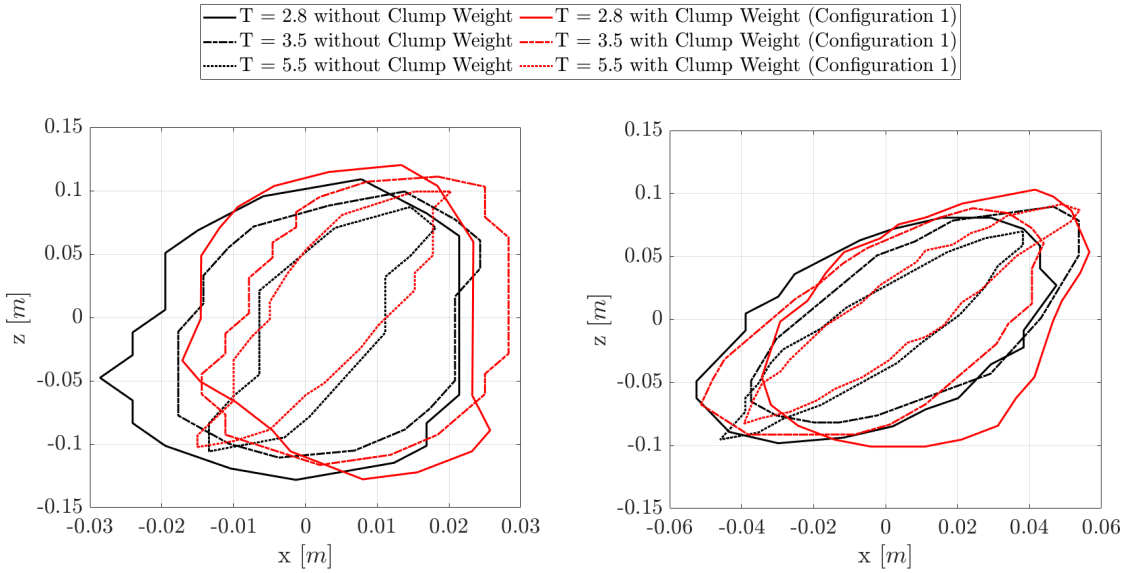

(a) Trajectories of the mooring line lower point of Fig. 4.23 (Marker 9).

(b) Trajectories of the mooring line middle point of Fig. 4.23 (Marker 5).

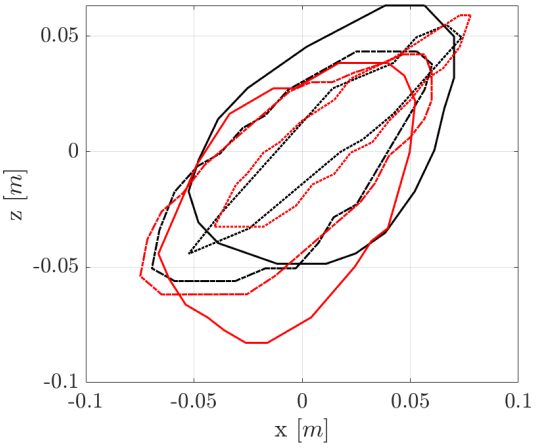

(c) Trajectories of the mooring line upper point of Fig. 4.23 (Marker 2).

Figure 4.24: Tracked motions of three points of the mooring line, for a top-end motion of an Amplitude of 0.125 m and periods $2.8, 3.5, 5.5$ s.

4.4.2.2.1 Numerical validation The trajectory of part of the mooring line in the absence of clump weights has been computed numerically with OPASS and MoorDyn for three oscillation periods $T = 2.8,\ 3.5,\ 5.5\ s$ and one amplitude $A = 0.125\ m$, see Fig. 4.25. It can be observed that the prediction of the numerical tools approximates very well the values measured in the experiments for all periods and amplitudes tested. When the clump weight is modeled in the numerical codes, the dynamic effects of the mooring line are still well predicted; see, for example, Fig. 4.26 for Config. 1.

The optical errors have not been corrected in the postprocessing and their effects are present for the nodes placed at the ends: markers 1 to 3 and 8 to 11. This could be the explanation for why the numerically obtained trajectories agree better with the experimental results for central nodes (Markers 4 to 7). This could be improved using several cameras instead of a single one with better calibration process at the beginning of the tests [28]. This has been left for a future work.

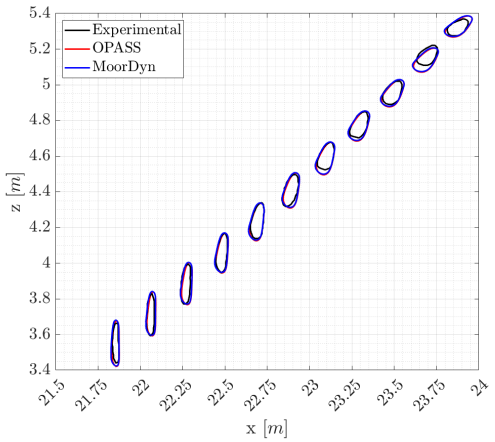

(a) $T = 2.8$ s

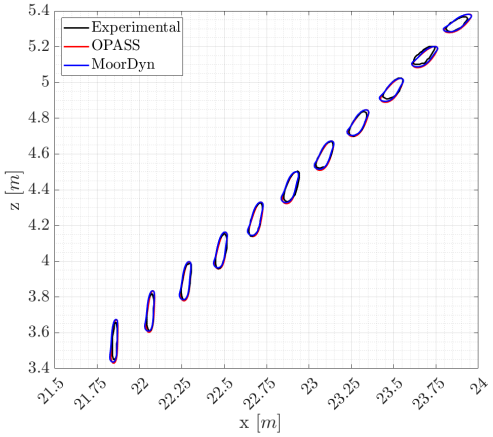

(b) $T = 3.5$ s

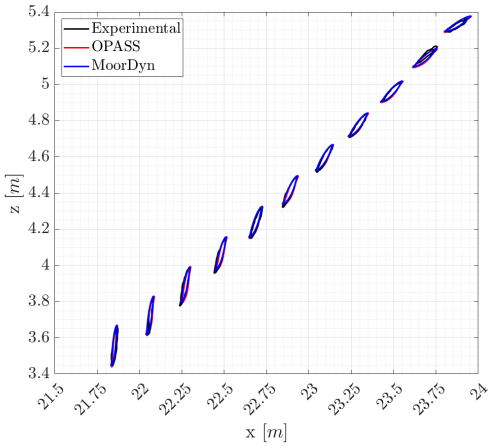

(c) $T = 5.5$ s.

Figure 4.25: Comparison between computed trajectories of catenary nodes and experimental tracked points for different oscillation periods $T = 2.8,\ 3.5,\ 5.5$ s and amplitude $A = 0.125$ m for the isolated mooring line without clump weight.

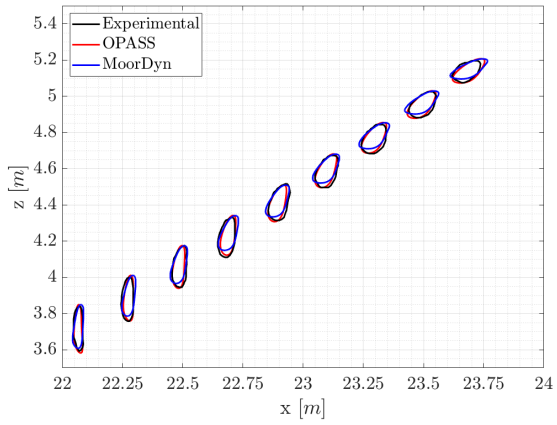

(a) $T = 2.8$ s

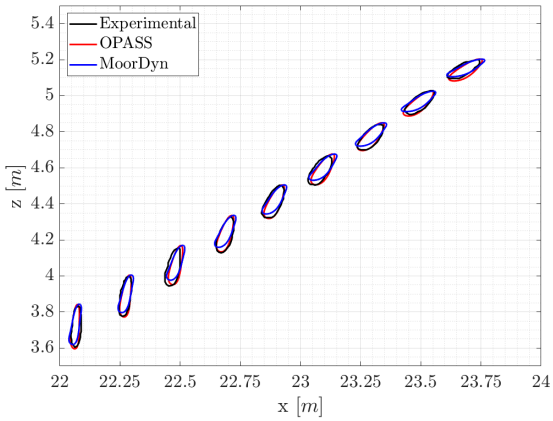

(b) $T = 3.5$ s

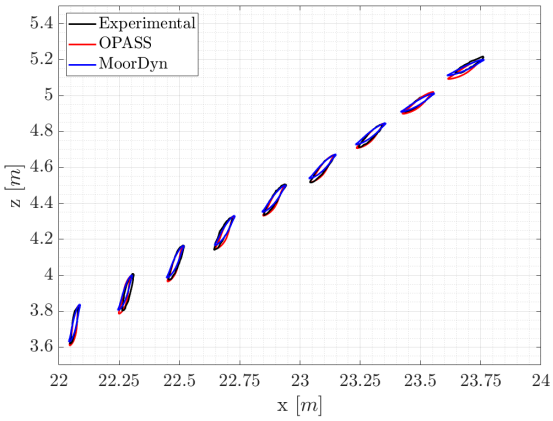

(c) $T = 5.5$ s

Figure 4.26: Comparison between computed trajectories of catenary nodes and experimental tracked points for different oscillation periods $T = 2.8,\ 3.5,\ 5.5$ s and amplitude $A = 0.125$ m for the isolated mooring line with clump weight (Configuration 1).

4.5 Concluding remarks

In this chapter, the influence of the clump weights when added to an isolated mooring line is studied from a dual point of view: experimentally, using surge forced oscillations scaled experiments in a towing tank, and numerically, using a finite element numerical tool where the action of the clump weights has been modeled. Then, the results are verified with an established simulation code that includes the feature of inclusion of extra elements into the line.

In static cases, the geometric stiffness of the mooring line in the horizontal plane increases when a clump weight is added and the pretension is not controlled. Therefore, a mean reduction in the surge motion of the moored platform should be expected in practical applications at the expense of a tension increase. In contrast, when a clump weight is added and the pretension is maintained, the geometric stiffness of the mooring line is decreased, expecting lower tensions but larger motions.

The installation position of the clump weight has been shown to have a great influence on the pretension and geometric stiffness of the line. The location farther from the fairlead showed larger pretension values and therefore a stiffer system. Then, as expected, the experimental results show an increase in the fairlead tension when the clump weights are present and the pretension is not controlled, approximately increasing its value in relative terms between 6% and 9% of the dynamic maximum fairlead tension with respect to the isolated mooring line for the two tested positions, respectively. In terms of energy dissipation of the mooring line, a clump weight farther from the fairlead dissipates more energy; therefore, setting the clump weight farther from the fairlead with the obvious limitation of seabed contact seems to be an adequate practice to reduce the surge motion of the moored platform.

The simulation tool OPASS [2], specifically designed for mooring line dynamics, now includes the possibility of clump weight implementation. The tool has been successfully validated against experiments with remarkable accuracy and verified with the well-known MoorDyn code [49], an open-source numerical tool for mooring line dynamics developed by NREL. The performance of the numerical tools is notably accurate when its predictions are compared to the experiments for both an isolated line with and without the presence of clump weights in all the configurations, in terms of fairlead tension and line kinematics. However, when the fairlead accelerations grow, and the mooring line excitation is more violent, the numerical approach tends to overpredict the maximum tension in the fairlead. This could be due to the difficulty of accurately determining the line drag and added mass coefficients.